Analysis, Design, and Fabrication of Archimedean Spiral Antennas

by

Paul C. Werntz

Thesis submitted to the Faculty of the

Virginia Polytechnic Institute and State University

in partial fulfillment of the requirements for the degree of

Master of Science

in

Electrical Engineering

APPROVED:

W. L. Stutzman, Chairman

G. S. Brown

W. A. Davis

August 1988

Blacksburg, Virginia

Analysis, Design, and Fabrication of Archimedean Spiral Antennas

by

Paul C. Werntz

W. L. Stutzman, Chairman

Electrical Engineering

(ABSTRACT)

The uses for wideband antennas include wideband measurement systems, spread spectrum communications systems, feeds for reflectors and elements in wideband arrays. Here, wideband antennas are discussed and Archimedean spiral antennas are found to be appropriate elements for use in a new type of wideband array referred to as the wideband switched array. The design of an Archimedean spiral and a necessary wideband balun transformer feed structure are presented. To aid in the design, the Electromagnetic Surface Patch Code (ESP) developed by Ohio State University is used. The spiral and feed structure are constructed and measured results are compared to predictions obtained by ESP.

Acknowledgements

Foremost, would like to express my appreciation to my advisor, Dr. W.L. Stutzman, for all his patience, helpful suggestions, and fine editing job, without which this work would be impossible to read. I would also like to thank the members of my committee, Dr. G.S. Brown and Dr. W.A. Davis, for their many suggestions and donated time.

I would like to thank the members of the band, , , and , without whom our fame would have been impossible. Also I would like to thank the members of the late night Satcom club, and , for the company we spent together during the long hours. Particularly thanks to whose computer programs are responsible for many of the figures in this work.

I would like to thank the Satcom Group employees and graduate students for their consultation and companionship.

Finally I would like to thank and my Parents for all of their encouragement and understanding.

Table of Contents

I. Introduction

There are many uses for an antenna whose characteristics remain virtually unchanged over exceptionally large bandwidths. These uses include wideband measurement systems, spread spectrum communication systems such as those using "frequency hopping", feeds for reflectors, and radar. Considerable time may be saved when performing wideband antenna or scattering measurements by using one wideband antenna in the measurement system rather than switching between narrowband antennas. Likewise, frequency hopping communication systems can be made more efficient by using only one radiating element. A narrowband feed-reflector system may be converted to a wideband system by replacing the narrowband feed by a wideband one because reflectors are inherently wideband. Perhaps the greatest use for wideband antennas is radar. They are of particular importance in radar detection where there is no apriori knowledge of the radar's frequency.

The class of frequency independent antennas is made up of antennas for which pattern, impedance and polarization remain virtually unchanged over exceptionally large bandwidths. Frequency independent antennas are distinguished by the trait that their electrical dimensions scale with frequency. Ideally the electrical dimensions of such

antennas remain constant over the entire electromagnetic spectrum. This requires infinite physical dimensions, so in practice the frequency independent structure is truncated giving the antenna an upper and lower frequency limit.

In many cases a wideband array offers significant advantages over individual wideband antennas. Advantages include increased gain, greater control over the radiation pattern including the ability to electronically steer the beam, and the possibility of conformal structures. Also, arrays may prove to be economical because several small antennas can be used to replace one large and possibly expensive antenna. Because of fixed element spacings, conventional quasi-planar arrays do not scale with frequency and are inherently narrowband. As frequency is increased the effective electrical spacing between each element will increase causing grating lobes to appear in the visible region of the radiation pattern. The problem of designing a wideband array is further complicated by the fact that the low frequency limit of a wideband antenna is determined by its outer dimensions. Hence, these antennas are electrically large at their upper frequency of operation and will not fit close together. Nevertheless, with certain array architectures wideband arrays are possible [1].

There is an architecture which resolves the basic wideband array conflict between avoiding electrically large interelement spacings while needing electrically large elements. The concept first abandons the requirement of identical elements in a uniform spatial grid. Then, nonidentical elements are used in a grid arrangement that is changed electrically as the frequency is changed. This is referred to as a wideband switched array. Shively [1] has examined several geometries and found an architecture which provides for operation over two octaves; it is an eight element planar array using elements of two different sizes.

Here, wideband antennas are discussed and Archimedean spiral antennas are found to be appropriate elements for use in Shively's eight element wideband switched array.

The design of an Archimedean spiral element and necessary feed structure are presented. To aid in the design, a computer code developed at Ohio State University [17] is used to predict the spiral's performance. The code is called the Electromagnetic Surface Patch Code (ESP) and makes use of the method of moments. The spiral and feed structure are constructed and the measured results are compared to the predictions made by ESP. In general, it is found that ESP is a reliable method of obtaining pattern information. ESP is also found to be a reliable method of obtaining impedance information as long as frequencies are chosen low enough so that the thin wire approximations made by ESP, that the radii of all wires in the structure remain less than then 0.1λ, are not violated.

II. Basics of Spiral Antennas

As will be shown in the following chapter, spiral antennas are appropriate elements for use in Shively's planar wideband switched array [1]. Spiral antennas, which exhibit exceptionally large bandwidths, are members of the class of antennas known as frequency independent antennas. There are two underlying principles behind the frequency independent behavior of spiral antennas: minimization of the dependence on fixed physical lengths and the nature of the self-complementary structure. We will discuss these.

If a lossless antenna has electrical dimensions which are independent of frequency, it will have characteristics which are independent of frequency. Put another way, the performance of a lossless antenna is independent of frequency if its dimensions, measured in wavelengths, are held constant. It follows that if the shape of the antenna could be specified entirely by angles and the structure could be made infinite, its performance would be frequency independent. Hence "frequency independent antennas are designed to minimize finite lengths and maximize angular dependence" [2].

If Z_m is the input impedance of a planar antenna, and Z_a is the input impedance of a complementary structure in which the metal is replaced by air and the air is replaced by metal, then by Babinet's principle Z_m and Z_a are related as follows:

$$(Z_a)(Z_m) = \frac{\eta_o^2}{4} \tag{2.0-1}$$

where η_o is the intrinsic impedance of free space. If the geometry of the antenna is identical to that of its complement, then the antenna is self-complementary and [2]

$$Z_a = Z_m = \frac{\eta_o}{2} = 188.5\,\Omega\,. \tag{2.0-2}$$

The above result is independent of frequency. Therefore, a self-complementary structure is another design objective for frequency independent antennas [2].

Spiral antennas are structures which minimize finite length, maximize angular dependence, and tend to be self-complementary. These properties combine to give spiral antennas their wideband characteristics.

Many of the radiating characteristics of spiral antennas can be explained by a "band" description of radiation [9]. Referring to Fig. 2.0-1, assume the spiral is fed at the center with the two arms 180 degrees out of phase. Points P and Q are on different arms and are an equal number of turns away from the center of the spiral, O. Therefore, there is a 180 degree phase difference between the currents at points P and Q. If the arc length QP' is equal to one half of a wavelength, the currents at points P and P' will be inphase. If the spiral is tightly wound, the arclength QP' is approximated by $\pi d/2$, where d is the diameter QP', and the currents on adjacent arms of the spiral will be approximately inphase for an annular band about the diameter d causing on-axis radiation to occur. The spiral antenna can thus be considered a two wire transmission

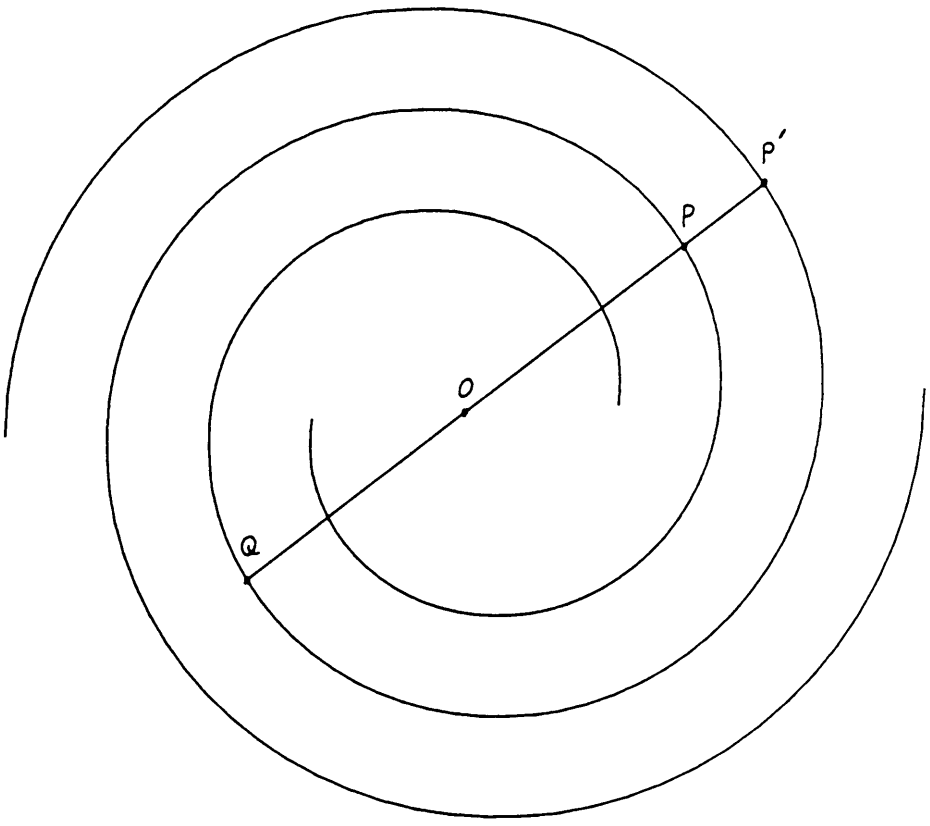

Figure 2.0-1. Two arm spiral antenna.

line which gradually transforms itself into a radiating structure. The annular band is referred to as an active region. In this case, the active region has a circumference of one wavelength and the radiation pattern produced by the spiral is similar to that produced by a one wavelength loop of traveling wave current (see Appendix E).

The formation of an active region determines the low frequency limit of the antenna. If D is the outer diameter of the spiral, the lowest operating wavelength is approximated by [9]

$$\lambda_L = \pi D. \tag{2.0-3}$$

In the active region equal amplitude orthogonally directed current components exist at points spaced 90 degrees apart along the arms of the spiral, these points are also a quarter wavelength apart causing them to be 90 degrees apart electrically. The result is that radiation from the spiral is circularly polarized with the sense of the polarization being identical to the sense of the outward directed spiral winding.

If the attenuation through the first active region is not large, as is the case for loosely wound spirals [3], the current waves travel with little attenuation past the first active region to form a second active region. Arguments similar to the ones used in the preceding discussion may be used to show that the circumference of the second active region is 3λ. The radiation pattern produced can be approximated by superposition of the patterns produced by traveling wave current loops of circumferences one and three wavelengths.

The previous results may be extended to spirals which contain more then two arms. For any N arm spiral with rotational symmetry such that a rotation of $\frac{2\pi}{N}$ radians about the axis leaves the structure unchanged, any arbitrary excitation may be decomposed into $N-1$ independent normal modes [3]. For any M^{th} normal mode, $(M \leq N-1)$, the arms are excited with equal amplitudes and with phases varying as

$$\frac{-2\pi nM}{N} \text{ radians} \tag{2.0-4}$$

where n is the number of the arm. A property of any M^{th} normal mode excitation is that the first active region, as described previously for the two armed spiral, has circumference $M\lambda$, and the pattern produced by the spiral is similar to that produced by a loop of traveling wave current with circumference $M\lambda$.

As with the two armed spiral, current may travel past the first active region to form a second active region. For an N arm spiral excited in normal mode M the second active region will have circumference $(M + N)\lambda$.

Radiation patterns for the first five modes of an idealized equiangular spiral (see Section 2.1 for a discussion of equiangular spirals) which contains an infinite number of arms and has infinite size have been derived analytically [4] and are shown in Fig. 2.0-2. Radiation patterns produced by all modes of excitation, with the exception of the $M = 1$ mode, possess a null on boresight, where boresight is defined as being along the axis of the spiral perpendicular to the plane of the spiral. The phases of the radiation patterns vary with the azimuthal angle ϕ approximatly as $e^{-jM\phi}$ [3].

A multi-arm spiral excited independently in both the $M = 1$ and $M = 2$ modes can be used for direction finding [30]. In principle, the two independent ports provide two independent solutions to the two position unknowns of the target. The position unknowns are the angle off of the antenna's boresight, θ , and the azimuthal angle from some arbitrary reference point on the antenna, ϕ. With reference to Fig 2.0-2, it is evident that the power ratio of the fields radiated by the $M = 1$ and $M = 2$ modes is unambiguous and yields the θ unknown [30]. As one rotates the spiral by 360°, the phase of the radiated fields progress from 0 to 360° for the $M = 1$ mode and from 0 to

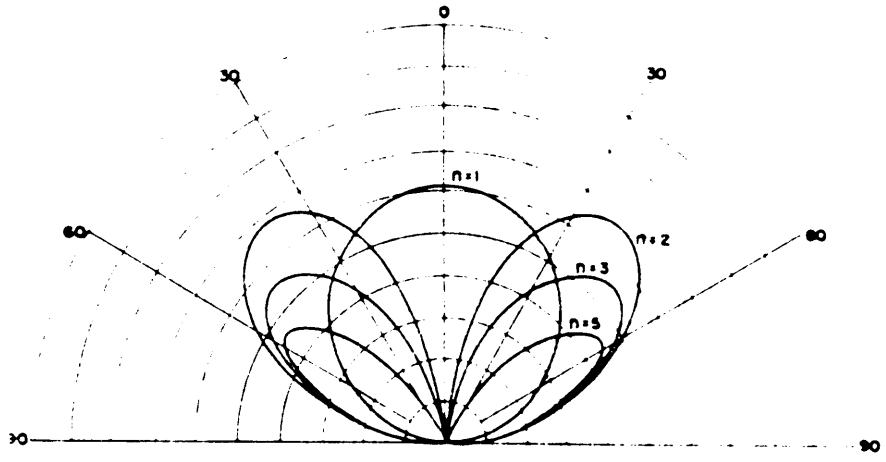

Figure 2.0-2. Radiation patterns for the first five modes of an infinite equiangular Archimedean spiral antenna with infinite number of arms. The spiral is located in the xy-plane which is perpendicular to the plane of this page.

720° for the $M = 2$ mode; therefore, comparison of the phase of these two signals uniquely determines the ϕ unknown [30].

For the case of the wideband switched array we are interested in elements which produce a pattern maximum on boresight. This restricts us to the $M = 1$ mode. For a two arm spiral ($N = 2$) to be excited in the $M = 1$ mode, we find from (2.0-4) that the two arms must be excited with voltages of equal amplitude and opposite phases. This is the simplest means of exciting the $M = 1$ mode in terms of both spiral structure and excitation. Unless otherwise stated, the rest of this Chapter assumes the case of a two armed spiral with the two arms excited with equal amplitudes and opposite phases.

2.1 The Equiangular Spiral Antenna

The equiangular spiral antenna (or log spiral antenna) is often referred to as a frequency independent structure. This is not true in the strictest sense, even for an infinite structure, because a change in frequency is equivalent to a rotation of the structure specified in wavelengths about its central axis [3]. As this is the only theoretical change observed with frequency for an infinite structure, it is logical to refer to it as frequency independent.

The equiangular spiral antenna is based on the equiangular spiral curve as shown in Fig. 2.1-1. The distance of the curve from the origin is given in cylindrical coordinates by

$$r = r_o e^{a\phi}. \tag{2.1-1}$$

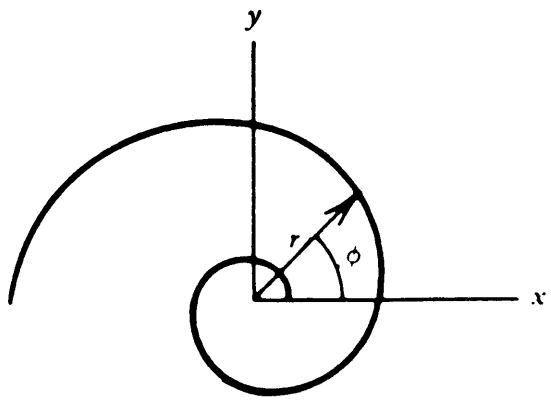

Figure 2.1-1. Equiangular spiral curve.

The minimum distance of the curve from the origin is given by r_o while the rate of growth is determined by a.

A right-handed two arm equiangular spiral antenna is shown in Fig. 2.1-2. The boundaries of each arm are defined by equations of the form given in (2.1-1). One arm of the spiral is defined by the curves

$$r_1 = r_o e^{a\phi} \quad \text{and} \quad r_2 = r_o e^{a(\phi-\delta)}. \tag{2.1-2}$$

For symmetry the other arm is identical to that given by (2.1-2), but is rotated through 180 degrees. It is defined by the curves

$$r_3 = r_o e^{a(\phi-\pi)} \quad \text{and} \quad r_4 = r_o e^{a(\phi-\pi-\delta)}. \tag{2.1-3}$$

The widths of the arms are governed by the angle δ. When $\delta = \pi/4$ the antenna is self-complementary. This is not necessary, but provides for the best pattern symmetry [2]. As noted earlier, a change in frequency is equivalent to a rotation of the spiral about its centeral axis and hence a rotation of the radiated field. Because rotation becomes more evident as the pattern losses symmetry, the self-complementary structure provides for the most frequency independent operation. A left handed spiral can be generated by simply using negative values for a.

The amount by which the radius of the antenna increases per turn is given by

$$\varepsilon = \frac{r_o e^{a(\phi+2\pi)}}{r_o e^{a\phi}} = e^{a2\pi}. \tag{2.1-4}$$

A typical value of ε is 4 corresponding to $a = 0.221$. With $\varepsilon = 4$, only one and one half turns are required for an 8:1 bandwidth [2].

If (2.1-2) ,(2.1-3) and $\delta = \pi/4$ were the only equations defining the spiral of Fig. 2.1-1, it would be infinite, and exhibit frequency independent behavior. The inner radius

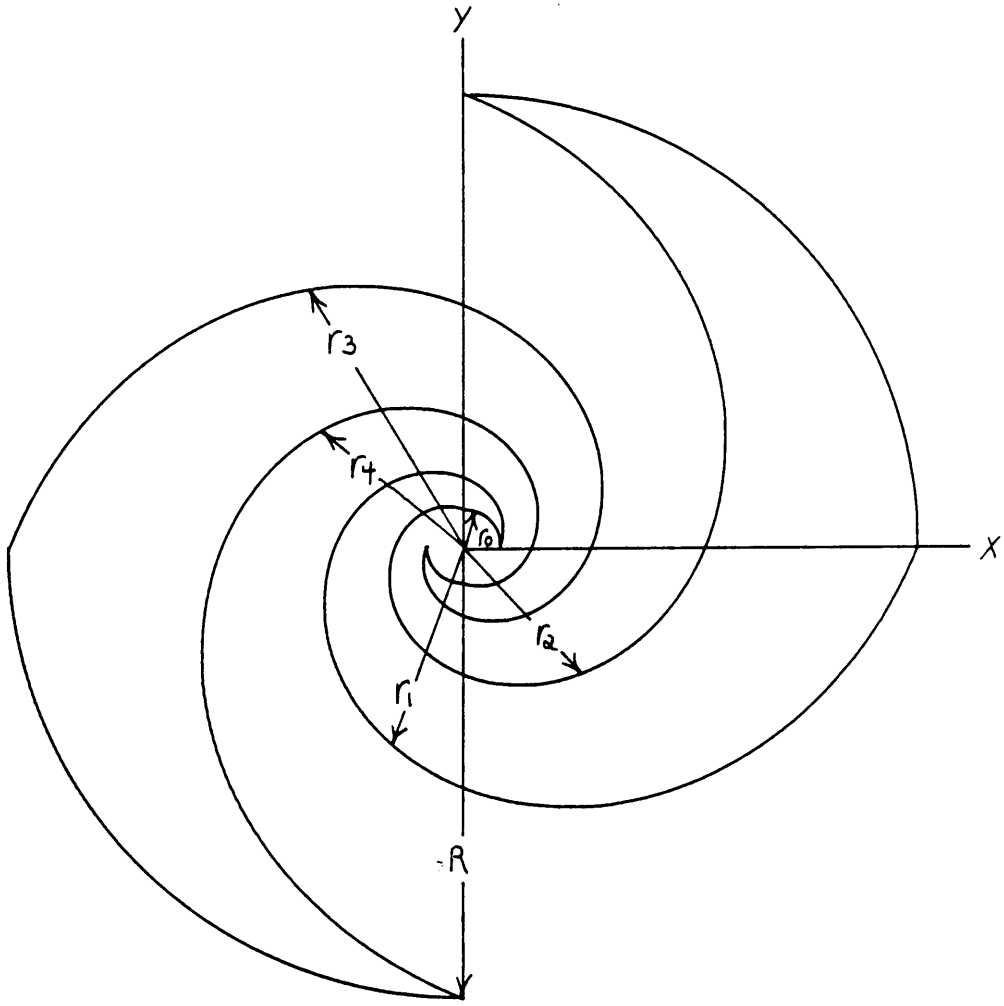

Figure 2.1-2. Right-handed two arm equiangular spiral.

r_o and the outer radius R define the boundaries of the finite structure, and likewise determine the upper and lower frequency bounds of operation. For $\varepsilon = 4$, the low frequency limit is given by $R \simeq \frac{\lambda_L}{4}$ and the upper frequency limit is given by $r_o \simeq \frac{\lambda_U}{4}$ [2] where λ_U and λ_L are the wavelengths of the upper and lower frequency bounds respectivly.

From Babinet's, principle the theoretical impedance of the self-complementary equiangular spiral is 188.5 + j0 ohms. In practice the measured values tend to be lower. An input impedance of about 164 ohms has been measured over a 6:1 frequency range from 500 MHz to 3 GHz [6].

The radiation pattern of the self-complementary equiangular spiral is bidirectional with a wide beam normal to each side of the plane of the antenna. The polarization is close to circular with the sense of the polarization (right or left handed) being the same as that of the spiral. The pattern beamwidth is around 80 degrees and is rotationally symmetric about boresight for values of a less than 0.2. For larger values of a the pattern shows asymmetry and the rotation with frequency is observed [3].

2.2 *The Archimedean Spiral Antenna*

A two arm Archimedean spiral is shown in Fig. 2.2-1. The spiral is based on a curve whose distance from the origin is given in cylindrical coordinates by

$$r = r_o \phi \, . \tag{2.2-1}$$

The edges of one arm are defined by

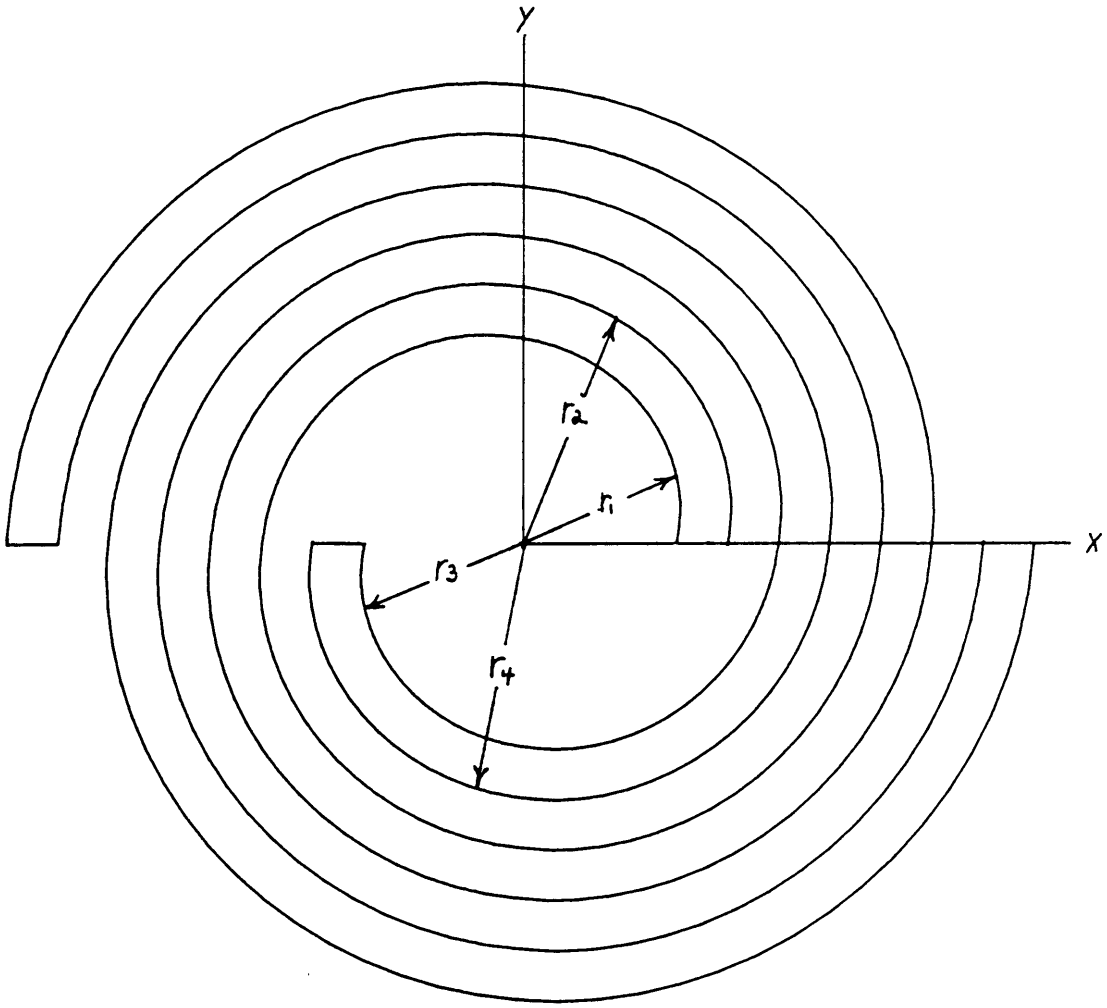

Figure 2.2-1. Printed circuit two arm Archimedean spiral.

$$r_1 = r_o\phi + b_1 \quad \text{and} \quad r_2 = r_o\phi + b_2 \,. \tag{2.2-2}$$

The second arm is rotated through 180 degrees for symmetry and its edges are defined by

$$r_3 = r_o(\phi - \pi) + b_1 \quad \text{and} \quad r_4 = r_o(\phi - \pi) + b_2 \,. \tag{2.2-3}$$

The width of the arms are given by $b_2 - b_1$. It has been stated that of all the spiral antenna parameters, the conductor width and conductor spacing appear to be the least critical [16]. When the width of the arms are the same as the spacing between arms, the structure is self-complementary; this is the usual case. For the self-complementary structure the input impedance is in the range of 188.5 ohms as predicted by Babinet's principle. This often causes an impedance matching problem as the spiral is usually fed from a 50 ohm coaxial line. The impedance matching problem might be greatly simplified if the impedance of the spiral were reduced by making the ratio of conductor width to conductor spacing greater then unity [16].

The radiation pattern of a tightly wound spiral is similar to that of an equiangular spiral; one lobe perpendicular to the plane of each face and a pattern maximum on axis. The radiation from the spiral is elliptically polarized. As circular polarization is the ideal, a measure of how well the spiral is operating is the axial ratio. Axial ratio is defined as follows: for an elliptically polarized wave the vector representing the electric field rotates with time in the plane perpendicular to the direction of propagation. In this plane the tip of the vector traces out the shape of an ellipse. The ratio of the major to minor axis of this ellipse is the axial ratio. It follows that for circular polarization the axial ratio is one, and as ellipticity is increased the axial ratio increases. For linear polarization (the extreme of an ellipse) the axial ratio is infinite. It has been experimentally verified that the axial ratio is reduced as the spiral is more tightly wound

[16]. This improvement may be explained by band theory. Poor axial ratio results from second pass radiation caused by the current reflected at the ends of each arm. This second pass radiation is polarized in the reverse sense to the primary radiation. The situation exists in which the spiral is simultaneously radiating fields which are circularly polarized in both the clockwise and counter-clockwise sense. The net effect is an elliptically polarized field. As the spiral is more tightly wound and the number of turns is increased, there is an increase in the percentage of input power which is radiated by the first active band. Less power is then reflected at the ends of the spiral arms, and second pass radiation is reduced. It has been shown that the reduction in axial ratio is not accompanied by a corresponding reduction in gain [16]. In general, it is best to obtain the maximum number of turns possible in the allocated space. A comprehensive study of Archimedean spiral antennas has been performed by Nakano [28] who has examined the effects of different architectures, feed locations and number of feeds.

2.3 Unidirectional Antennas

Usually a wideband antenna which exhibits a unidirectional pattern is desired. Two structures which possess this characteristic are conical spiral antennas and cavity backed planar spiral antennas.

A conical spiral antenna is shown in Fig. 2.3-1. The conical spiral results from the projection of a planar spiral onto a cone. It is a conical log-spiral antenna if the planar projection is an equiangular spiral, and it is a conical Archimedean spiral if the planar projection is an Archimedean spiral. To produce a symmetrical radiation pattern a half cone angle of 25 degrees or less is usually required [3].

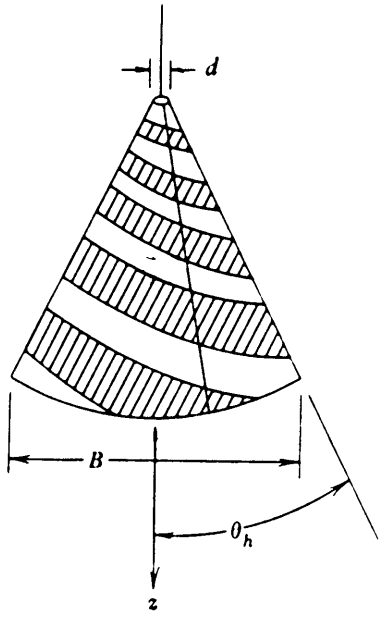

Figure 2.3-1. Conical equiangular spiral antenna.

The arms of the antenna are fed at their termination points at the peak of the cone. As with planar spirals, conical spirals may contain any number of arms N for which $N-1$ orthogonal modes of operation can be defined. A two-arm conical spiral fed in the $M=1$ mode provides a single-lobed circularly polarized pattern along the axis of the cone in the pointing direction. This degrades to elliptical polarization at the beamwidth extremes. Higher order modes produce a null on axis.

With reference to Fig. 2.3-1 the lowest frequency of operation is determined by the base diameter B, the cut off being when $B=3\lambda_L/8$ [8]. The upper frequency of operation is determined by the truncated cone diameter d, the cutoff being when $d=\lambda_u/4$ [8].

A cavity backed planar spiral excited in the $M=1$ mode may also be used to obtain a single main lobe perpendicular to the plane of the spiral. The cavity backed Archimedean spiral is the most common, but the spiral tracing may also be equiangular. The cavity may be a hollow metal-based cylinder or absorber loaded. For the hollow cavity, gain is influenced by cavity depth. It is a maximum for quarter-wave deep cavities, and decreases for greater or smaller depths. This acts to limit the bandwidth to about an octave [3]. Cavity diameter should be approximately equal to the spirals diameter. If the cavity diameter is too large, pattern distortion may result from higher order coaxial and/or waveguide mode excitation of the cavity at frequencies near resonances [16]. For larger bandwidths an absorber loaded cavity is required. The disadvantage of the absorber loaded cavity is a loss of gain. For the case of the hollow quarter-wave deep cavity, the backward directed radiation from the spiral is reflected by the rear wall of the cavity and adds inphase to the forward directed radiation. The forward directed radiation is then approximatly twice what it would be if no cavity were present. For the case of the absorber loaded cavity, the backward radiation is absorbed resulting in an approximate 3 dB loss in gain with respect to the quarter-wave hollow backed spiral.

2.4 Methods of Increasing Bandwidth

It has been shown in in Section 2.2 that the formation of a radiation band, or active region, in which adjacent arms have inphase currents is essential for the operation of the Archimedean spiral. This led to the following relation between the spiral outside diameter, D, and its largest wavelength of operation:

$$D = \lambda_L/\pi \,. \tag{2.4-1}$$

At the lower frequencies the spiral's performance is degraded by the second pass radiation caused by current reflected by the open circuit at the end of each arm. This is not a problem at higher frequencies as the current attenuates rapidly as it travels down the arm and the reflected wave is minimal [4]. If a matched load is attached to the arm ends the reflected current is reduced and spiral's low frequency response is improved, the most dramatic improvement being a decrease in axial ratio [10,16].

The in-phase current condition in the radiation band is the result of a 180 degree phase shift caused by the additional length of the extra half turn. If the electrical length of the arms can be made to appear longer than their physical length, the operating frequency of the spiral of fixed diameter can be lowered. Assuming that the current phase propagation along the wire can be approximated by $e^{-j\beta L_h}$, the phase shift of the extra half turn can be calculated as follows [9]:

$$\phi_h = \beta L_h = \frac{2\pi f L_h}{v} = \frac{2\pi f L_h \sqrt{\varepsilon_r}}{c} = \frac{2\pi L_h \sqrt{\varepsilon_r}}{\lambda} \tag{2.4-2}$$

where

λ = free space wavelength,

L_h = path along the structure for half of a turn,

ε_r = relative dielectric constant of the material on which the spiral is imbedded,

and

v = the phase velocity of light through the material on which the spiral is imbedded.

The shape of a spiral can be chosen to maximize L_h in (2.4-2). For a given maximum antenna width, W, a square shape provides the largest value of L_h, which is $L_h = 2W$. Assuming an air dielectric and $L_h = 2W$, (2.4-2) gives the following solution for $\phi_h = \pi$:

$$W = \frac{\lambda}{4} . \tag{2.4-3}$$

Comparison with (2.4-1) leads to

$$\frac{W}{D} = \frac{\pi}{4} = 0.785 . \tag{2.4-4}$$

Therefore, the size of the spiral is reduced by 21.5 % if the shape is changed from circular to square. A square spiral is shown in Fig. 2.4-1.

The effective value of L_h can be further increased by modulating the metallic arm [10]. The resulting structure is a slow-wave spiral. A square slow-wave spiral resulting from a triangular modulation is shown in Fig. 2.4-2 [9]. The ratio of zig-zag to straight path lengths is 1.79 [9]. The electrical length for the slow-wave spiral is then $L_h = 1.79(2W)$. Setting $\phi_h = \pi$ in (2.4-2) leads to

$$W = 0.14\lambda . \tag{2.4-5}$$

Comparison with (2.4-1) gives

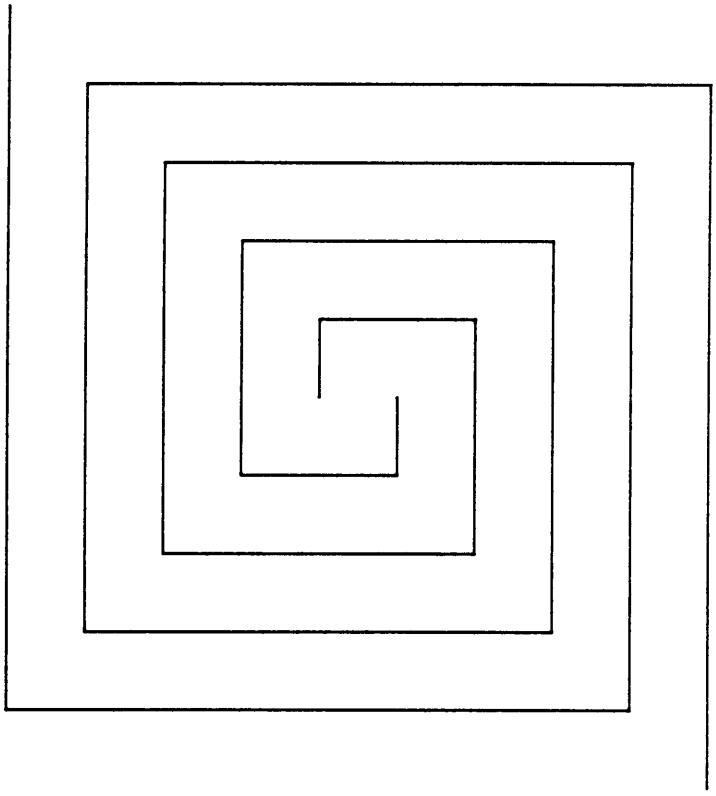

Figure 2.4-1. Square spiral.

$$\frac{W}{D} = 0.14\pi = 0.44\,. \tag{2.4-6}$$

The size of the spiral has been reduced by 56 % compared to the circular spiral.

The reduction in size is not without penalties. Because of the modulations the spiral can not be wound as tight; the result is increased axial ratio and greater frequency dependence [10].

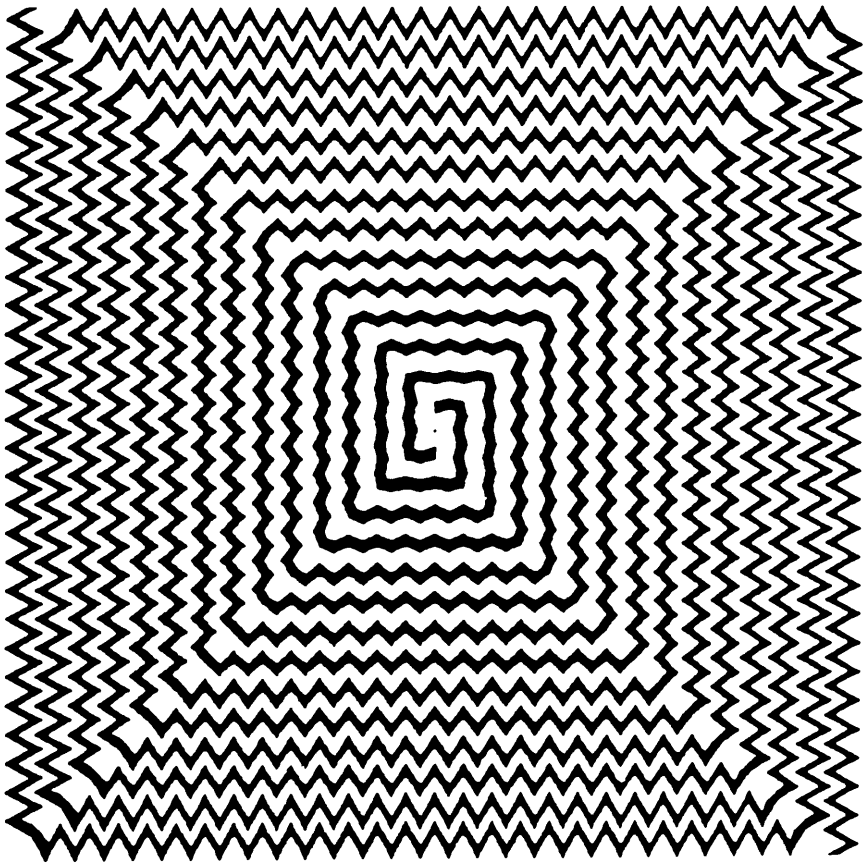

Figure 2.4-2. Square triangular modulated slow wave spiral.

III. The Wideband Switched Array

It is useful to establish a definition of what is meant by the term "wideband array". For our purposes a wideband array is a planar array which is limited in size and at all frequencies of interest has sidelobes less then a specific value. Typically element spacing in an array, as measured between the element centers, is limited to the range of 1/2 to 1 wavelength. Spacings under a half-wavelength lead to poor aperture efficiency (low gain) and increased mutual coupling, while spacings approaching a wavelength lead to the the appearance of grating lobes in the visible region which reduce directivity [2]. Hence, conventional arrays with fixed element number and spacings are constrained to an operational bandwidth of less then an octave.

In order to maintain element spacings in the desired range of 1/2 to 1 wavelength the concept of the switched array has been introduced [1]. Small elements are located in between the large elements of the array. When the frequency is increased such that the spacing between the large elements is one wavelength, the previously inactive small elements are activated reducing the spacings in the array to less than a wavelength, thereby reducing the grating lobes. In this way the switched array accomplishes a form of discrete scaling with frequency.

If the larger elements are 1/2 wavelength apart at the lowest frequency of operation, a frequency bandwidth of two octaves can be achieved with element spacings never exceeding a wavelength. Because interelement spacings in the switched array are allowed to vary vary between 1/2 to 1 wavelength as frequency is changed, the performance of the array can be expected to vary considerably over the two octave bandwidth, but as the sidelobe level is controlled it qualifies as a wideband array under our definition.

3.1 Array Architecture

Various planar switched array architectures have been studied by Shively [1]. The goal was to find a switched array architecture which allows for operation over two octaves while minimizing both the number of elements used and the maximum sidelobe level. To some extent these goals are mutually exclusive and compromises must be made. The result of the study is the wideband eight element planar array structure shown in Fig. 3.1-1. It is convenient to divide the two octave bandwidth into two one octave components. The first octave is defined by the bandwidth between the frequencies f_1 and f_2, where f_1 is the lowest frequency of operation and $f_2 = 2f_1$. The second octave is defined by the bandwidth between f_2 and f_3 so that $f_3 = 2f_2$. With reference to Fig. 3.1-1, in the first octave only the larger elements are active, while in the second octave all of the elements are active. It follows that the larger elements must be capable of operation over a two octave region, while the smaller elements need only be capable of operation over a single octave.

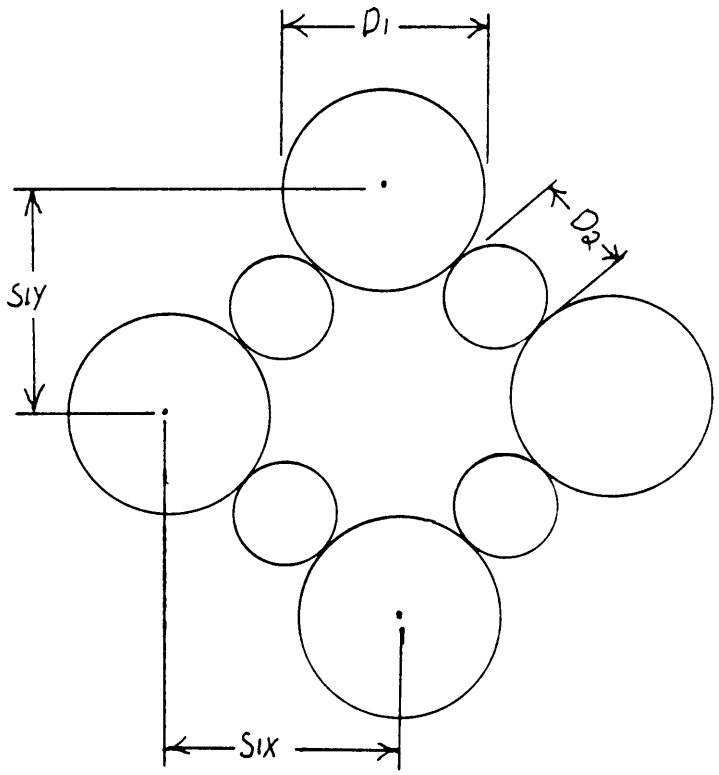

Figure 3.1-1. A planer two octave switched array.

3.2 Element Selection

Due to the wide bandwidth required, spiral antennas appear to be good candidates for use as elements in the wideband switched array. Because of the ease with which they can be constructed, absorber loaded cavity backed Archimedean spiral antennas are particularly attractive. The required bandwidth of one and two octaves, for the smaller and larger elements respectively, is easily within the bandwidth capabilities of the Archimedean spiral. The question is whether or not the Archimedean spiral will accommodate the tight spacing required in the array.

Referring to Fig. 3.1-1, D_1 is the diameter of the larger elements and D_2 is the diameter of the smaller elements. The distance between the center of the larger elements, measured in either the x-direction or the y-direction, is

$$s_{1x} = s_{1y} = s_1 = \frac{\lambda_1}{2}. \tag{3.2-1}$$

where λ_1 is the wavelength of the lowest frequency of operation, f_1. This is related to D_1 and D_2 as follows:

$$s_1 = \frac{\lambda_1}{2} = (D_1 + D_2)\cos\frac{\pi}{4}. \tag{3.2-2}$$

Assuming the elements are Archimedean spiral antennas, the lowest frequency of operation of each element is directly proportional to the elements outside diameter. The larger element's lowest frequency of operation is 1/2 the lowest frequency of operation of the smaller element, this implies $D_1 = 2D_2$. Substitution into (3.2-2) leads to

$$D_1 = 0.472\lambda_1 . \tag{3.2-3}$$

In according with the band theory presented in Section 2.0, the outside diameter of the Archimedean spiral is related to its lowest frequency of operation, f_L, by

$$D_1 = \frac{\lambda_L}{\pi} \cong 0.319\lambda_L \,. \tag{3.2-4}$$

This leads to a 32.4 % margin between the lowest desired frequency of operation and the cutoff frequency. Similar calculations lead to the same margin between the lowest desired frequency of operation for the smaller element, f_2, and the cut off frequency of that element.

In summary, it has been found that the absorber loaded cavity backed Archimedean spiral antenna is an appropriate element for use in the wideband switched array of Fig. 3.1-1. This statement is based on the Archimedean spirals bandwidth capabilities, physical size and ease of construction. What follows is an analysis and development of the Archimedean spiral with a view toward its use in the wideband switched array.

IV. Design and Analysis of an Archimedean Spiral

In Chapter 3 it was established that Archimedean spiral antennas are appropriate elements for use in the wideband switched array of Fig. 3.1-1. In this chapter, we will design the Archimedean spiral to be used in the array and attempt to predict its performance numerically using the Electromagnetic Surface Patch Code (ESP). ESP, which was developed at the Ohio State University Electro-Science Laboratory, is a computer implementation of the method of moments technique for geometries consisting of thin wires and perfectly conducting polygonal plates [17]. The method of moments technique and ESP will be discussed further in Sections 4.2 and 4.3.

The wideband switched array of Fig. 3.1-1 contains two sizes of spiral elements. The smaller spirals may be considered to be truncated versions of the larger elements; therefore, the performance of the smaller spirals is expected to be similar to that of the larger spirals with the exception of a higher low frequency cutoff due to their smaller outside diameter as predicted by (3.2-4). In order to avoid redundancy, we will only be concerned with the design and analysis of the larger spirals in this chapter.

4.1 Design of the Archimedean Spiral

It was decided that the wideband switched array of Fig. 3.1-1 should be designed to operate over the two octave bandwidth between 2.5 GHz and 10 GHz. This frequency range was chosen because it is compatible with both the equipment and dimensions of our antenna range. The Archimedean spiral antenna to be designed corresponds to the larger elements of Fig. 3.1-1 and in accordance with the discussion of Chapter 3 must be capable of operation over the entire two octave region.

The fundamental structure of the spiral discussed in this design is shown in Fig. 4.1-1. It is identical to the spiral of Fig. 2.2-1 with the addition of two circular plates at the center of the structure. The plates are to facilitate attachment of the feed which is to be soldered into place. The equations describing the arms of the spiral are identical to (2.2-2) and (2.2-3). These are repeated here for convenience. The edges of one arm are defined by

$$r_1 = r_o\phi + b_1 \quad \text{and} \quad r_2 = r_o\phi + b_2 \,. \tag{4.1-1}$$

The other arm is identical, but rotated through 180 degrees to provide symmetry; its edges are defined by

$$r_3 = r_o(\phi - \pi) + b_1 \quad \text{and} \quad r_4 = r_o(\phi - \pi) + b_2 \,. \tag{4.1-2}$$

The feed attachment plates may be considered circles of radius R_f centered along the x-axis and positioned such that the circumference is flush with the outer edge of the truncated arm. The spiral is a self-complementary structure. As discussed in Section 2.0, the input impedance can be expected to be in the range of 188.5 ohms. In Chapter 6 it will be shown that this high input impedance is useful in matching the antenna to

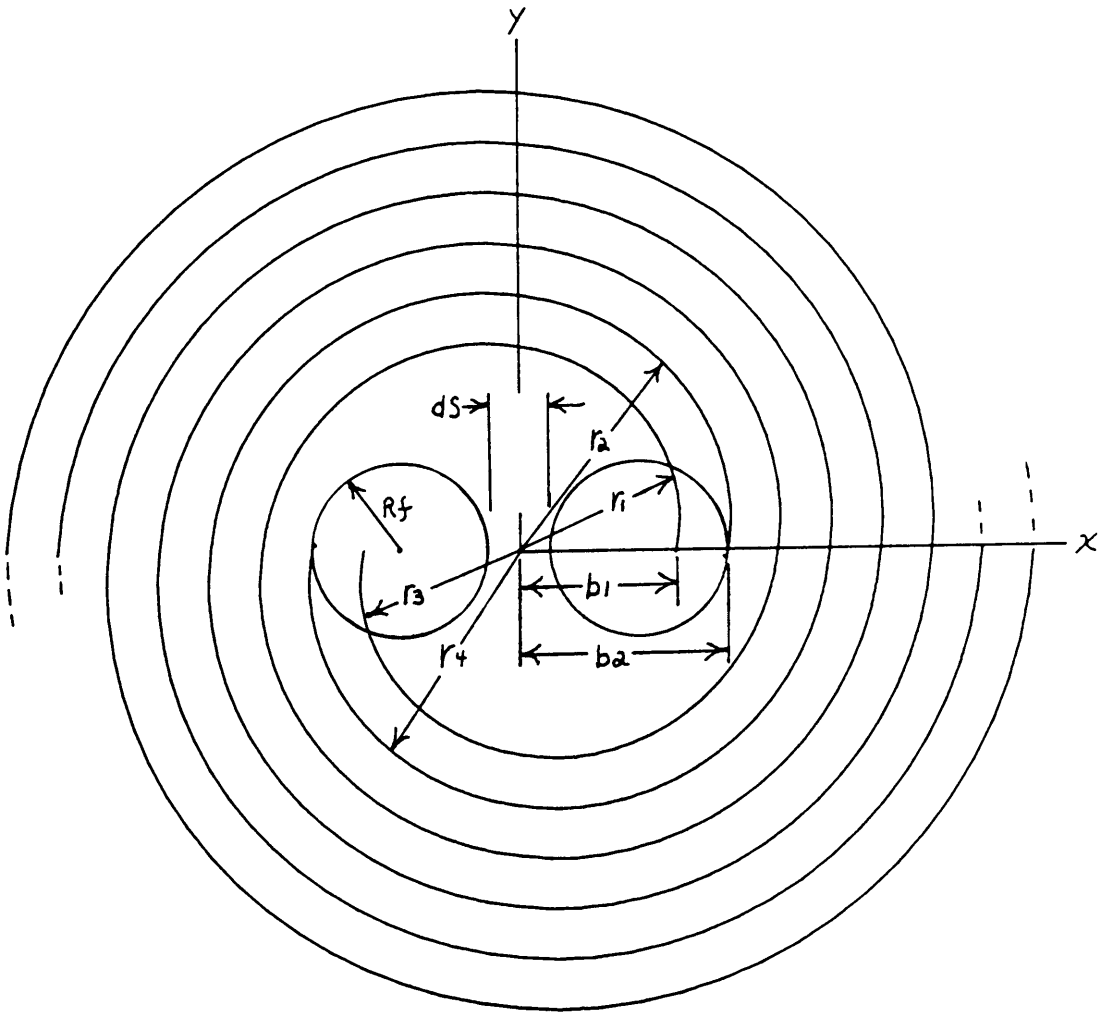

Figure 4.1-1. Structure of the Archimedean spiral antenna.

the feed structure. The width of the conductors, w, and spacing between conductors, s, are chosen such that

$$w = s = 0.03 \; inch \, . \tag{4.1-3}$$

It is noted that this makes for fairly wide conductors and spacings which is in contradiction to the basic tenant of Archimedean spiral design discussed in Chapter 2; that is, to aim for the maximum number of turns possible in the allocated space. We are prevented from significantly increasing the number of turns in the spiral (by reducing s and w) because numerical prediction of spiral performance would be difficult due to the large number of segments or patches required. Another reason for staying away from excessively thin conductors and spacings is spiral construction. As the number of turns are increased, the probability of adjacent arms being accidentally shorted together increases and detection of such a problem becomes more difficult.

The active region at the upper frequency of 10 GHz, as defined in Chapter 2, will have a circumference of 1.181 inches. To insure active region formation, while allowing enough room at the center of the spiral for the feed attachment plates, we chose $b_1 = 0.075$ inch and $b_2 = 0.105$ inch. The radius of the feed attachment plates is then chosen to be $R_f = 0.045$ inch. This leaves a minimum separation of $d_s = 0.03$ inch between feed attachment plates at the center of the spiral. In accordance with the discussion of second pass radiation in Chapter 2, the axial ratio is expected to deteriorate as the frequency approaches the spiral cutoff frequency given by (2.0-3). Therefore, it is advisable to make the the outer diameter of the spiral as large as spacing in the array allows, insuring the lowest possible cutoff frequency. This is defined by (3.2-3) to be $D_1 = 0.472\lambda_1$. For $f_1 = 2.5$ GHz, this leads to $D_1 = 2.23$ inches. The maximum outer diameter of the spiral is found from (4.1-1) and (4.1-2) to be

$$D_1 = 2(r_o\phi_{max} + b_2)\,. \tag{4.1-4}$$

For an Archimedean spiral it can be shown that r_o is related to s and w by

$$r_o = \frac{(s+w)}{\pi}\,. \tag{4.1-5}$$

For our case $s = w = 0.03$ inch; therefore, $r_o = 0.0191$ inch. Substitution of r_o into (4.1-1), along with $b_2 = 0.105$ inch and $D_1 = 2.23$ inches, leads to

$$\phi_{max} = 52.88 \text{ rad}\,. \tag{4.1-6}$$

Division by 2π radians reveals that the number of turns corresponding to $\phi_{max} = 52.88$ radians is $N = 8.416$ turns. This is rounded down to $N = 8$ turns leading to a new outer diameter of $D_1 = 2.13$ inches and a corresponding low frequency cutoff, as given by (3.2-4), of $f_L = 1.76$ GHz. This leaves a 29.6 % margin between the lowest specified frequency of 2.5 GHz and the spirals cutoff frequency f_L.

To conclude, with reference to Fig. 4.1-1, the following values are used in our design of the Archimedean spiral:

$$R_f = 0.045 \ inch \quad b_1 = 0.075 \ inch$$
$$b_2 = 0.105 \ inch \quad r_o = 0.0191 \ inch$$
$$N = 8 \ turns \quad D_1 = 2.13 inches.$$

For the smaller elements of Fig. 3.1-1 all parameters are the same except the number of turns which is reduced to $N = 4$ turns corresponding to an outer diameter of $D_2 = 1.17$ inches. For $D_1 = 2.13$ inches and $D_2 = 1.17$ inches, the minimum spacing between the center of the larger elements is found from (3.2-2) to be $s_1 = 2.33$ inches. Our design objective is to have $s_1 = \lambda_1/2$ where λ_1 is the wavelength at 2.5 GHz, this leads

to $s_1 = 2.36$ inches. Therefore, there is a 1.3 percent margin between the minimum possible spacing of $s_1 = 2.33$ inches and the desired spacing as given by $s_1 = \lambda_1/2$.

4.2 The Method of Moments

The Electromagnetic Surface Patch Code (ESP), which will be used to evaluate the spiral design of the previous section, is a computer implementation of the method of moments technique for geometries consisting of thin wires and perfectly conducting polygonal plates [17]. The method of moments is a general technique used to obtain solutions to equations of the form

$$F(g) = h \tag{4.2-1}$$

where F is a linear operator, h is a known excitation function and g is the unknown response function [18]. In the moment method technique the response function g is expanded as a linear combination of N orthogonal terms

$$g = \sum_{n=1}^{N} C_n g_n \,. \tag{4.2-2}$$

Each g_n is a known function referred to as a "basis" or "expansion" function and each C_n is an unknown constant. The domain of each g_n is the same as g. Substitution of (4.2-2) into (4.2-1) and using the linearity of the F operator leads to

$$\sum_{n=1}^{N} C_n F(g_n) = h. \tag{4.2-3}$$

It is observed that (4.2-3) contains one equation with N unknowns corresponding to the set of coefficients $\{C_n\}$. In order to create N linearly independent equations (4.2-3) may be evaluated at N separate points in the common domain of h and g_n. This is referred to as point matching. Point matching has a disadvantage in that the values computed for the set of coefficients $\{C_n\}$ obtained only satisfy (4.2-3) at the specified points. To improve the solution we may use the method of weighted residuals [2,18]. We define the residual of (4.2-3) to be

$$R = h - \sum_{n=1}^{N} C_n F(g_n)\,. \tag{4.2-4}$$

In the method of weighted residuals the set of coefficients $\{C_n\}$ are found such that the residual is forced to zero in an average sense. Therefore, the inner product of the residual R and a set of "weighting" or "testing" functions, $w_m = w_1, w_2, \ldots, w_N$, is set to zero as follows:

$$\begin{aligned} &< w_m, R > = 0 \\ &m = 1, 2, \ldots, N \end{aligned} \tag{4.2-5}$$

A typical, but not unique, inner product is

$$< w, R > = \int\int_s w \cdot R ds\,. \tag{4.2-6}$$

Applying the results of (4.2-5) to (4.2-4) we have

$$\sum_{n=1}^{N} C_n < w_m, F(g_n) > = < w_m, h > , \qquad m = 1, 2, ..., N. \tag{4.2-7}$$

Assuming that the elements of the set $\{w_m\}$ have been judiciously chosen to be linearly independent, (4.2-7) represents a system of N linearly independent equations. This system may be conveniently written in matrix form as

$$[F_{mn}][C_n] = [h_m] \tag{4.2-8}$$

where

$$F_{mn} = < w_m, F(g_n) >$$

$$h_m = < w_m, h >$$

Equation (4.2-8) can be solved for the unknown set of coefficients $\{c_n\}$ using the matrix inversion

$$[C_n] = [F_{mn}]^{-1}[h_m] . \tag{4.2-9}$$

By finding the set of coefficients $\{C_n\}$ we obtained an approximation to the unknown function g in (4.2-1) which is related to the coefficients through (4.2-2).

4.3 The Reaction Integral Equation

Consider the case of an arbitrarily shaped scatterer in a homogeneous medium illuminated by a time harmonic source $(\overline{J}_i, \overline{M}_i)$. This situation is illustrated in Fig. 4.3-1 where s represents the surface of the scatterer and $\hat{n}$ the unit out-ward normal to the scatterer. The impressed source $(\overline{J}_i, \overline{M}_i)$ radiate the fields $(\overline{E}_i, \overline{H}_i)$ in free space and the fields $(\overline{E}, \overline{H})$ in the presence of the scatterer. The fields interior to the surface s are null. Using Schelkonoff's surface equivalence theorem [19,20], the scatterer may be removed and replaced by the ambient medium without disrupting the existing fields interior and exterior to s, if the following electric and magnetic surface current densities are placed over the surface s :

$$\begin{aligned} \overline{J}_s &= \hat{n} \times \overline{H} \\ \overline{M}_s &= \overline{E} \times \hat{n}. \end{aligned} \tag{4.3-1}$$

This is illustrated in Fig. 4.3-2. The current densities $(\overline{J}_s, \overline{M}_s)$ radiate the scattered fields $(\overline{E}_s, \overline{H}_s)$ which are defined exterior to s by

$$\begin{aligned} \overline{E}_s &= \overline{E} - \overline{E}_i \\ \overline{H}_s &= \overline{H} - \overline{H}_i \end{aligned} \tag{4.3-2}$$

and interior to s by

$$\begin{aligned} \overline{E}_s &= -\overline{E}_i \\ \overline{H}_s &= -\overline{E}_i. \end{aligned} \tag{4.3-3}$$

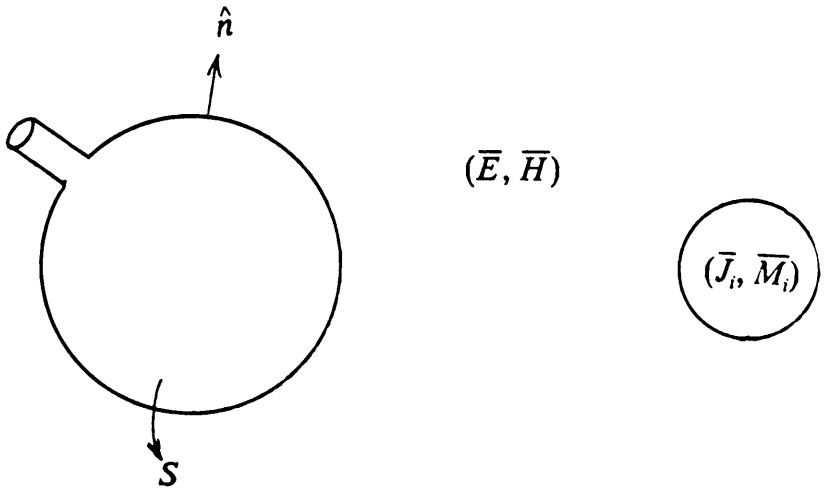

Figure 4.3-1. Scatterer illuminated by a time harmonic source.

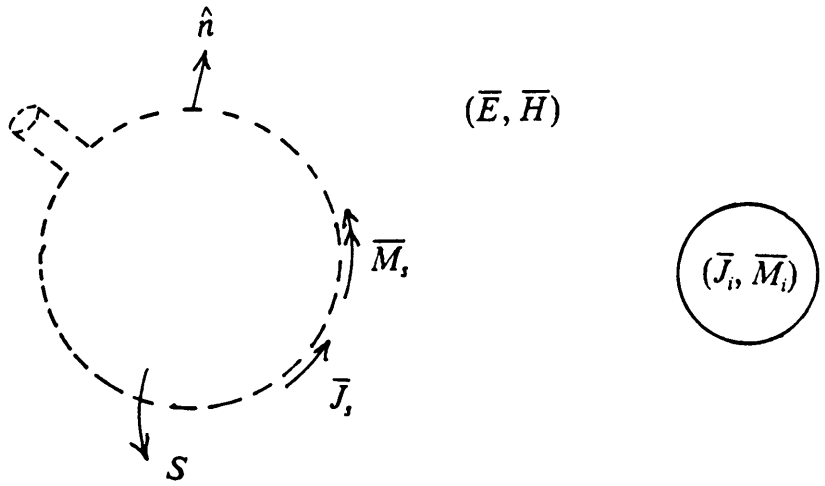

Figure 4.3-2. Magnetic and electric surface currents replace the conductor without disrupting the existing field.

If a test source ($\bar{J}_m$, $\bar{M}_m$) is placed in the volume interior to the surface s its reaction with the fields ($\bar{E}_s$, $\bar{H}_s$) and ($\bar{E}_i$, $\bar{H}_i$) interior to s must be zero as no field exists interior to s. Hence,

$$\int\int\int_{V_m} (\bar{J}_m \cdot \bar{E}_s - \bar{M}_m \cdot \bar{H}_s) dv = \int\int\int_{V_m} (\bar{J}_m \cdot \bar{E}_i - \bar{M}_m \cdot \bar{H}_i) dv = 0 \qquad (4.3\text{-}4)$$

where the integrals are over the volume of the test source. The above is referred to as the Reaction Integral Equation (RIE). If only electric test sources are used ($\bar{M}_m = 0$) the RIE is referred to as the Electric Field Integral Equation (EFIE). If only magnetic test sources are used ($\bar{J}_m = 0$) the RIE is referred to as the Magnetic Field Integral Equation (MFIE). The MFIE may only be applied to closed surfaces while the EFIE may be applied to both open and closed surfaces [19]. The Electromagnetic Surface Patch code (ESP) is based on the EFIE and hence may be applied to both open and closed surfaces. ESP allows for geometries consisting of thin wires and plates. Wires may be finitely conducting and contain lumped loads while plates must be infinitely conducting ($M_s = 0$) [17]. For infinitly conducting plates (4.3-5) reduces to

$$\int\int_s \bar{J}_m \cdot \bar{E}_s \, ds = \int\int\int_{V_i} \bar{J}_m \cdot \bar{E}_i \, dv \; . \qquad (4.3\text{-}5)$$

The plates used in ESP are of zero thickness. The field radiated is equivalent to that radiated by a single current located at the center of the plate [17]. This current is $\bar{J}_s$ and is the vector sum of the top and bottom surface currents of the plate [22]. $\bar{E}_s$ can be related to the current $\bar{J}_s$, then in accordance with the discussion of Section 4.2, $\bar{J}_s$ can be expanded in term of N basis functions $\{F_n\}$ as follows:

$$\bar{J}_s = \sum_{n=1}^{N} I_n \bar{F}_n \ . \tag{4.3-6}$$

An approximate solution to (4.3-5) can now be obtained by arranging it in the form of (4.2-9) where

$$\begin{aligned} F_{mn} &= -\int\int_n \bar{J}_m \cdot \bar{F}_n \, ds \\ C_n &= I_n \\ h_m &= \int\int\int_{V_i} \bar{J}_m \cdot \bar{E}_i \, dv \ . \end{aligned} \tag{4.3-7}$$

A detailed evaluation of (4.3-7) is described in references [21] - [27].

In (4.3-7), $\{\bar{J}_m\}$ is seen to be identical to the weighting function $\{W_m\}$ described in Section 4.2. ESP uses piecewise sinusoidal functions for both weighting and basis functions [17]. This procedure is known as piecewise sinusoidal Galerkin's method and is computationally more efficient then other pairs of expansion and weighting functions [2]. ESP allows either a delta-gap voltage generator or plane wave excitations [17]. Thus, both radiation and scattering problems can be solved. The delta gap generator may be placed at any point between wire segments or at attachment modes between plates and wires. The attachment modes, which insure the continuity of current at the wire to plate junctions, consist of a wire monopole centered on a circular disk monopole which is specified on the plate to which the wire is to be attached [17]. The circular disk monopole must have a radius between 0.1λ and 0.25λ and must be at least 0.1λ away

from all edges of the plate [17]. For all wires, ESP uses a thin wire approximation [17]. For accurate results, wire radii must not exceed 0.01λ [17].

ESP has the capability of computing quantities of interest such as current distribution, input impedance, radiation efficiency, mutual coupling, far zone radiation patterns and radar cross section [17]. However, our interest will be restricted to calculation of input impedance and far zone radiation pattern.

4.4 Numerical Evaluation of the Archimedean Spiral

In this section the Electromagnetic Surface Patch Code (ESP) is used to numerically evaluate the performance of the Archimedean spiral design of Section 4.1. The evaluation is performed with respect to radiated field pattern and input impedance over the two octave region between 2.5 GHz and 10 GHz. Initially our goal was to use ESP to model the spiral with perfectly conducting plates. However, ESP requires structures to be excited by delta-gap generators which may only be placed between wire segments or at attachment points between plates and wires. In either case, wire to plate attachment modes must be specified. These modes, as discussed in Section 4.3, consist of wire monopoles centered on circular disk monopoles. For accurate impedance and pattern data the circular disk monopoles must have radii between 0.1λ and 0.25λ and must be at least 0.1λ away from all edges of the plate on which it is specified [17]. The feed attachment plates have a radius of $R_f = 0.045$ inch corresponding to only 0.021λ at the highest frequency of 10 GHz where the plates appear the largest electrically. Therefore, the required dimensions of the plate attachment modes are too large and prevent us from modeling the spiral with plates. It deserves mention that there is no size

limit on the conducting plates themselves. Possibilities for future work include an investigation into the possibility of either shrinking the size requirements on the wire to plate attachment modes or feeding the plates directly thus negating the need for attachment modes.

We proceed to model the Archimedean spiral with thin wires. This, however, is not without complications. ESP incorporates a thin wire approximation which the ESP documentation [17] notes may lead to inaccurate results for wire radii exceeding 0.01λ. For conductor widths of 0.03 inch, the wires used to model the spiral must have radii of $a = 0.015$ inch. Thus, the thin wire condition is violated for frequencies greater then 7.87 GHz where $a = 0.01\lambda$. For this reason, results obtained from ESP for frequencies greater then about 7.0 GHz must be viewed with suspicion.

We used an approximation to the Archimedean spiral design of Section 4.1 consisting of 722 straight wire segments. The approximate spiral, located in the xy-plane, is shown in Fig. 4.4-1. All wires have radii of 0.015 inch and are spaced 0.03 inch apart in a self-complementary structure. The feed attachment plates at the center of the spiral of Fig. 4.1-1 are approximated by two wire segments parallel to the x-axis. The spiral is fed by a delta gap generator placed at the connection point between these two segments. The feed segments form a convenient reference point for defining polarization. We define vertical polarization as being parallel to the x-axis and hence parallel to the feed segments. Horizontal polarization is then defined as being parallel to the y-axis and hence at 90 degrees to the feed segments.

Numerical results obtained from ESP over the two octave frequency range between 2.5 GHz and 10 GHz are presented in Table 4.4-1. A plot of input impedance magnitude versus frequency is shown in Fig. 4.4-2. It may be noted that at about 4 GHz the input impedance begins a sharp increase. This effect is most likely due to the thin wire approximations made by ESP. We know that the results for frequencies above 7.87 GHz

are suspect; therefore, being cautious, we will ignore impedance results for frequencies greater than 7.0 GHz throughout the rest of this work. Over the two octave bandwidth, the maximum gain for horizontal polarization varies by only 1.87 dB, and the maximum gain for vertical polarization varies by 2.8 dB. In this respect the performance of the spiral is relatively constant over the two octave bandwidth. A plot of maximum gain versus frequency is shown Fig. 4.4-3. Radiation patterns predicted by ESP are discussed in Chapter 7 where they are presented versus the corresponding measured patterns. Comments on what effects the thin wire approximations made by ESP have on the impedance and pattern calculations will be discussed further with the presentation of measured data in Chapter 7.

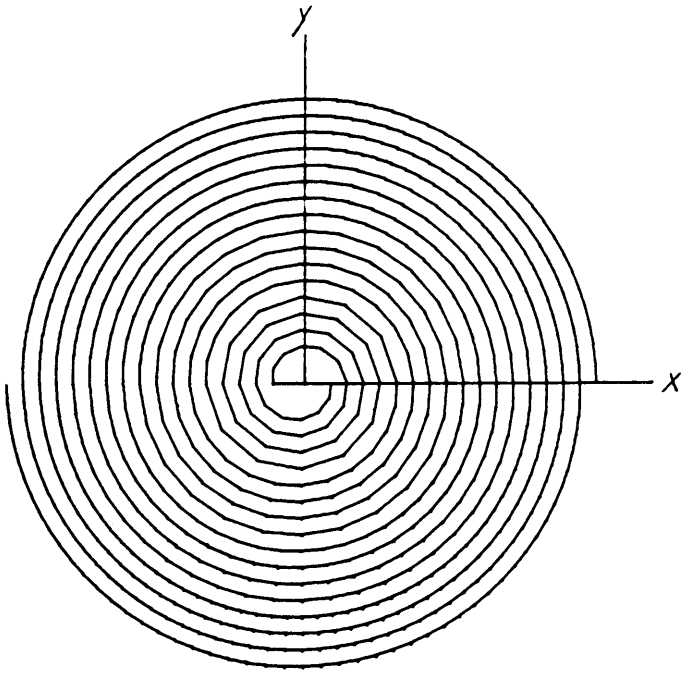

Figure 4.4-1. Archimedean spiral modeled by 722 straight wire segments for use with ESP. The parameters of this spiral are given in Section 4.4.

Table 4.4-1

Numerical Results Obtained From ESP

Frequency (GHz)	Gain (dB) Horizontal	Vertical	Input Impedance (ohms)
2.5	1.35	0.43	139.363 + j8.477
3.0	1.72	0.47	125.442 - j22.721
4.0	1.91	1.56	110.458 + j43.868
5.0	2.37	2.22	127.783 + j54.494
6.0	2.61	2.85	140.823 + j84.610
7.0	2.86	3.15	176.068 + j106.862
8.0	3.07	3.23	218.132 + j111.146
9.0	3.21	3.07	258.311 + j100.673
10.0	3.22	2.77	292.980 + j78.481

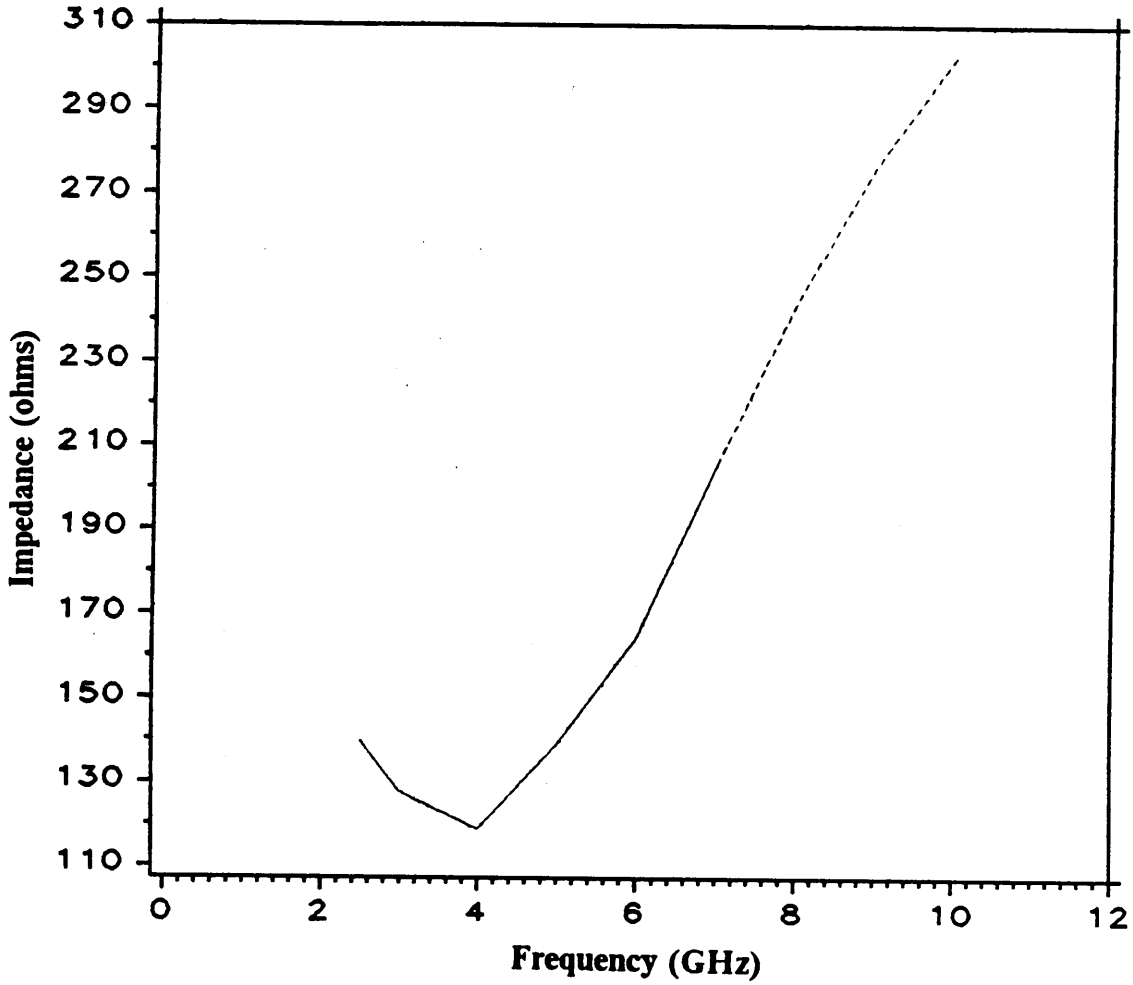

Figure 4.4-2. Input impedance of the spiral in Fig. 4.4-1 versus frequency calculated using ESP.

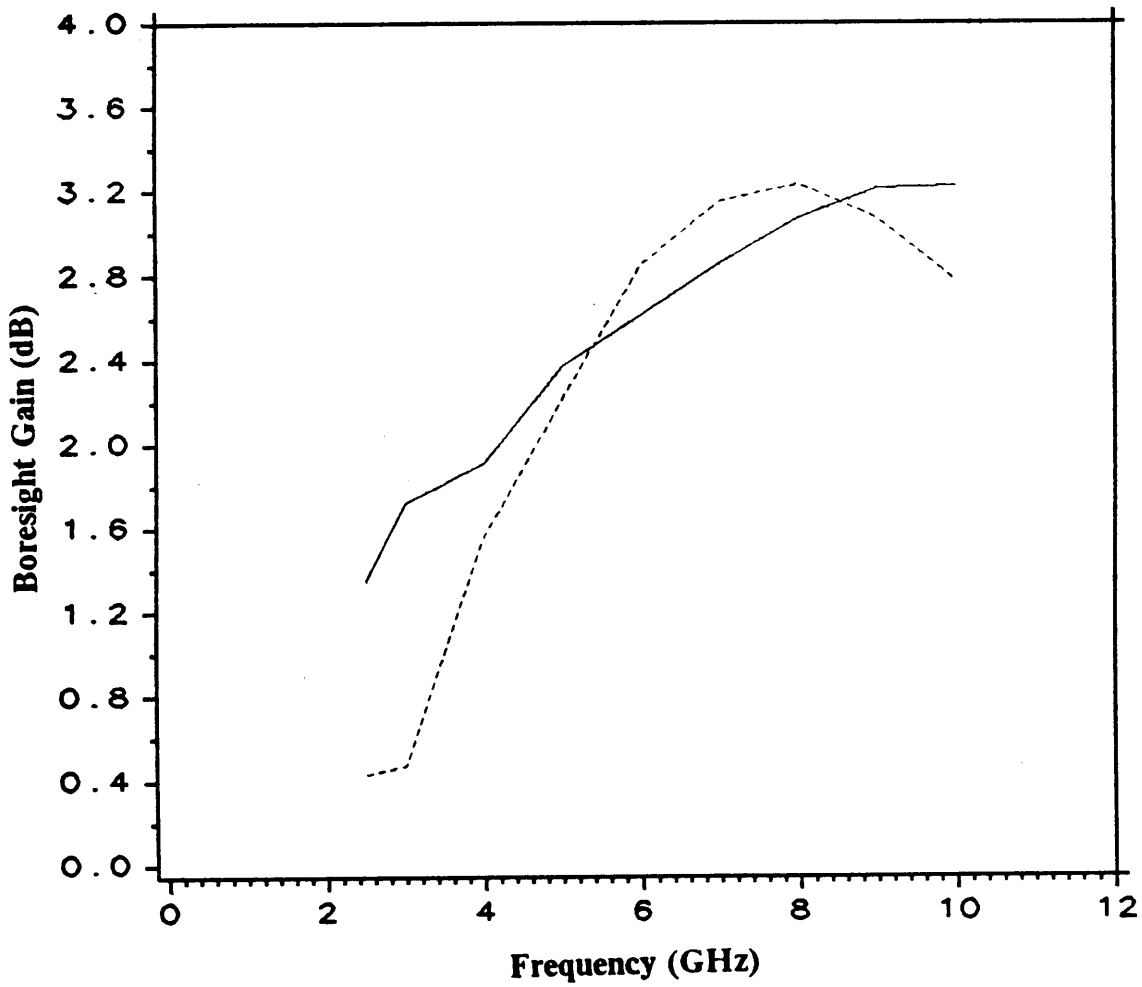

Figure 4.4-3. Maximum (boresight) gain versus frequency. Horizontal polarization-solid; vertical polarization-dashed.

V. Construction of the Archimedean Spiral

The material used to construct the Archimedean spiral is RT/duroid, which is manufactured by the Rogers corporation. RT/duroid may be obtained in a variety of sizes, shapes and materials. We used RT/duroid model 5870, which consists of 20.0 mils of teflon substrate with a dielectric constant of $\varepsilon_r = 2.35$ sandwiched between two sheets of copper each approximately 5.0 mils thick. The construction process involves etching away excess copper until the desired copper pattern remains. The etching process hinges on the the chemical photoresist which is produced by Shippley Inc. Photoresist is baked onto the copper surface of the RT/duroid and selective portions are exposed to ultraviolet light. The ultraviolet light causes a chemical change in the photoresist. When the RT/duroid is then imerrsed in photodeveloper, also produced by Shippley, the photoresist which had been exposed washes away while the unexposed photoresist is not affected. The RT/duroid is then rebaked, in order to harden the photoresist, and submersed in a printed circuit board etchant. The etchant dissolves copper, but does not affect teflon or photoresist. Thus the photoresist allows us to control which portions of copper are etched away.

The steps by which the Archimedean spiral was constructed are shown in Fig. 5.0-1. The first step is to etch into a sheet of rubylith (a material commonly used for silk screening) a negative image of the desired spiral enlarged to ten times its final size. The image on the rubylith is then reduced photographically so that the photographic negatives contain a positive image of the spiral reduced to its final size. In order to proceed, a sheet of RT/duroid must be prepared. This is done by evenly coating one side with photoresist and baking at 90° C for 10 minutes. The negative containing the image of the spiral is then placed over the the RT/duroid and the face is exposed to ultraviolet light. Next, the RT/duroid is submersed in photodeveloper and the portions of photoresist which were exposed to the ultraviolet light are washed off. The only photoresist remaining on the RT/duroid corresponds to the desired spiral pattern. At this point the remaining photoresist is hardened by baking the RT/duroid at 110° C for 15 minutes. The RT/duroid is submersed in printed circuit board etchant, and all copper not protected by the hardened photoresist is etched off. This includes all of the copper on the side of the RT/duroid opposite to the spiral. The remaining hardened photoresist is then washed off with acetone, and an Archimedean spiral of 5.0 mils of copper backed by a 20.0 mils of teflon remains.

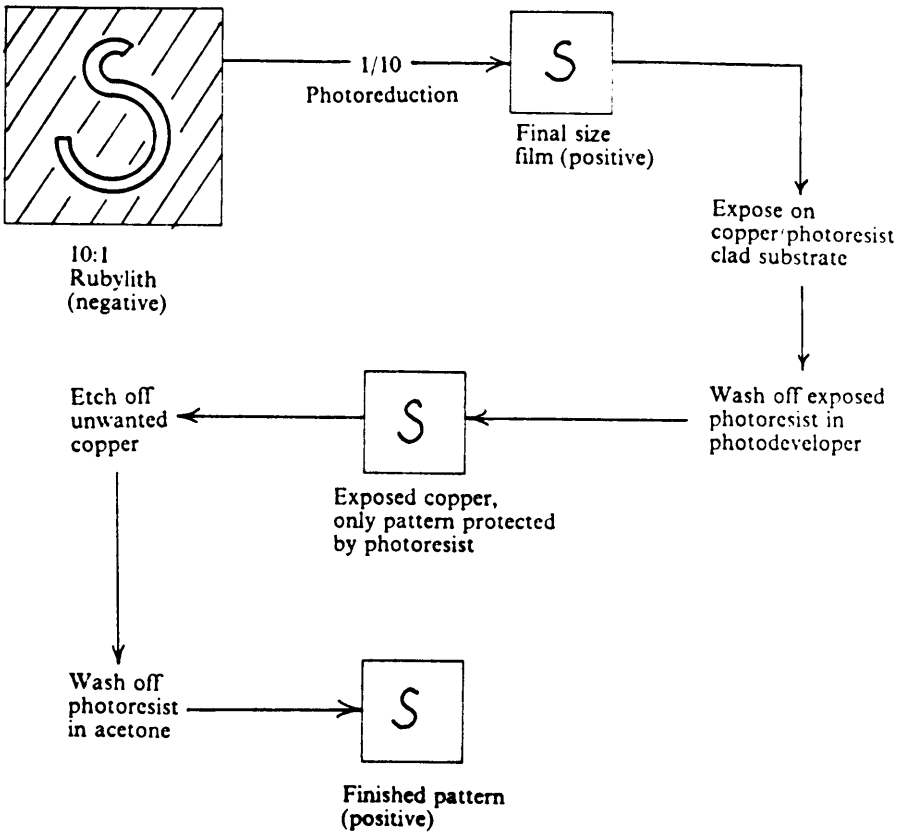

Figure 5.0-1. Archimedean spiral construction process.

VI. Feed Details of the Archimedean Spiral

Coaxial cable of 50 ohm characteristic impedance is readily available, inexpensive and compatible with the existing equipment at our antenna range. For these reasons, we decided to use RG 402 simi-rigid coax with 50 ohm characteristic impedance in the feed network of the Archimedean spiral; however, this choice presents us with two problems. The first problem is impedance mismatch. Ignoring the results obtained by ESP for frequencies greater then 7 GHz, where the thin wire approximations used by ESP lose validity, the numerical results of Chapter 4 indicate that we can expect the Archimedean spiral to exhibit an input impedance magnitude between 118.8 and 205.9 ohms. For this impedance range the mismatch between the antenna and the 50-ohm coax leads to a reflection coefficient in the range of $|\Gamma| = 0.41$ to $|\Gamma| = 0.61$, which is unexceptablly high. To reduce reflections, a wideband impedance transformer is needed to match the spiral to the feed network. The second problem is that for proper operation the currents on the arms of the spiral must be of equal amplitude and opposite phase. If this balanced condition is not met, the resulting current distribution on the spiral will be composed of two components. One component is the desired currents with equal amplitude and opposite phase at the input to the spiral; this is the $M = 1$ normal

mode of excitation as defined in Section 2.0. For this mode the active region, as defined in Section 2.0, has a one wavelength circumference, producing a pattern with a maximum on boresight and a 360 degree phase change per spiral revolution. The other component is an inphase component in which the currents at the input to the spiral are equal in amplitude and phase. For this case the first active region occurs at the input terminal of the spiral and does not significantly contribute to radiation. The primary source of radiation is the second active region. As discussed in Section 2.0 this active region has circumference $(M+N)\lambda$ where M is the normal excitation mode and N is the number of arms in the spiral. For the case considered here, $M=0$ and $N=2$. Therefore, $(M+N)=2$ and the primary source of radiation is an active region of circumference 2λ. The radiation pattern produced by this active region possess a null on axis and a 720 degree phase change per spiral revolution. The total field radiated by these two current components, obtained by superposition, is characterized by beam squinting, or pointing of the beam other than along the axis of the spiral [11]. The amount of squint is dependent upon the relative amplitude of the two modes while the direction is dependent on the relative phase. Beam squinting can be prevented by a wideband balun (contraction for "balanced" to "unbalanced") which will be discussed in the following section.

J.W.Duncan and V.P.Minerva [12] have introduced a wideband balun transformer which may be used to match the Archimedean spiral to a 50-ohm coaxial line and which will prevent beam squinting. Balun design is discussed next.

6.1 The Wideband Balun Transformer.

A diagram of the wideband balun transformer [12] is shown in Fig. 6.1-1. It is made by cutting a slot in the outer conductor of the coax so that a cross sectional view shows an open sector in the outer wall. The angle subtended by the open sector is denoted by 2α. Along the axis of the balun the angle 2α varies continuously from zero to almost 2π. The result is a transition from coax to an open two conductor transmission line, accompanied by a corresponding impedance transformation.

A balanced two-conductor transmission line has equal currents of opposite phase along the conductors for any cross section, resulting in a zero net current flow. System unbalance is typified by the addition of a codirectional component to the balanced current. The result is that a nonzero net current may occur. In a coaxial line balanced transmission conditions occur between the center conductor and the inside of the outer conductor. If the inside and outside of the outer conductor are not isolated from each other at the load, current may be shunted by the load to the outside of the coax resulting in system unbalance.

Consider the case of the balun transformer of Fig. 6.1-1. Over the length of the transformer the field changes from the totally confined field in the coax to the open field of the two wire transmission line. Any unbalance in the current on the surface of the coax must result from the summation of reflected waves throughout the transmission region. By making the slot transition gradual, the reflections may be made arbitrarily small, resulting in a negligible current unbalance. Thus, the slot transition region provides isolation from the outside of the coax.

The design procedure used for the slot transition region has been adopted by Duncan and Minerava [12] from the procedure developed by Klopfenstein [13] for the

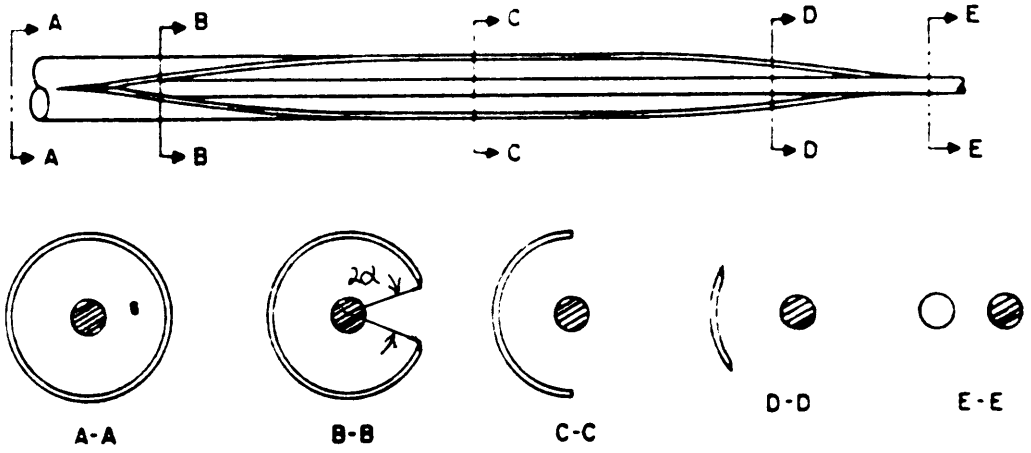

Figure 6.1-1.The wideband balun transformer.

design of tapered transmission-line matching sections. This is discussed in the next section.

6.2 *Analysis of the Wideband Balun Transformer*

Klopfenstein's method was originated as a way of designing tapered transmission-line matching sections such as that shown in Fig. 6.2-1. The objective is to obtain the impedance taper which requires the shortest transition region to match a transmission line of characteristic impedance Z_1 to a transmission line of characteristic impedance Z_2 for a given maximum input reflection coefficient.

For any transmission line, assuming all modes except the dominant mode are well below cutoff, the applicable equations are [13]

$$\frac{dV}{dx} = -ZI \quad \text{and} \quad \frac{dI}{dx} = -YV \tag{6.2-1}$$

where

V = the voltage across the transmission line,

I = the current in the transmission line,

Z = the series impedance per unite length of line,

and

Y = the shunt admittance per unite length of line.

The configuration to which the above equations are applied is shown in Fig. 6.2-1. For the nonuniform transition section between $x = \frac{-l}{2}$ and $x = \frac{l}{2}$ the quantities Z and Y are known functions of position along the line, and the properties of the system are

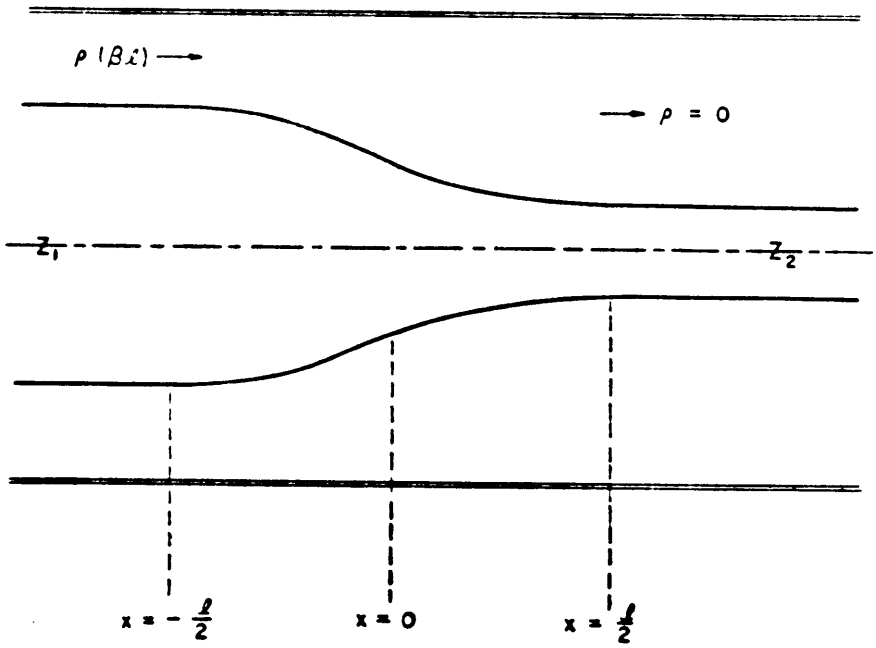

Figure 6.2-1. Tapered transmission-line matching section.

determined through the solution of (6.2-1) along with the appropriate boundary conditions [13].

We can put (6.2-1) in a more useful form which is in terms of the quantities of direct interest in impedance matching problems through the introduction of the quantities [13]

$\gamma = \sqrt{ZY}$ = the propagation constant of the line,

$Z_o = \sqrt{Z/Y}$ = the characteristic impedance of the line,

and

$\rho = \dfrac{V/I - Z_o}{V/I + Z_o}$ = the reflection coefficient at any point along the line.

These lead to the first order nonlinear differential equation

$$\frac{d\rho}{dx} - 2\gamma\rho + \frac{1}{2}(1 - \rho^2)\frac{d(\ln Z_o)}{dx} = 0 \tag{6.2-2}$$

Assuming $\rho^2 << 1$, (6.2-2) can be approximated by the first-order linear differential equation

$$\frac{d\rho}{dx} - 2\gamma\rho + F(x) = 0 \tag{6.2-3}$$

where $F(x) = \dfrac{1}{2}\dfrac{d(\ln Z_o)}{dx}$.

The solution of (6.2-3) which satisfies the boundary condition that $\rho = 0$ at $x = l/2$, for the case of a lossless transmission-line taper (the characteristic impedance is a real number independent of frequency), is [13]

$$\rho \exp(j\beta l) = \int_{-l/2}^{l/2} F(z) \exp(-j2\beta z)dz \tag{6.2-4}$$

which can be inverted through the theory of Fourier transforms to obtain

$$F(x) = 1/\pi \int_{-\infty}^{\infty} [\rho \exp(j\beta l)] \exp(j\beta x) d\beta \,. \tag{6.2-5}$$

Collin [14] has shown that optimum performance is obtained from a cascaded transformer structure when the power loss ratio is expressed in terms of a Tchebycheff polynomial of a degree equal to the number of sections. This is equivalent to having the input reflection coefficient, ρ, proportional to a Tchebycheff polynomial of the same degree, as long as $\rho^2 << 1$. Klopfenstein applies Collin's results to the continuous transformer section by using the limiting form of the Tchebycheff polynomial as its degree is increased without limit. This is given by [15]

$$\rho \exp(j\beta l) = \frac{\rho_o \cos[\sqrt{(\beta l)^2 - A^2}]}{\cosh A} \,, \tag{6.2-6}$$

where A is an arbitrary real constant and ρ_o is the reflection coefficient that would exist between the sections to be matched if no transformer section were used, that is

$$\rho_o = \frac{Z_2 - Z_1}{Z_2 + Z_1} \,. \tag{6.2-7}$$

The passband of (6.2-6) is defined as all frequencies such that the quantity under the radical is real, that is all frequencies where $(\beta l)^2 \geq A^2$. The low frequency cutoff is then defined as the frequency at which

$$\beta l = A \,. \tag{6.2-8}$$

The reflection coefficient, as given by (6.2-6), takes on its maximum value of $|\rho_o|$ at zero frequency and oscillates in the passband with a maximum amplitude given by

$$|\rho_{\max}| = \frac{\rho_o}{\cosh A} \,. \tag{6.2-9}$$

A plot of $|\rho/\rho_o|$ versus l/λ is shown in Fig. 6.2-2 for several values of A.

Substitution of (6.2-6) into (6.2-5) and integration leads to the following equation relating the impedance at any position in the transition region to A [13]:

$$\ln(Z_o) = \frac{1}{2}\ln(Z_1 Z_2) + \frac{\rho_o}{\cosh(A)}\left\{A^2\phi(2x/l, A) + U(x-\frac{l}{2}) + U(x+\frac{l}{2})\right\}, \tag{6.2-10}$$

$$|x| \le \frac{l}{2},$$

$$= \ln(Z_2), \quad x > \frac{l}{2},$$

$$= \ln(Z_1), \quad x < \frac{l}{2} \,.$$

U is the unit step function defined by

$$U(z) = 0, \quad z < 0,$$
$$U(z) = 1, \quad z \ge 0, \tag{6.2-11}$$

and ϕ is defined by

$$\phi(z, A) = -\phi(-z, A) = \int_o^z \frac{I_1(A\sqrt{1-y^2})}{A\sqrt{1-y^2}}\, dy, \tag{6.2-12}$$

$$|z| \le 1$$

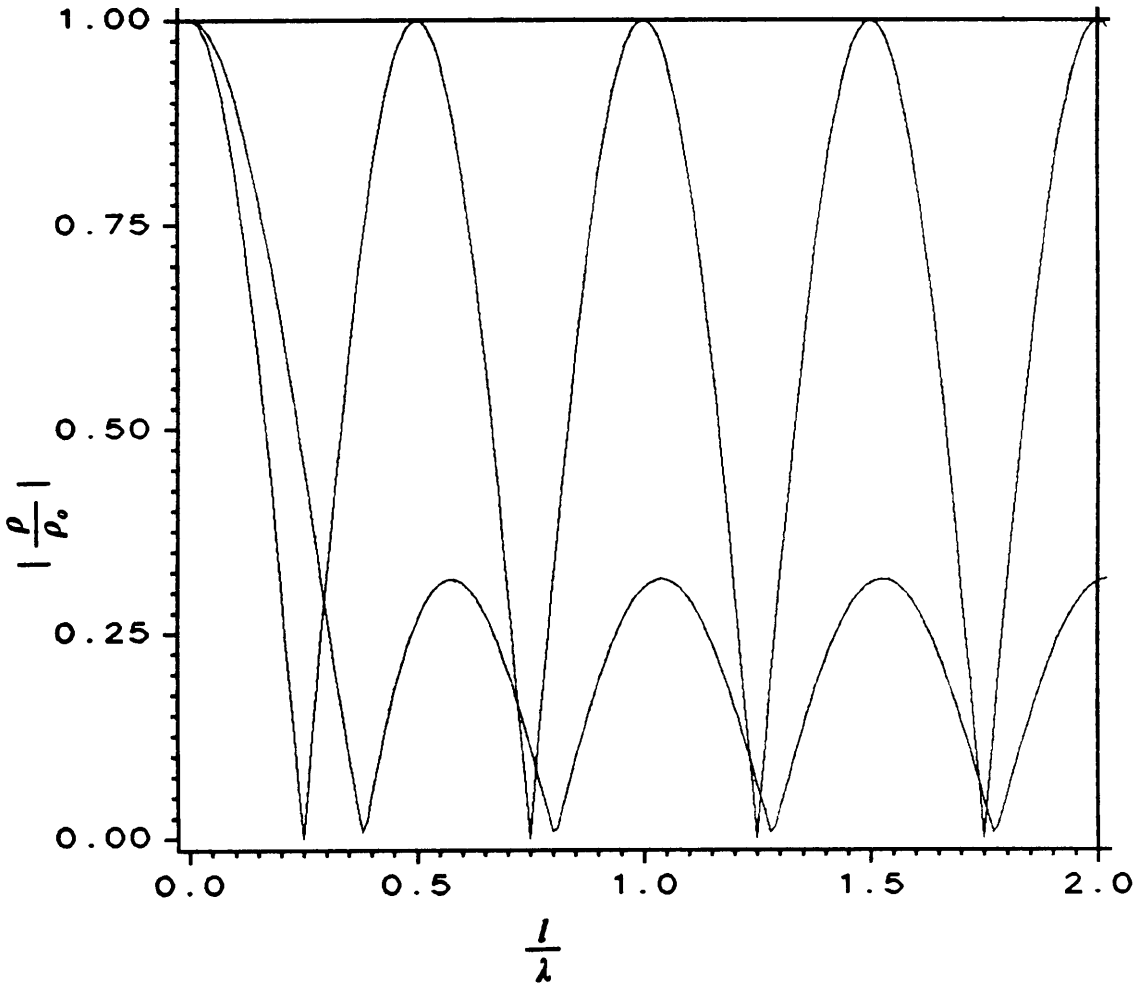

Figure 6.2-2. Reflection coefficient magnitude for three values of A as calculated from (6.2-6).

where I_1 = the first kind of modified Bessel function of the first order.

In the derivation of (6.2-10) the approximation that $\rho^2 << 1$ was used; the result of this approximation is that the impedance taper given by (6.2-10) does not perfectly match the values of Z_2 and Z_1 at either end of the taper. The magnitude of the discontinuities, and the inconvenience that they cause, may be reduced by setting [13]

$$\rho_o = 1/2 \ln(\frac{Z_2}{Z_1}) . \tag{6.2-13}$$

This value of ρ_o will not be significantly different from the value of ρ_o as given by (6.2-7).

By specifying the maximum acceptable magnitude of input reflection coefficient in the passband, (6.2-6) is used to find the corresponding value of A and (6.2-10) through (6.2-12) are used to find the required impedance taper of the transition region (i.e. $Z_o(x)$).

It is noted that the preceding was derived in reference to the tapered line transition of Fig 6.2-1; however, Duncan and Minerava [12] have experimentally shown that the results can be successfully applied to the slot transition region of the wideband balun transformer of Fig. 6.1-1. Therefore, having obtained the impedance taper, all that is needed in order to design the wideband balun transformer is the relation between the slot width and the impedance at any cross section along the transition region. This problem has not been solved exactly; however, Duncan and Minerava [12] have obtained upper and lower bounds to the exact impedance at any cross section along the transition region.

The upper bound is given by the equation

$$Z_{ou} = \frac{1}{2\pi}\sqrt{\frac{\mu}{\varepsilon}}\ln\frac{b}{a}$$

$$\frac{\sqrt{\frac{\mu}{\varepsilon}}}{\pi(\pi-2)^2}\sum_{n=1}^{\infty}\frac{\sin^2(n\alpha)[1+\frac{c_1 n^2}{n^2-k^2}]^2}{n^3[1+coth(n\ln\frac{b}{a})]}\ ohms \qquad (6.2\text{-}14)$$

where

$$-c_1 = \frac{\sum_{n=1}^{\infty}\frac{\sin^2(n\alpha)}{n(n^2-k^2)[1+coth(n\ln\frac{b}{a})]}}{\sum_{n=1}^{\infty}\frac{n\sin^2(n\alpha)}{(n^2-k^2)^2[1+coth(n\ln\frac{b}{a})]}} \qquad (6.2\text{-}15)$$

and a and b are the radii of the inner and outer conductors of the coax from which the balun is constructed. The lower bound may be obtained by the equation

$$Z_{ol} = \frac{\frac{1}{2\pi}\sqrt{\frac{\mu}{\varepsilon}}\ln(\frac{b}{a})}{1-\frac{4}{5}(\frac{\alpha}{\pi})c_1} \qquad (6.2\text{-}16)$$

where

$$\frac{1}{c_1} = \frac{4}{5}(\frac{\alpha}{\pi}) + \frac{40}{\pi}\ln(\frac{b}{\alpha})\sum_{n=1}^{\infty}$$

$$\frac{[1+coth(n\ln\frac{b}{a})]}{(n\alpha)}\left[\frac{A_n\cos(n\alpha)-B_n\sin(n\alpha)}{(n\alpha)^4}\right]^2 \qquad (6.2\text{-}17)$$

$$A_n = (n\alpha)^3 - 6(n\alpha),$$

$$B_n = 3(n\alpha)^2 - 6.$$

The derivation of the upper and lower bounds assumes the same dielectric occupies the space between the conductor as exists on the outside of the coax. Because a balanced transmission line does not radiate, we assume that most of the field exists between the two conductors. For this case the value of $\frac{\mu}{\varepsilon}$ in (6.2-14) and (6.2-16) refers the properties of the medium between the two conductors only.

Experimental data presented by Duncan and Minerava [12] show that the actual impedance is closely approximated by the average of the upper and lower bounds. Hence, for design purposes we will use

$$Z_o = \frac{Z_{ou} + Z_{ol}}{2}. \tag{6.2-18}$$

The following is a summary of the procedure used to design a wideband balun transformer to match a coaxial transmission line of characteristic impedance Z_1 to a two wire transmission line of characteristic impedance Z_2 where both Z_1 and Z_2 are real: The first step is to specify $|\rho_{max}|$, the maximum acceptable magnitude of input reflection coefficient in the passband. Next (6.2-13) is used to calculate ρ_o, the reflection coefficient magnitude which would exist if there were no impedance transformer section to match Z_1 to Z_2. Having obtained $|\rho_{max}|$ and ρ_o, (6.2-9) is used to calculate the necessary value of A. Using the values of Z_1, Z_2, ρ_o and A , (6.2-10) through (6.2-12) are used to calculate the impedance taper ($Z(x)$ for $-l/2 \leq x \leq l/2$) needed to produce an input reflection coefficient, ρ, whose magnitude possess the desired Tchebycheff response with frequency. Having obtained the impedance taper, the next step is to calculate the slot which provides the impedance taper throughout the transition region. This is accomplished by using (6.2-14) through (6.2-18) which provide the upper bound,

lower bound and average value of the characteristic impedance of the sloted coax for a given value of 2α, the subtended angle of the slot as shown in Fig. 6.1-1. For our design we use the average value. The information needed about the coax in order to use (6.2-14) through (6.2-18) are the values of μ and ε of the dielectric material loading the coax and the ratio b/a, where b is the inside diameter of the outer conductor and a is the diameter of the inner conductor. It is noted that if we know μ, ε and the rated characteristic impedance of the coax Z_o, then b/a can be calculated through the equation [20]

$$Z_o = \frac{1}{2\pi}\sqrt{\frac{\mu}{\varepsilon}}\ln(b/a). \qquad (6.2-19)$$

All that is needed to complete the design is the required length of the transition region l. This is found by specifying the low frequency cutoff, f_c, and using (6.2-8) where $\beta = \frac{2\pi}{\lambda_c}$ (λ_c is the guided wavelength at the cutoff frequency f_c).

To aid in the design of the balun two computer programs have been written in FORTRAN. The first program, referred to as the Impedance Taper Code (ITC), uses (6.2-9) through (6.2-12) to calculate the impedance taper needed to match an impedance Z_1 to an impedance Z_2 for specified values of $|\rho_{max}|$ and ρ_o. ITC is presented in appendix A. The second program, called the Impedance Versus Subtended Angle Code (IVSAC), uses equations (6.2-14) to (6.2-18) to calculate the upper bound, lower bound and average value of the impedance of the sloted coax verses the subtended angle, 2α. The input parameters are the characteristic impedance of the coax, Z_o, and the relative dielectric constant, ε_r, of the medium between the two conductors in the coax. IVSAC is presented in Appendix B.

The following is a stepwise procedure which makes use of ITC and IVSAC for the design of the wideband balun transformer transition region for specified values of $|\rho_{max}|$, Z_1, Z_2 and f_c:

1. Use (6.2-13) to to calculate ρ_o.

2. For the specified values of $|\rho_{max}|$, ρ_o, Z_1 and Z_2, ITC is used to obtain a plot of the impedance taper ($Z(x)$ for $-l/2 \leq x \leq l/2$)

3. For the specified values of ε_r and Z_o of the coax from which the balun is to be constructed, IVSAC is used to obtain a plot of characteristic impedance versus the subtended angle of the slot 2α.

4. Using the plot of characteristic impedance versus length found in step 2 and the plot of characteristic impedance versus 2α found in step 3, values for 2α versus relative length along the transition region are obtained ($2\alpha(x)$ for $-l/2 \leq x \leq l/2$).

5. Finally, A is found using (6.2-9) for the specified values of $|\rho_{max}|$ and ρ_o. This value for A , along with the guide wavelength λ_c which corresponds to the cutoff frequency f_c, are used in (6.2-8) to calculate the transition region length l. Using the length l and the results of step 4, a plot of 2α versus absolute length along the transition region can be obtained. The method by which the wideband balun transformer can be constructed from this information is discused at the end of Section 6.3.

6.3 Complete Design of a Wideband Balun

In this section, the design of the wideband balun transformer used to match the spiral antenna of Section 4.1 to a coaxial cable with a 50 ohm characteristic impedance is presented. For this design, a transition between 50-ohm coaxial line and 125-ohm two conductor line was selected. It is noted that this may not be enough of a transition as the predictions by ESP, ignoring frequencies greater than 7.0 GHz, place the input impedance magnitude of the spiral in the range between 118.8 and 205.9 ohms; however, a preliminary investigation has shown that a larger impedance transformation would require an excessivly large slot width at the end of the transition region for the coax that we are using. It was decided that the cut off frequency, as given by (6.2-8), should be 2.0 GHz, and that the input reflection coefficient, ρ, should not exceed $\rho_o/20$, or $|\rho/\rho_o| \leq 0.05$.

We begin by using (6.2-13) to calculate ρ_o, this gives

$$\rho_o = \frac{1}{2}\ln(2.5) = 0.458\,, \tag{6.3-1}$$

which leads to $\rho = 0.023$.

ITC was run with $\rho_o = 0.458$, $|\rho_{max}| = 0.023$, $Z_1 = 50$ and $Z_2 = 125$; the resultant impedance taper is shown in Fig. 6.3-1. It should be noted that while the taper still exhibits discontinuities at both ends due to the approximation that $\rho^2 << 1$, the magnitude of the discontinuities have been reduced by using (6.2-13) rather than (6.2-7) in the calculation of ρ_o.

The balun is to be manufactured from RG 402 semi-rigid coax with a 50 ohm characteristic impedance. The coax is filled with teflon with a dielectric constant of 2.1.

For these values IVSAC is used to calculate the impedance verses subtended angle, 2α. The results are shown in Fig. 6.3-2.

To complete the design, the overall length of the balun, l, is needed. For $|\frac{\rho}{\rho_o}| = 0.05$, (6.2-9) leads to

$$\cosh(A) = 20 \quad \text{or} \quad A = 3.68835.$$

The low frequency cutoff has been defined as the frequency at which $\beta l = A$, with $\varepsilon_r = 2.1$ and a low frequency of 2.0 GHz, we have

$$l = 2.392 inches. \tag{6.3-2}$$

To summarize, Fig. 6.3-1 is used to find the impedance versus position, $\frac{x}{l}$, along the balun. Fig. 6.3-2 which shows the angle 2α versus impedance can then be used to obtain the relation between 2α and position $\frac{x}{l}$ along the balun. Finally, (6.3-2) is used to find the angle 2α versus distance along the balun given in inches. This is shown in Fig. 6.3-3.

The balun is constructed by first removing the inner conductor and teflon as one unit from the outer conductor. Next the radius of the outer conductor is measured. The radius of the outer conductor, along with the value of 2α versus length along the transition region as given in Fig. 6.3-3, allows us to project the geometry of the slot onto a sheet of paper. This projection is then wrapped around the outer conductor, and by carefully cutting along its edges it is possible to obtain a close approximation to the desired slot geometry. The inner conductor and teflon are then replaced and the construction is completed. While this procedure is simple in theory, it is not easy in practice and some variation from the calculated reflection coefficient is expected. Measured results obtained from the balun are presented in Chapter 7.

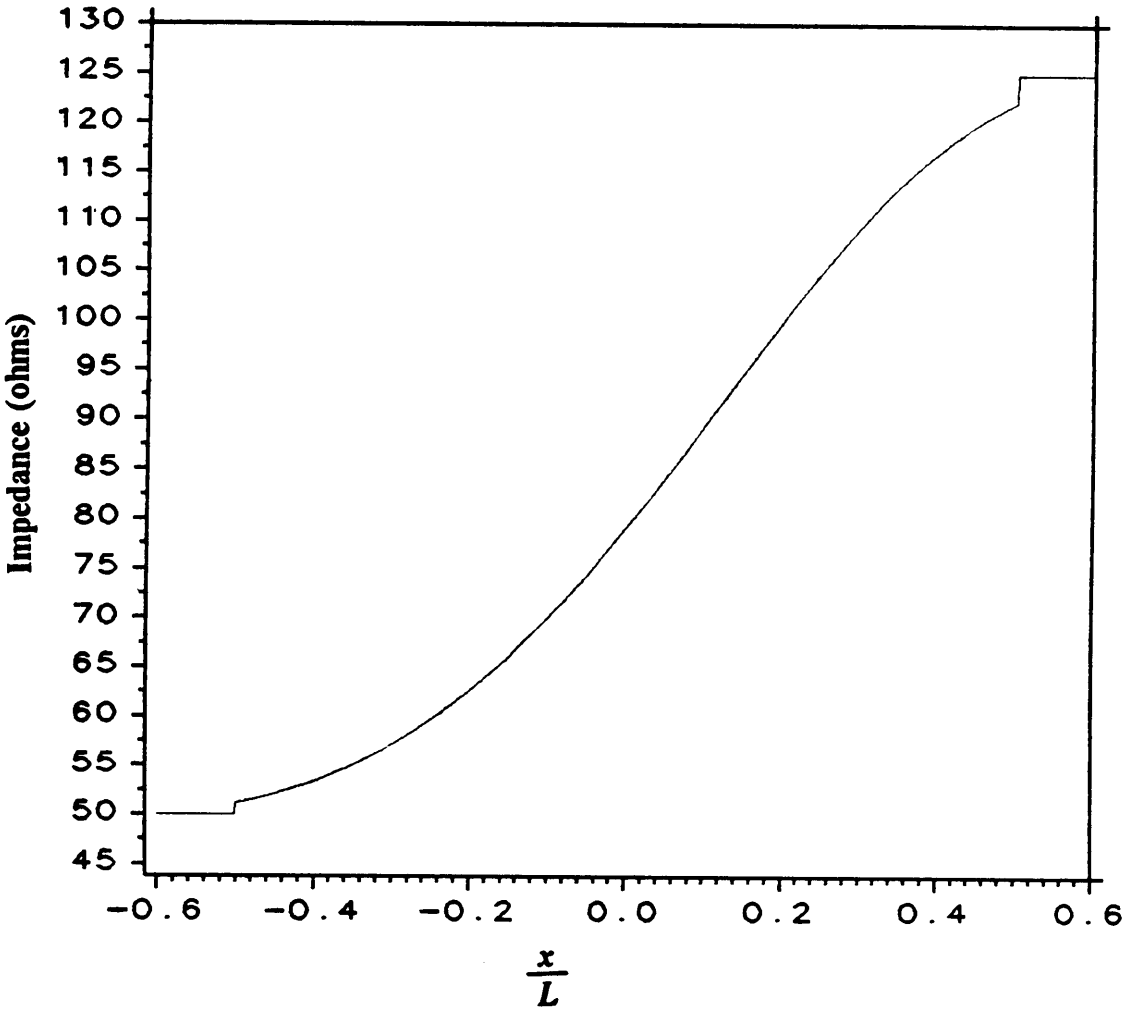

Figure 6.3-1. Impedance taper calculated using ITC and used in the wideband balun transformer design of Section 6.3.

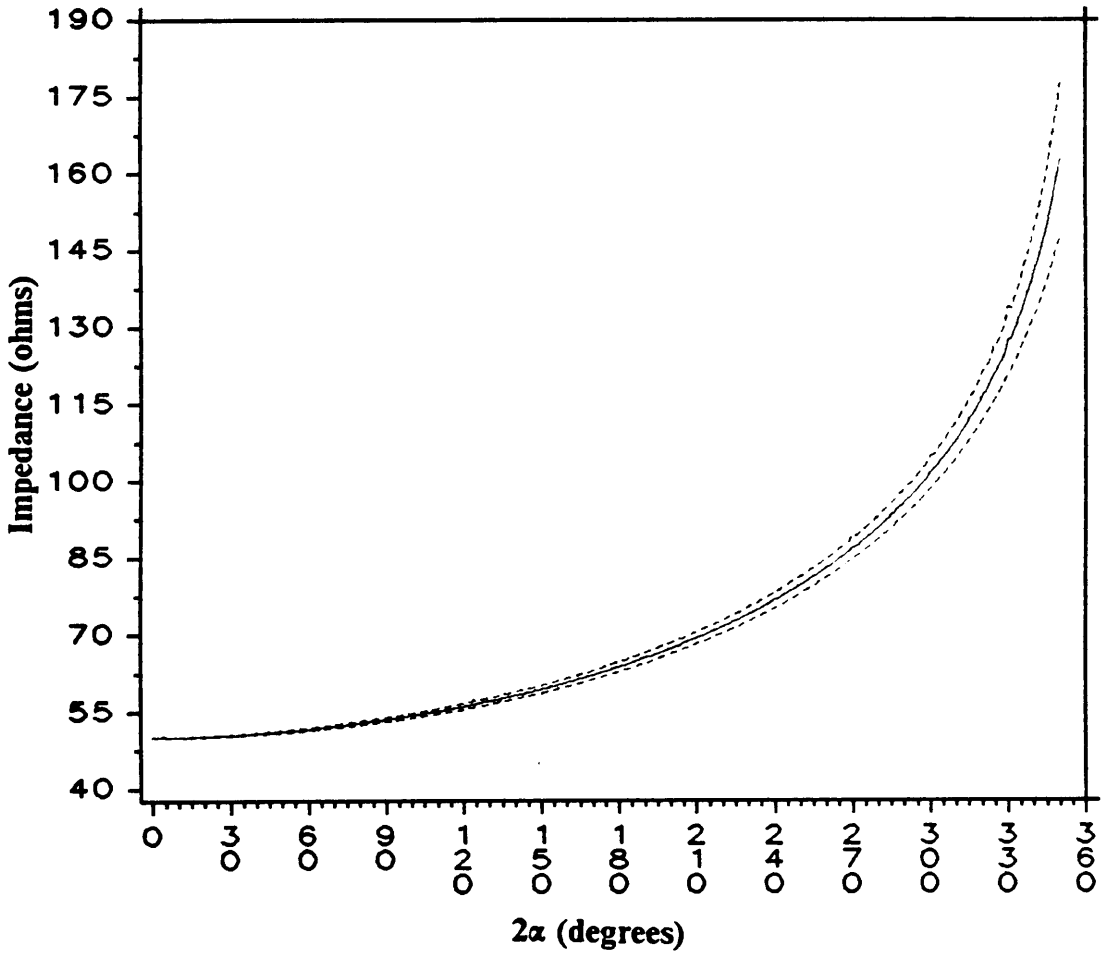

Figure 6.3-2. Upper, lower and average impedance vs subtended angle as calculated using IVSAC. The average value is used in the wideband balun transformer design of Section 6.3.

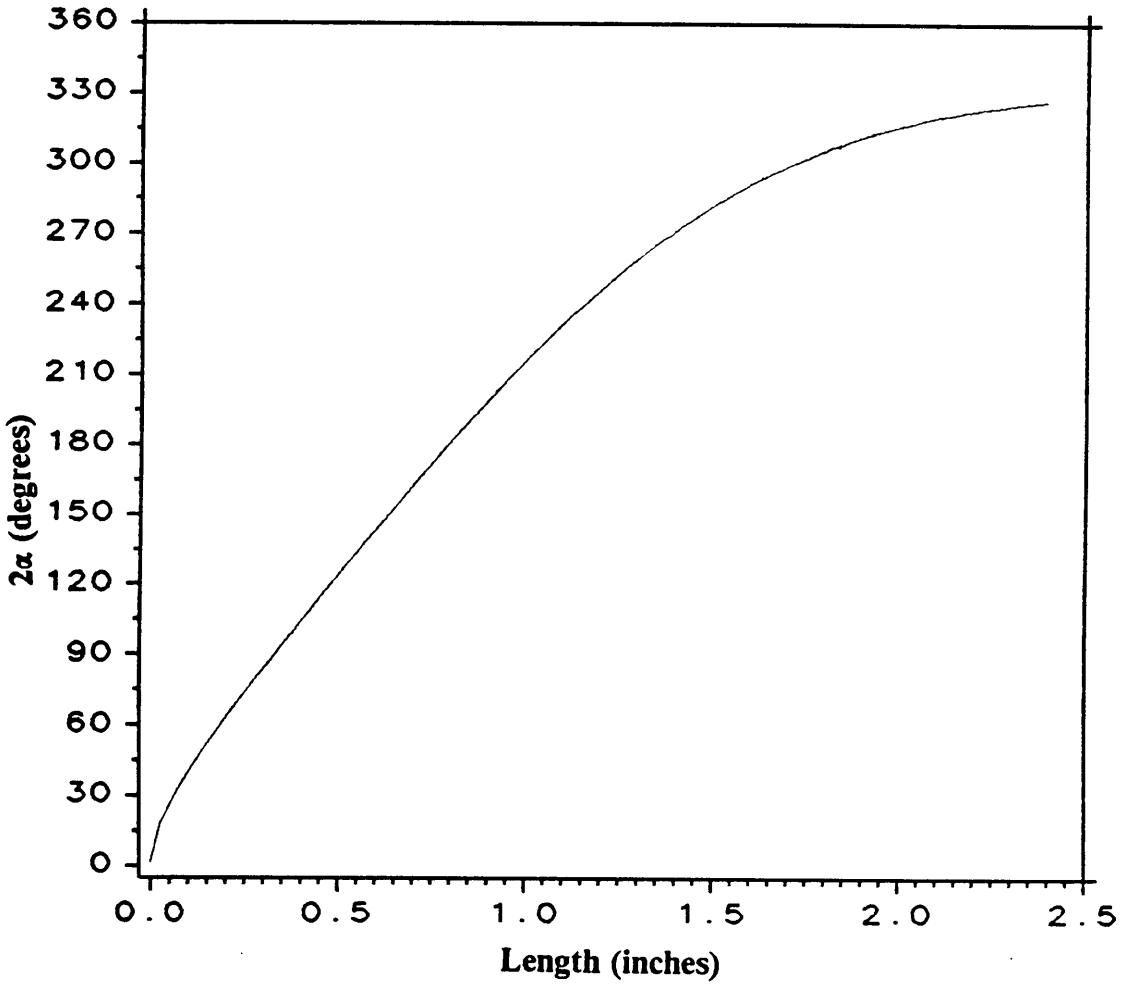

Figure 6.3-3. Distance vs subtended angle used in wideband balun transformer design of Section 6.3.

VII. Results

In Chapters 4 and 5 the design and construction of an Archimedean spiral antenna were discussed. In this Chapter measured results from the antenna will be presented. Before performing measurements, the balun transformer which was designed in Section 6.3 was connected to the spiral designed in Section 4.1. The balun was attached to the spiral by drilling a small hole through each of the feed attachment plates shown in Fig. 4.1-1 and inserting the leads of the balun through the holes from behind the spiral. The leads are held in place by solder placed on top of each plate covering the protruding lead ends. The balun extends behind the spiral perpendicular to the plane of the spiral. The coaxial end of the balun is fitted with a 50-ohm female SMA connector so that the spiral-balun system can easily be attached to 50-ohm measurement networks.

7.1 Impedance Measurements

Impedance information can be obtained from the S_{11} reflection coefficient (which is the same quantity we called ρ in Chapter 7). If Z_o is the characteristic impedance of the feed network used in the measurement, and Z_a is the input impedance of the antenna fitted with the balun, the reflection coefficient is given by

$$S_{11} = \frac{Z_a - Z_o}{Z_a + Z_o} \tag{7.1-1}$$

If the spiral-balun impedance is perfectly matched to the feed network, the magnitude of the measured S_{11} coefficient will be zero. Likewise, if the difference between Z_a and Z_o is large, a large value for S_{11} is measured.

The S_{11} reflection coefficient is measured using a Hewlett-Packard 8410 network analyzer. The feed consists of 50-ohm coaxial cable. It is desirable to make the measurements under similar circumstances to which the pattern measurements will be made. When making pattern measurements, we will only be interested in the forward directed radiation. Therefore, in order to prevent the pattern from being affected by scattering from the balun and feed structure, the spiral is backed by absorber. The face of the absorber measures eight inches on each side and the depth measures five inches. This absorber backing is included while performing the S_{11} coefficient measurements to assure that its presence does not adversely affect the operation of the balun transformer. To prevent reflected radiation from interfereing with the measurements, absorber was also placed about fifteen inches in front of the the spiral. Measurements were made over the frequency range between 500 MHz and 12.0 GHz. The results of the measurements are shown in Fig. 7.1-1 and Fig. 7.1-2.

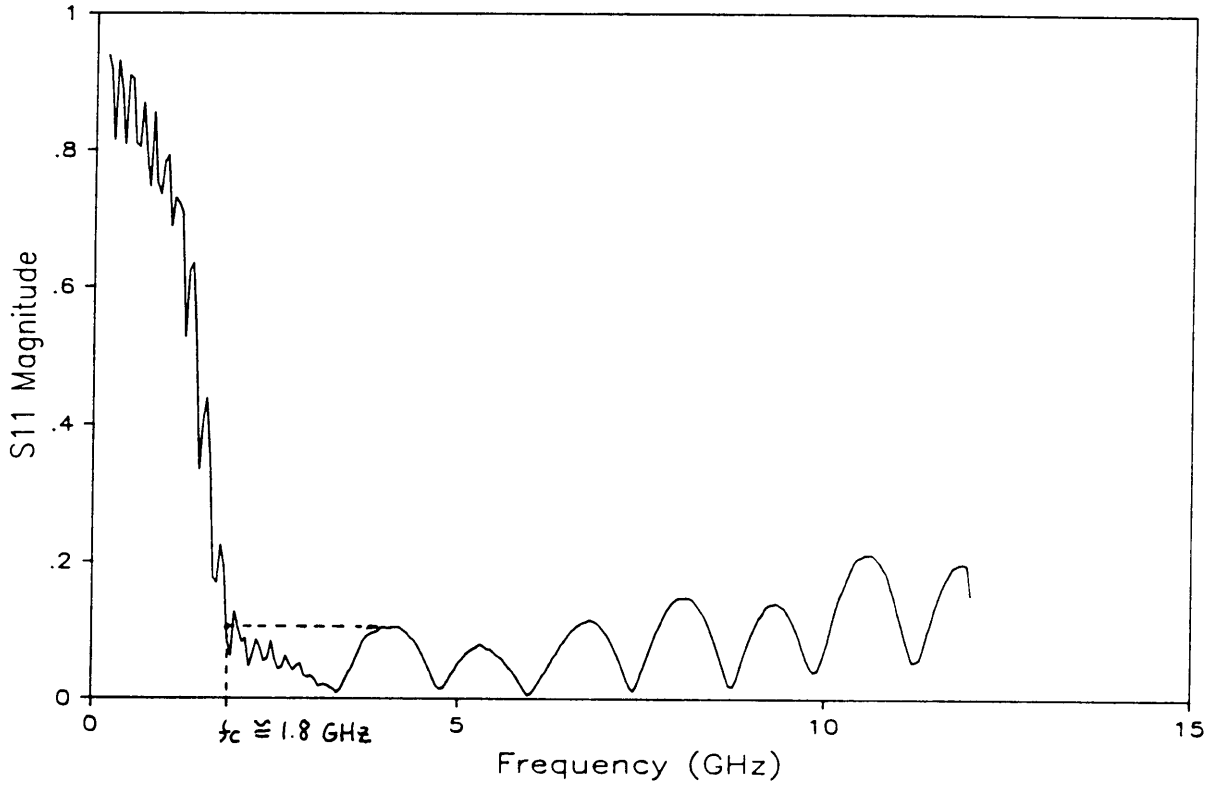

Figure 7.1-1. Reflection coefficient magnitude versus frequency for the spiral of Section 4.1 connected to the balun of Section 6.3.

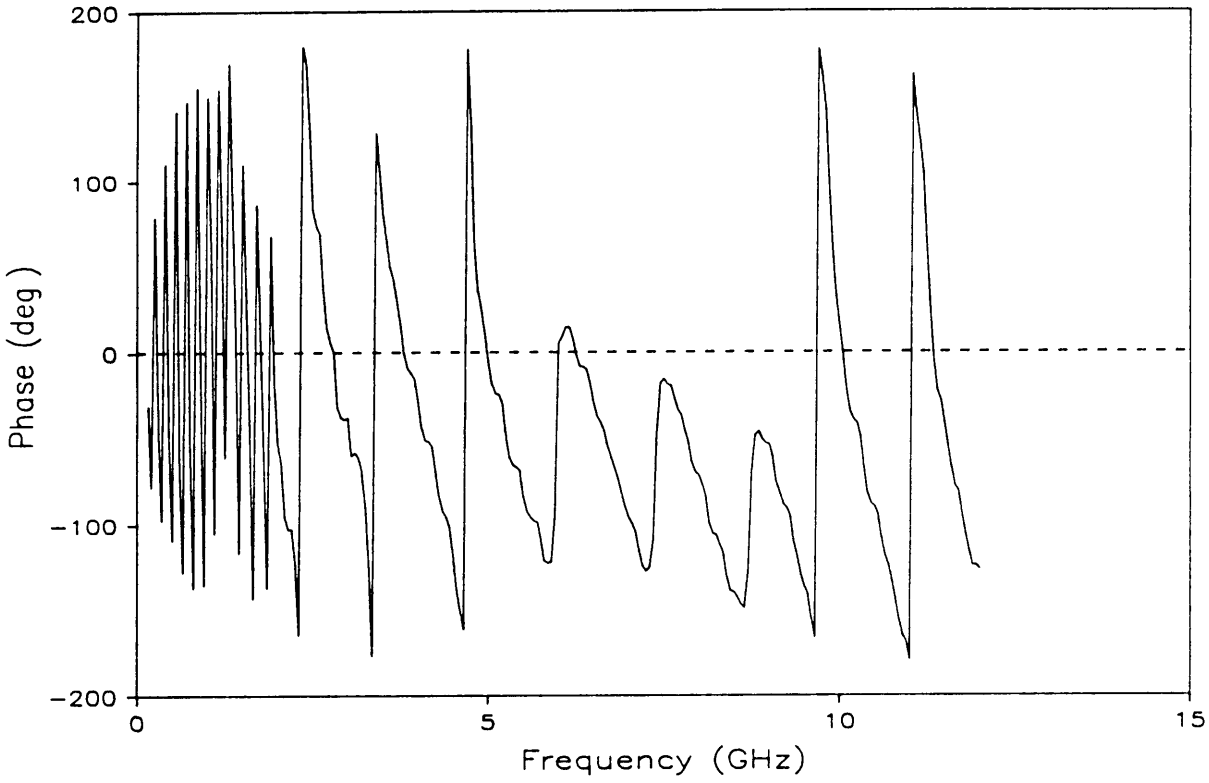

Figure 7.1-2. Reflection coefficient phase versus frequency for the spiral antenna of Section 4.1 with the balun of Section 6.3.

Comparison of Fig. 7.1-1 and Fig. 6.2-2 verifies that the plot of the reflection coefficient amplitude versus frequency possesses the desired Tchebycheff characteristic in the passband. The balun transformer low frequency cutoff is defined by (6.2-8) as being the frequency at which $\beta l = A$ and in accordance with (6.2-3) is located at the point where the $|S_{11}|$ first goes through $\frac{\rho_o}{\cosh A}$, the peak amplitude of the oscillating $|S_{11}|$ in the passband. With reference to Fig. 7.1-1, an approximation to the low frequency cutoff can be found from the measured data graphically by drawing a horizontal line from the first $|S_{11}|$ peak in the passband back toward the lower frequency region to find the frequency at which $|S_{11}|$ first crosses this value. The balun we are using was designed to have a low frequency cutoff of 2.0 GHz. Fluctuations in the measured data of Fig. 7.1-1 make it hard to tell exactly where the cutoff frequency occurs, but as we have drawn it in Fig 7.1-1 it is at 1.8 GHz. Over the two octaves between 2.5 GHz and 10 GHz, the reflection coefficient magnitude peaks remain fairly constant, falling within the range of 0.05 to 0.15 with a gradual increase with frequency being observed. Although the magnitude peaks are larger then the design peak of 0.023, they are reasonable small for our purposes. A probable explanation for the difference is that the balun transformer was designed to match a 50-ohm coaxial cable to a 125-ohm two wire transmission line; the 0.023 peak was calculated for this case. Results from ESP, ignoring frequencies greater then 7.0 GHz where it is expected that the thin wire approximations made by ESP lead to errors, indicate that the magnitude of the input impedance for the Archimedean spiral antenna may be expected to fall in the range between 118.8 and 205.9 ohms. For this range of input impedances a reflection coefficient in the range of 0.025 to 0.24 can be expected at the junction between the 125-ohm two conducter output of the balun and the input of the spiral. Therefore, the larger measured reflection coefficient peaks are probably due to the impedance mismatch between the output of the balun transformer and the input to the spiral. While a gradual

increase in reflection coefficient magnitude is observed as frequency is increased, there is no evidence of the drastic increase in impedance at frequencies above 7.0 GHz as predicted by ESP (see Fig.4.4-2). Hence, we were correct in our assumption that the calculated impedance increase was the result of the thin wire approximations made by ESP which begin to lose validity at the higher frequencies. We are then justified for having ignored the impedance predictions made by ESP at frequencies above 7.0 GHz in our design of the wideband balun transformer in Chapter 6. Finally, it may be recalled that in the design equations of the balun transformer in Chapter 6 the approximation was made that the electric field was confined to the region between the two conductors, while this is not strictly true, the success of the experimental results appear to confirm that the approximation is a good one.

It should be mentioned that the previous impedance results, as well as the pattern and gain results which will be presented in the following sections, were made using the balun design of Section 6.3. This was not the case with the baluns used in the testing of the completed wideband switched array [1]. The array was constructed before the programs necessary to design the transition region of the baluns, ITC and IVSAC, were written. Therefore, the shape of the transition region of the baluns used in the array were only approximated. The baluns were constructed from the same RG 402 50-ohm semi-rigid coax used in the balun design of Section 6.3. The dielectric constant of the teflon loading this coax is $\varepsilon_r = 2.1$. The baluns used in the array were designed to have a low frequency cutoffs of 2.0 GHz and to give $|\rho/\rho_o| \leq 0.05$ where ρ and ρ_o are as defined in Section 6.2. For these parameters, it was assumed that the baluns would exhibit a Tchebycheff reflection coefficient response with frequency (not necessarily a good assumption), and the length of the baluns were calculated as follows: For $\frac{\rho}{\rho_o} = 0.05$, (6.2-5) leads to

$$\cosh(A) = 20 \quad \text{or} \quad A = 3.68835.$$

In Section 6.2, for a low frequency cutoff of 2.5 GHz, (6.2-8) leads to

$$l = 1.91 \textit{ inches.} \tag{7.1-3}$$

It is noted that due to their higher low frequency cut off, the baluns used for the array are shorter then the balun designed in Section 6.2, which has a low frequency cutoff of 2.0 GHz and is 2.4 inches long. A typical S_{11} reflection coefficient magnitude measurement for an array balun, connected to a spiral as designed in Section 4.1, is shown in Fig. 7.1-3. It may be noticed that the Tchebycheff response, which was recorded for the balun designed in Sec 6.2, is absent. The lack of a Tchebycheff response for the array balun demonstrates the importance of using ITC and IVSAC in the design process of the wideband balun.

7.2 Radiation Pattern Measurements

Radiation patterns were measured using the Virginia Tech far field antenna range. The antenna under test, operated as the receiving antenna, is rotated 360 degrees while the power level is recorded. The transmit antennas used are linearly polarized standard gain horns. For more information on the antenna range refer to [28].

Before performing pattern measurements on our antenna, it would be wise to perform measurements on a similar antenna for which we have some idea of what the radiation patterns should be. This allows us to evaluate the strengths and weaknesses of our facility. Thus, measurements were taken for a spiral antenna produced by

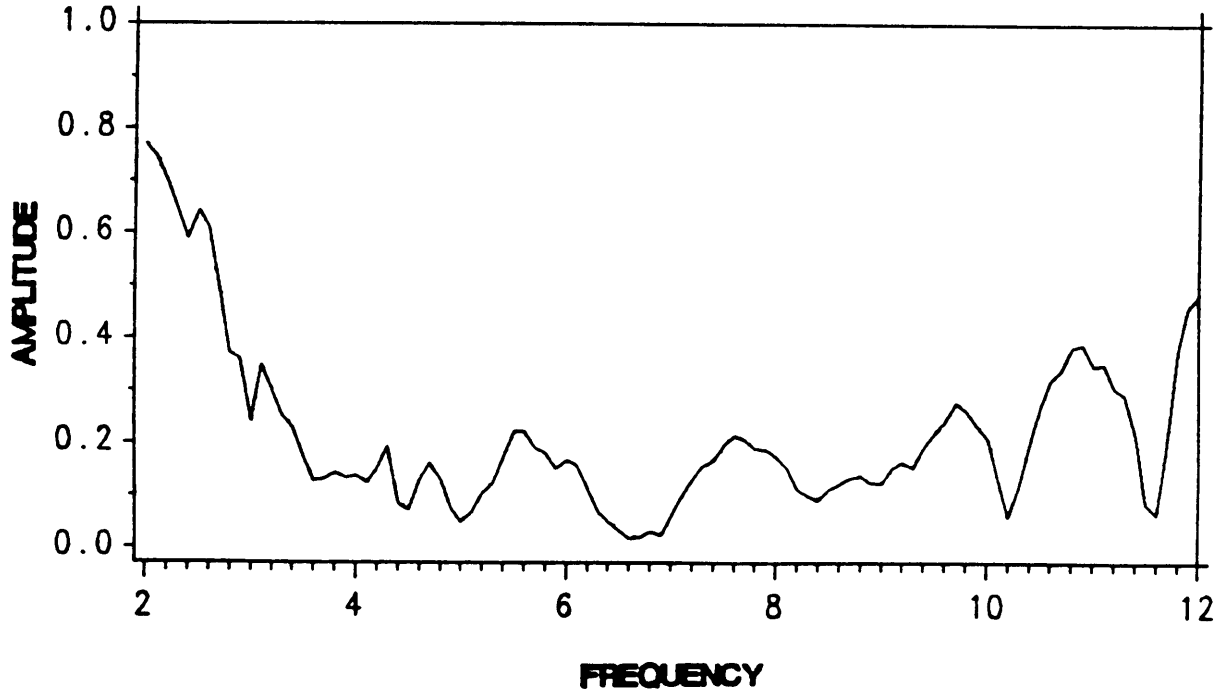

Figure 7.1-3. Reflection coefficient measured using a typical balun used in the wideband switched array.

American Electronics Laboratories Inc. (AEL) and are compared with the pattern measurements performed by AEL [29] on a similar antenna (nominal measurements). The antenna, model AST-1492A, is a broadband, cavity backed planar Archimedean spiral antenna that operates from 2.0 GHz to beyond 20.0 GHz. Radiation patterns were recorded at the frequencies 3.0, 6.0 and 10.0 GHz, thus covering the two octave region we are concerned with. Assuming the antenna is located in the xy-plane, the x-axis is defined as vertical polarization and the y-axis is defined as horizontal polarization. For each frequency, four antenna patterns were recorded: vertical and horizontal polarization for $\phi = 0.0°$ and vertical and horizontal polarization for $\phi = 90.0°$. The geometry used for the measurements, including the antennas orientation in the xy-plane, are shown in Fig. 7.2-1 and Fig 7.2-2. The recorded patterns are shown in Appendix C. Nominal results provided by AEL [29] are marked by asterisks. Agreement between our results and AEL's nominal results are very close, in most cases they differ by less than a decibel and in the extreme case they differ by only about 3 dB. Therefore, it appears that we can trust the results of our range to be accurate to at least 3 dB.

Having established the accuracy of our range, we proceed to perform pattern measurements on our spiral. The geometries used in making the measurements are identical to those used in making the AEL measurements and are shown in Fig. 7.2-1 and 7.2-2. Since we are only interested in the forward directed radiation, the spiral is backed by absorber. The face of the absorber measures 8 inches on each side, the depth is 5 inches. Radiation patterns were recorded at the frequencies 2.5, 4.0, 6.0, 8.0 and 10.0 GHz. The measured patterns are shown along with the corresponding predictions made using ESP in Figs. 7.2-3 through 7.2-7.

In every case ESP has predicted the fields accurately out to about $\theta = 45°$. In the region about $\theta = 90°$ the predictions made by ESP are the least accurate. In general, the

the two polarizations of the fields in this region appear to be more nearly identical then predicted by ESP. The best explanation for the discrepancy is scattering due to the presence of the absorber and feed structure as these features were not present in the model of the spiral used by ESP. It may also be noted that the accuracy of the ESP pattern calculations are not affected by frequency. As might be expected, the thin wire approximations made by ESP did not effect the field calculations as they did the impedance calculations. In any case, the measured patterns agreed well with the predictions made by ESP.

In Appendix D, the radiation patterns recorded for the spiral designed in Section 4.1 are presented along with radiation patterns recorded for the AEL spiral at the frequencies 2.5, 6.0 and 10 GHz. This allows us to compare the performance of the antenna designed in this paper to the performance of a commercial antenna. The patterns are very similar at all frequencies. The patterns are most dissimilar at 2.5 GHz. This can be explained by the fact that the AEL spiral is backed by an absorber loaded metalic cavity while the spiral designed in Section 4.2 is backed only by a piece of absorber. At the lower frequencies the absorber is less efficient and more radiation is able to be reflected off of the back of the AEL spirals cavity changing the radiated fields, this phenomena does not affect the spiral of Section 4.2 because there is no metalic cavity backing. To conclude, it can be said that the spiral of Section 4.2 compares favorably to the commercial AEL spiral in terms of radiation pattern.

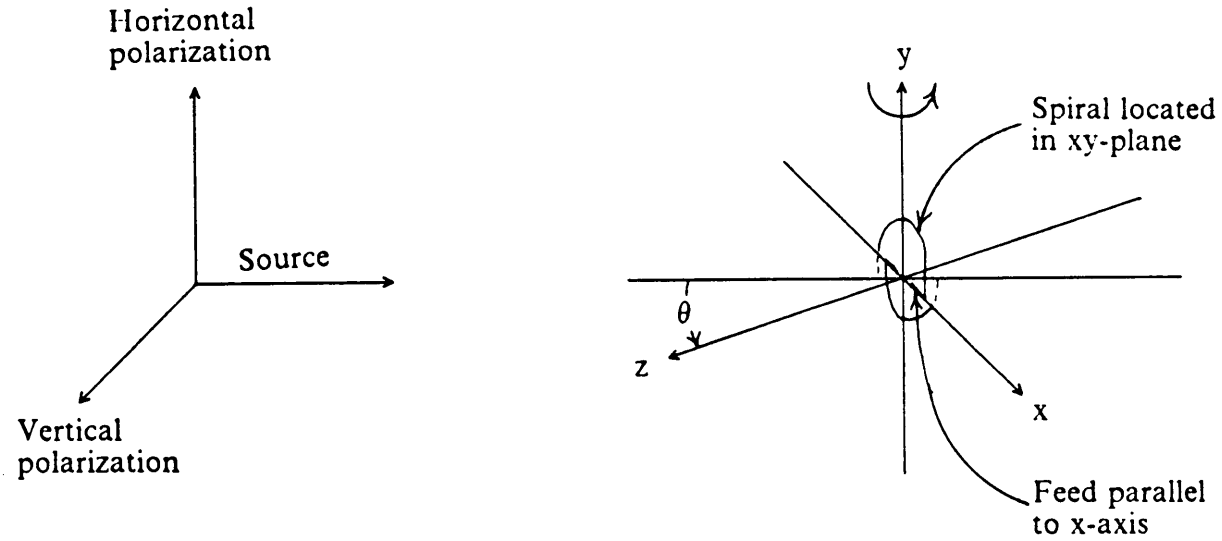

Figure 7.2-1. Range geometry used in $\phi = 0°$ plane pattern measurements of spiral antennas.

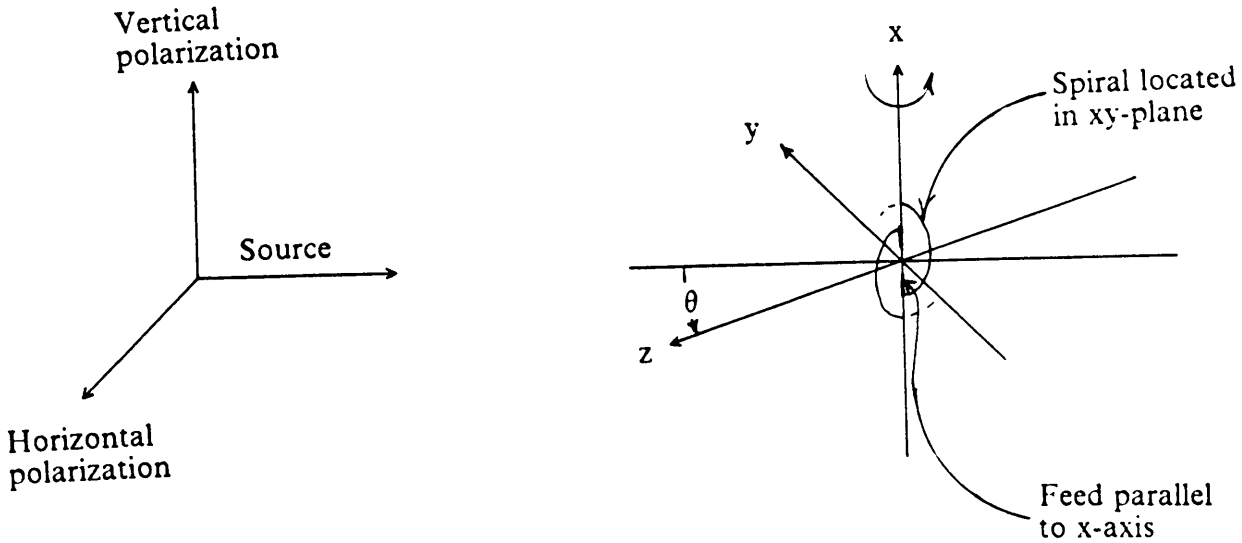

Figure 7.2-2. Range geometry used in $\phi = 90°$ plane pattern measurements of spiral antennas.

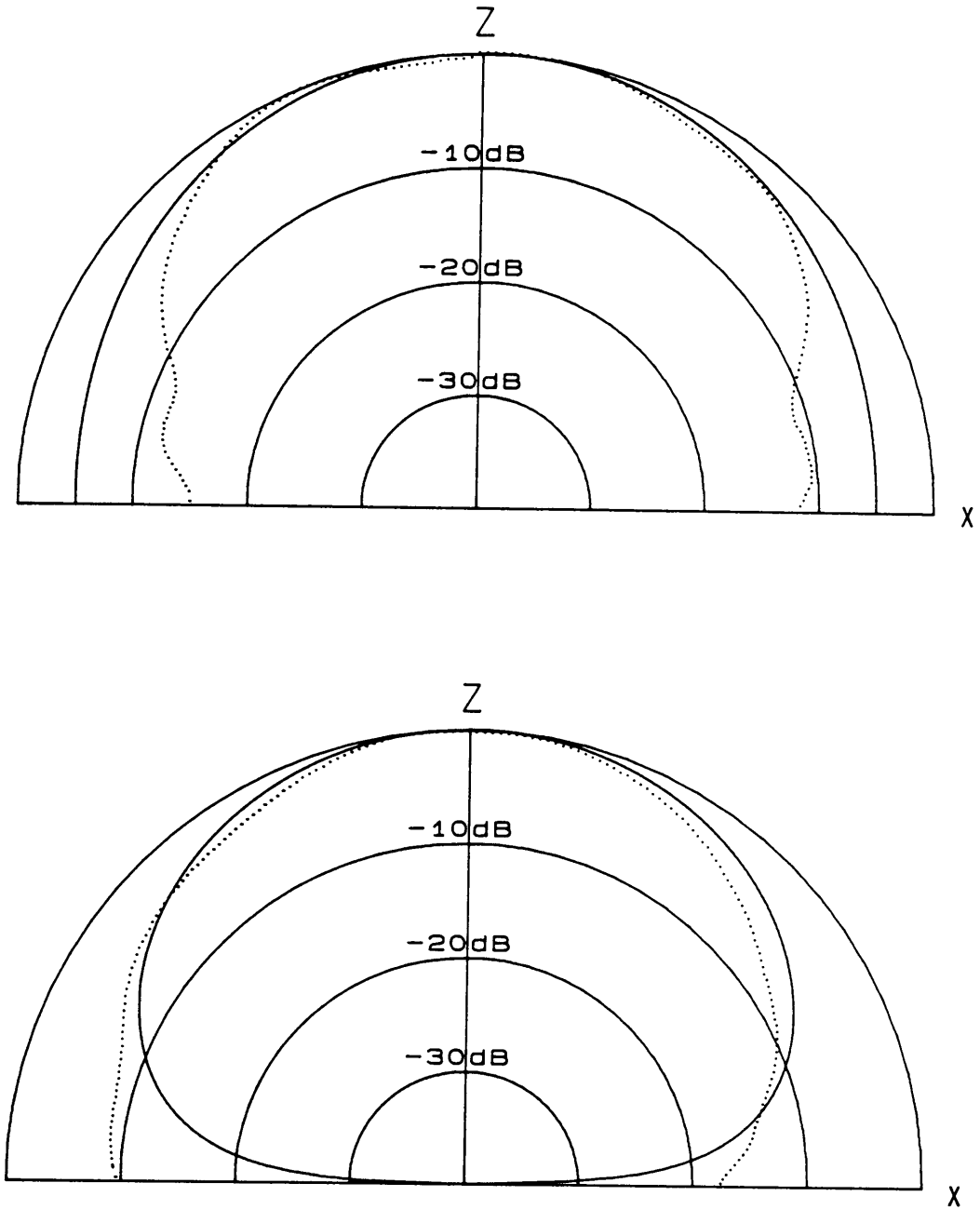

Figure 7.2-3. Radiation patterns of the Archimedean spiral of Section 4.1 at 2.5 GHz: top, $\phi = 0°$ plane pattern horizontal polarization, bottom, $\phi = 0°$ plane pattern vertical polarization. Measured-dashed; theoretical results obtained from ESP-solid.

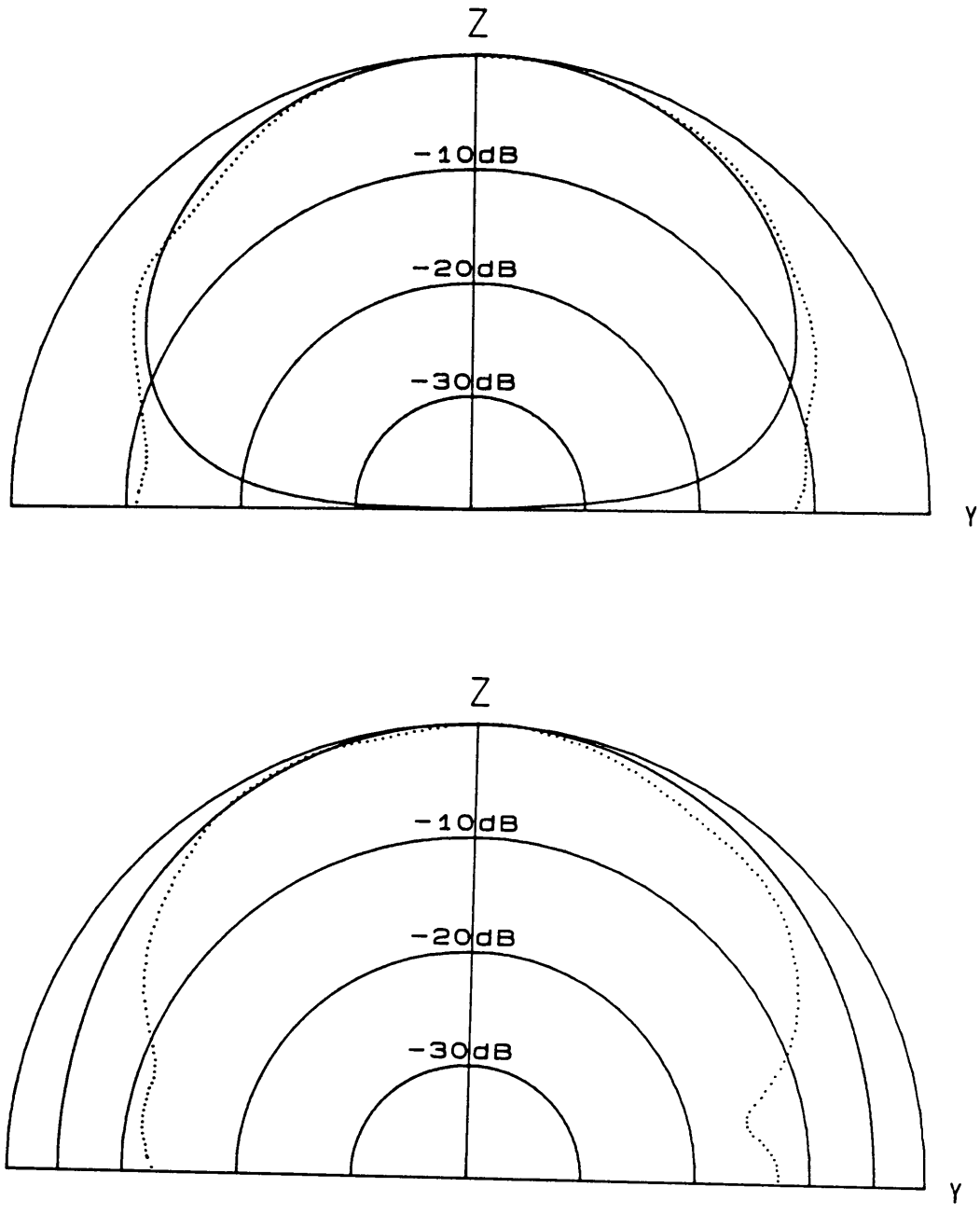

Figure 7.2-3 (continued) top, $\phi = 90°$ plane pattern horizontal polarization, bottom, $\phi = 90°$ plane pattern vertical polarization. Measured-dashed; theoretical results obtained from ESP-solid.

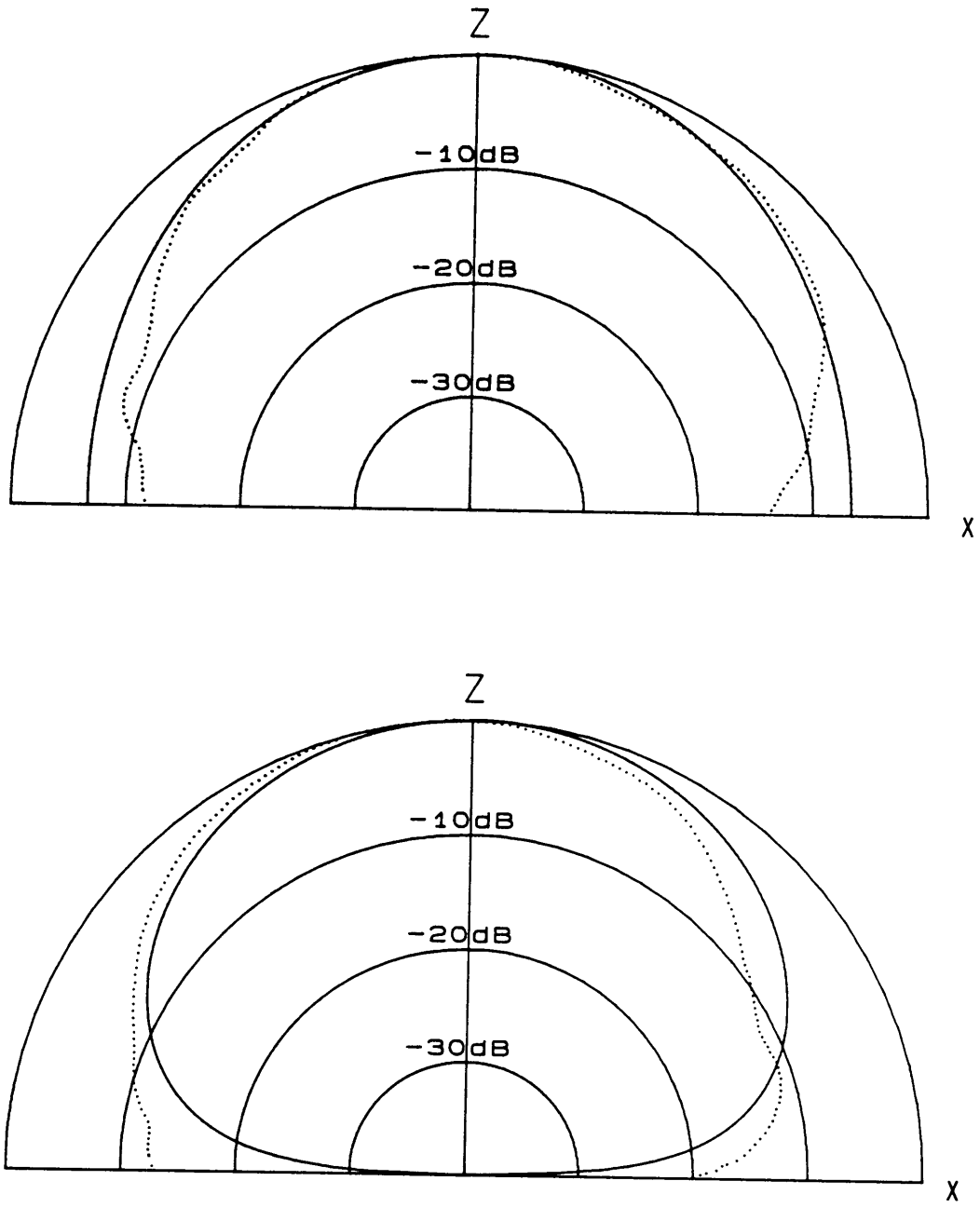

Figure 7.2-4. Radiation patterns of the Archimedean spiral of Section 4.1 at 4.0 GHz: top, $\phi = 0°$ plane pattern horizontal polarization, bottom, $\phi = 0°$ plane pattern vertical polarization. Measured-dashed; theoretical results obtained from ESP-solid.

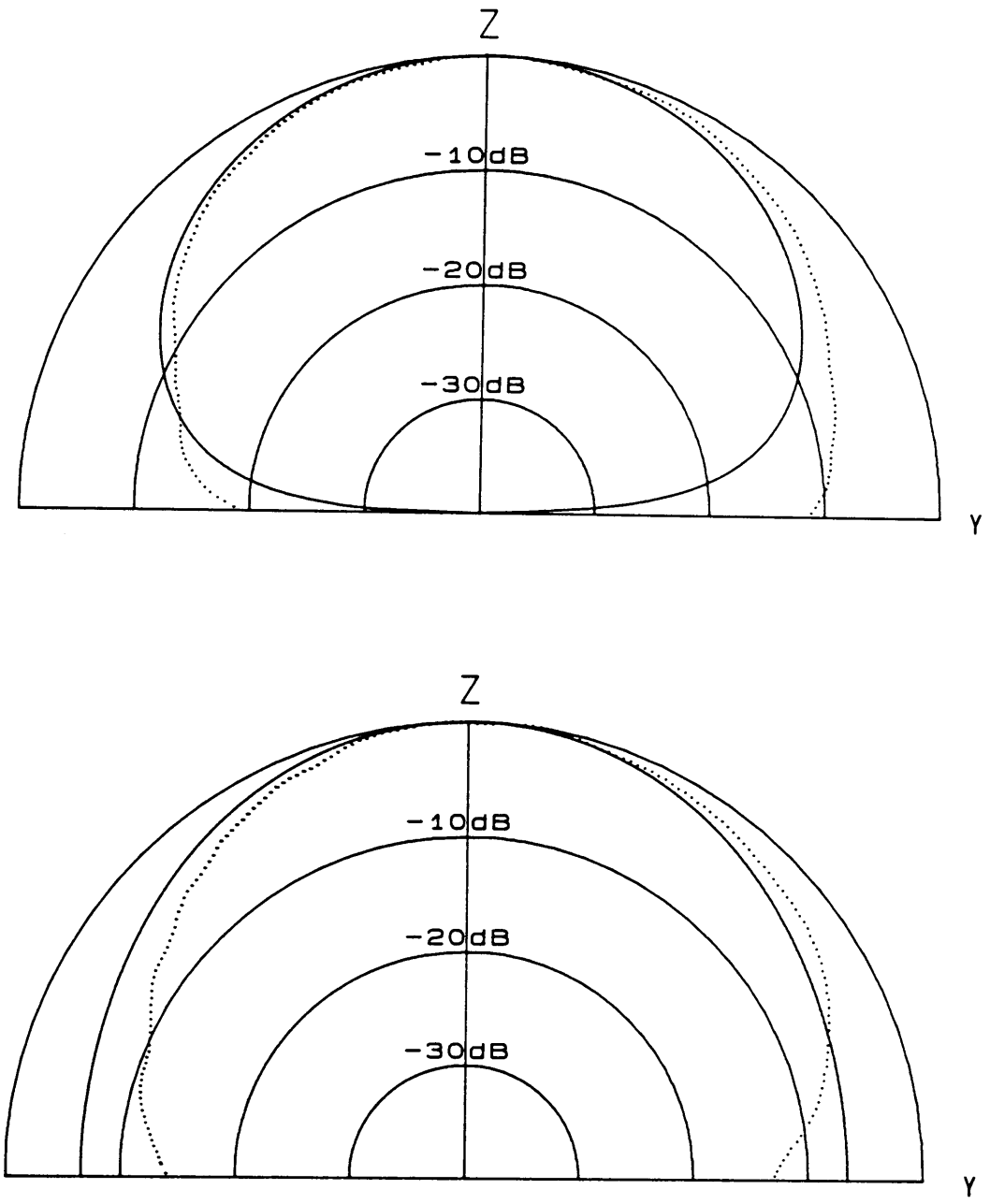

Figure 7.2-4 (continued) top, $\phi = 90°$ plane pattern horizontal polarization, bottom, $\phi = 90°$ plane pattern vertical polarization. Measured-dashed; theoretical results obtained from ESP-solid.

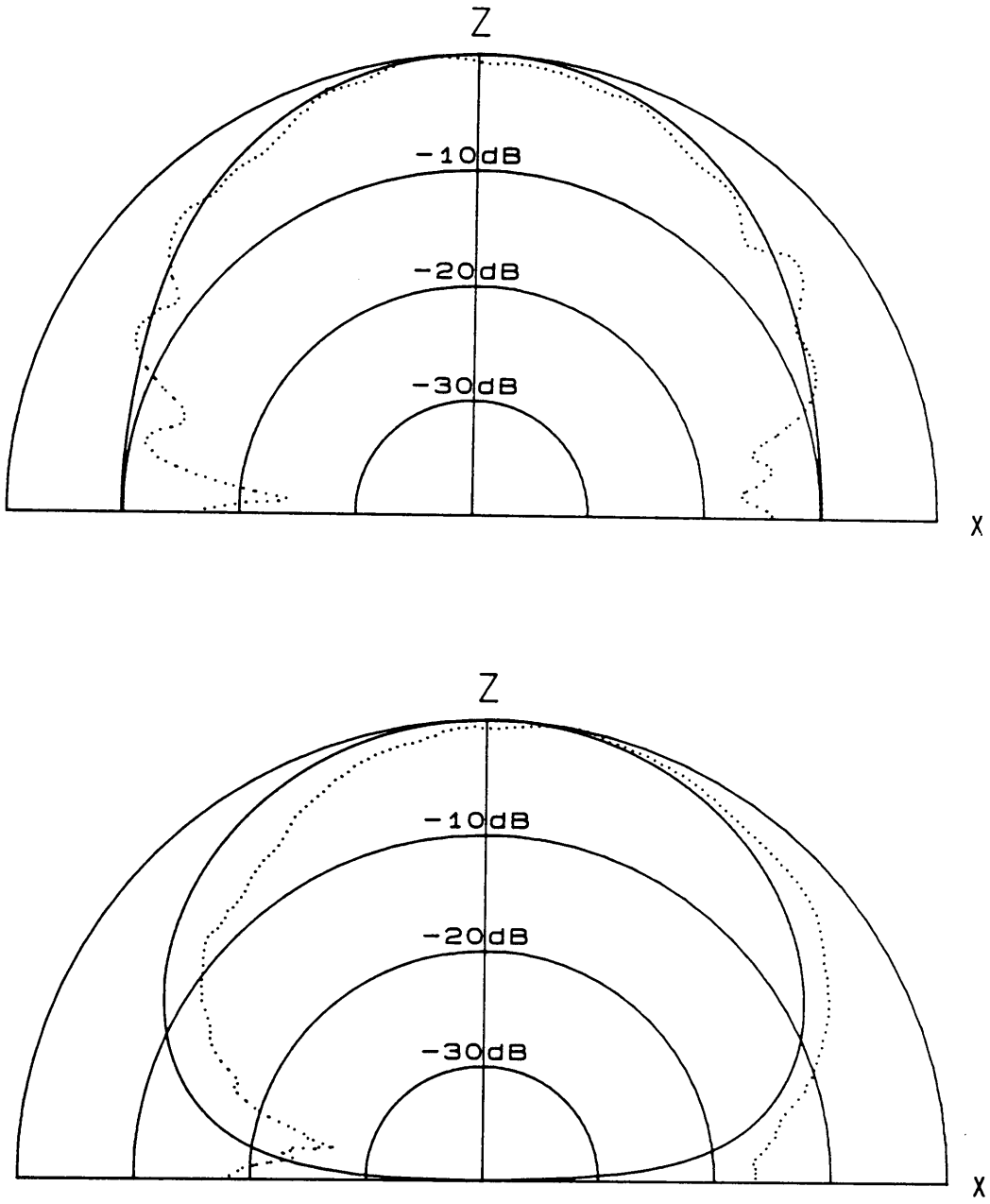

Figure 7.2-5. Radiation patterns of the Archimedean spiral of Section 4.1 at 6.0 GHz: top, $\phi = 0°$ plane pattern horizontal polarization, bottom, $\phi = 0°$ plane pattern vertical polarization. Measured-dashed; theoretical results obtained from ESP-solid.

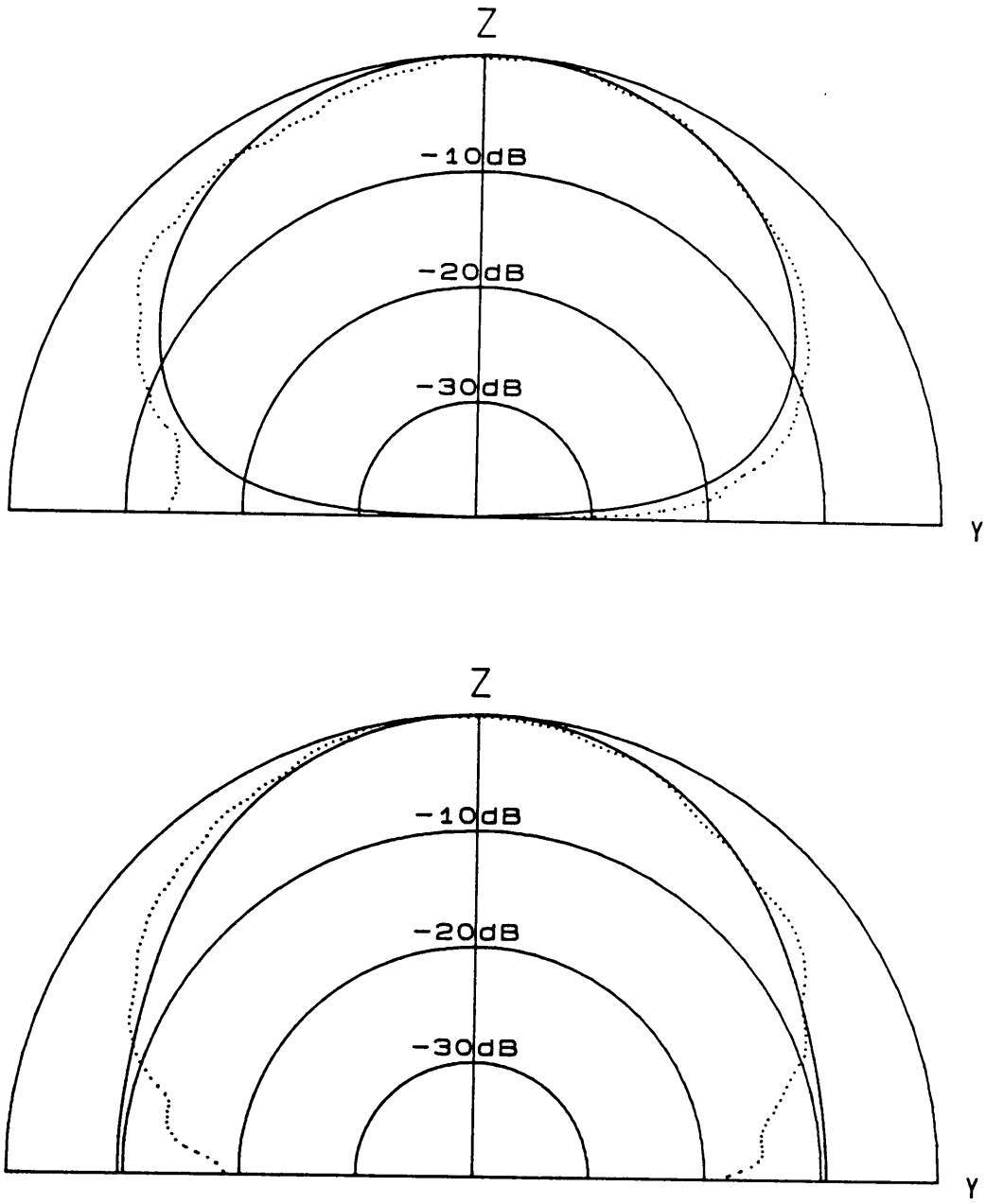

Figure 7.2-5 (continued) top, $\phi = 90°$ plane pattern horizontal polarization, bottom, $\phi = 90°$ plane pattern vertical polarization. Measured-dashed; theoretical results obtained from ESP-solid.

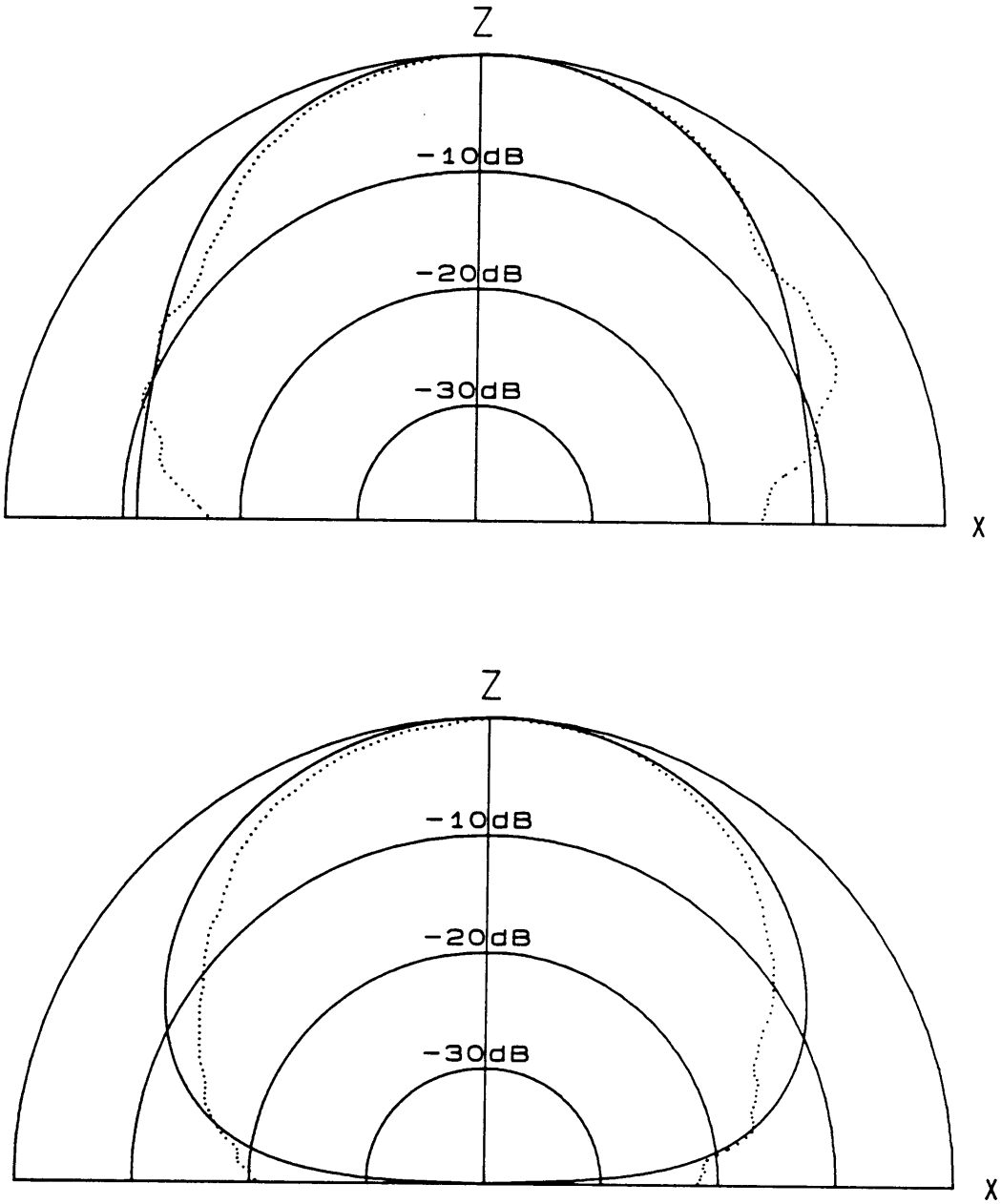

Figure 7.2-6. Radiation patterns of the Archimedean spiral of Section 4.1 at 8.0 GHz: top, $\phi = 0°$ plane pattern horizontal polarization, bottom, $\phi = 0°$ plane pattern vertical polarization. Measured-dashed; theoretical results obtained from ESP-solid.

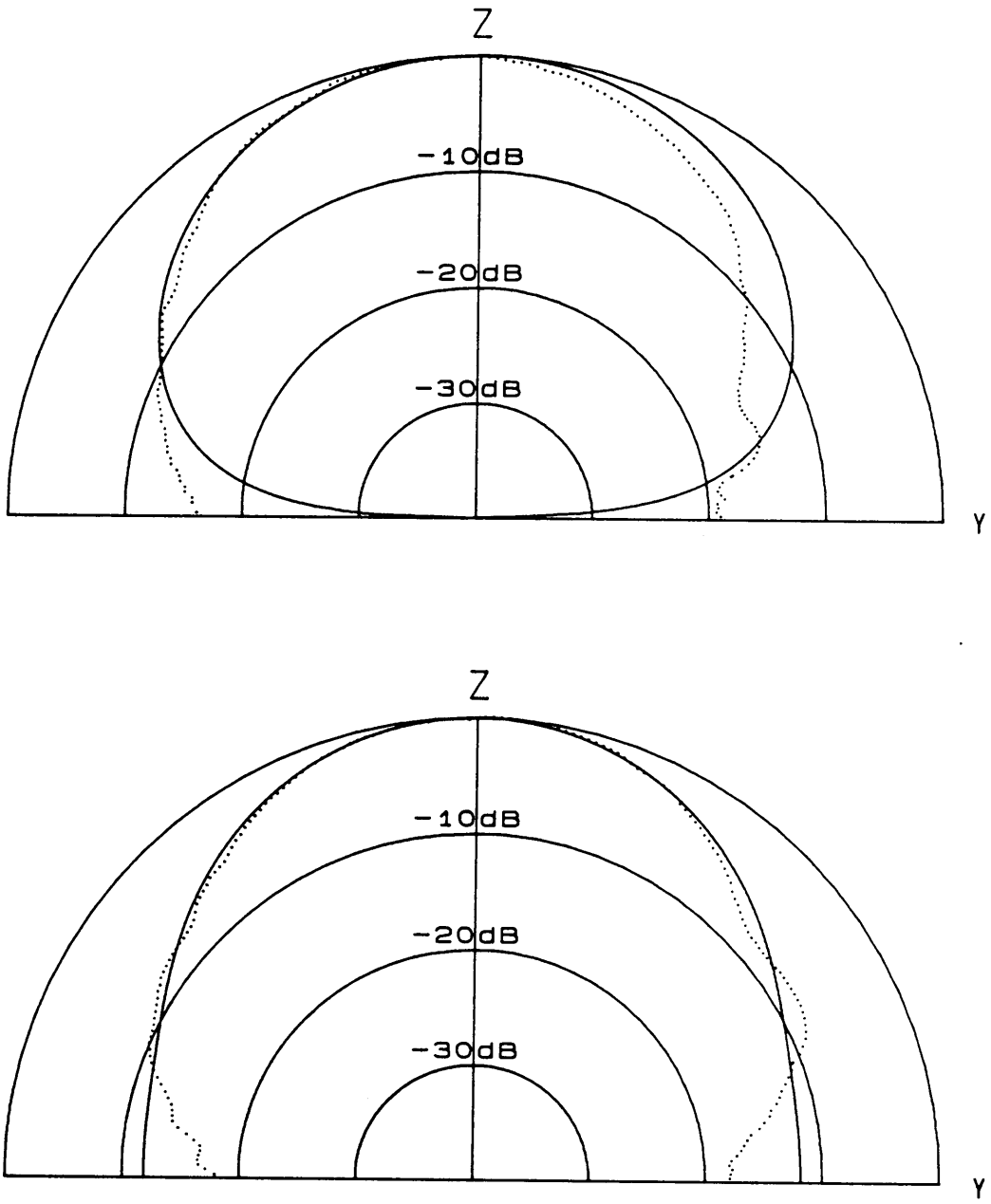

Figure 7.2-6 (continued) top, $\phi = 90°$ plane pattern horizontal polarization, bottom, $\phi = 90°$ plane pattern vertical polarization. Measured-dashed; theoretical results obtained from ESP-solid.

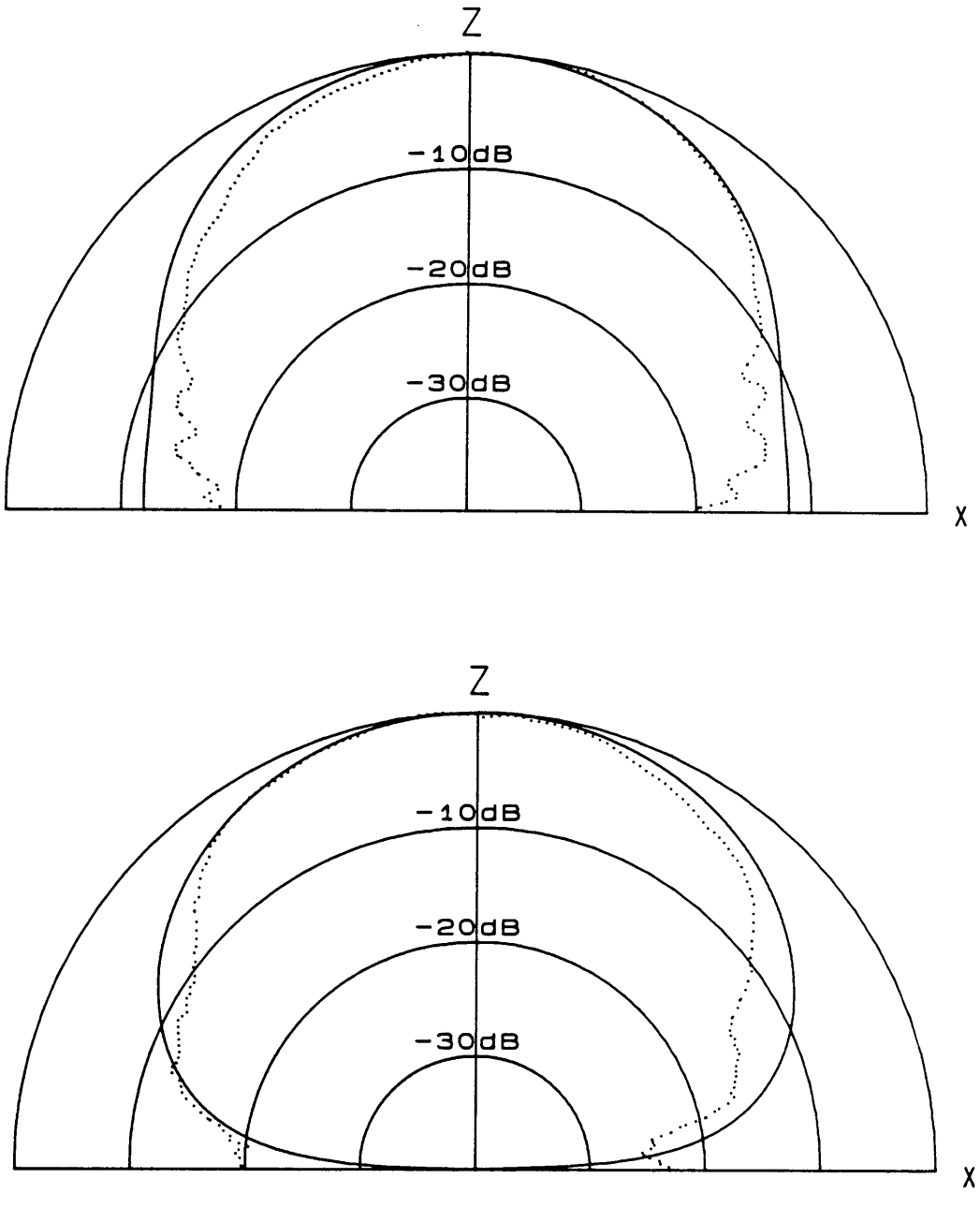

Figure 7.2-7. Radiation patterns of the Archimedean spiral of Section 4.1 at 10.0 GHz: top, $\phi = 0°$ plane pattern horizontal polarization, bottom, $\phi = 0°$ plane pattern vertical polarization. Measured-dashed; theoretical results obtained from ESP-solid.

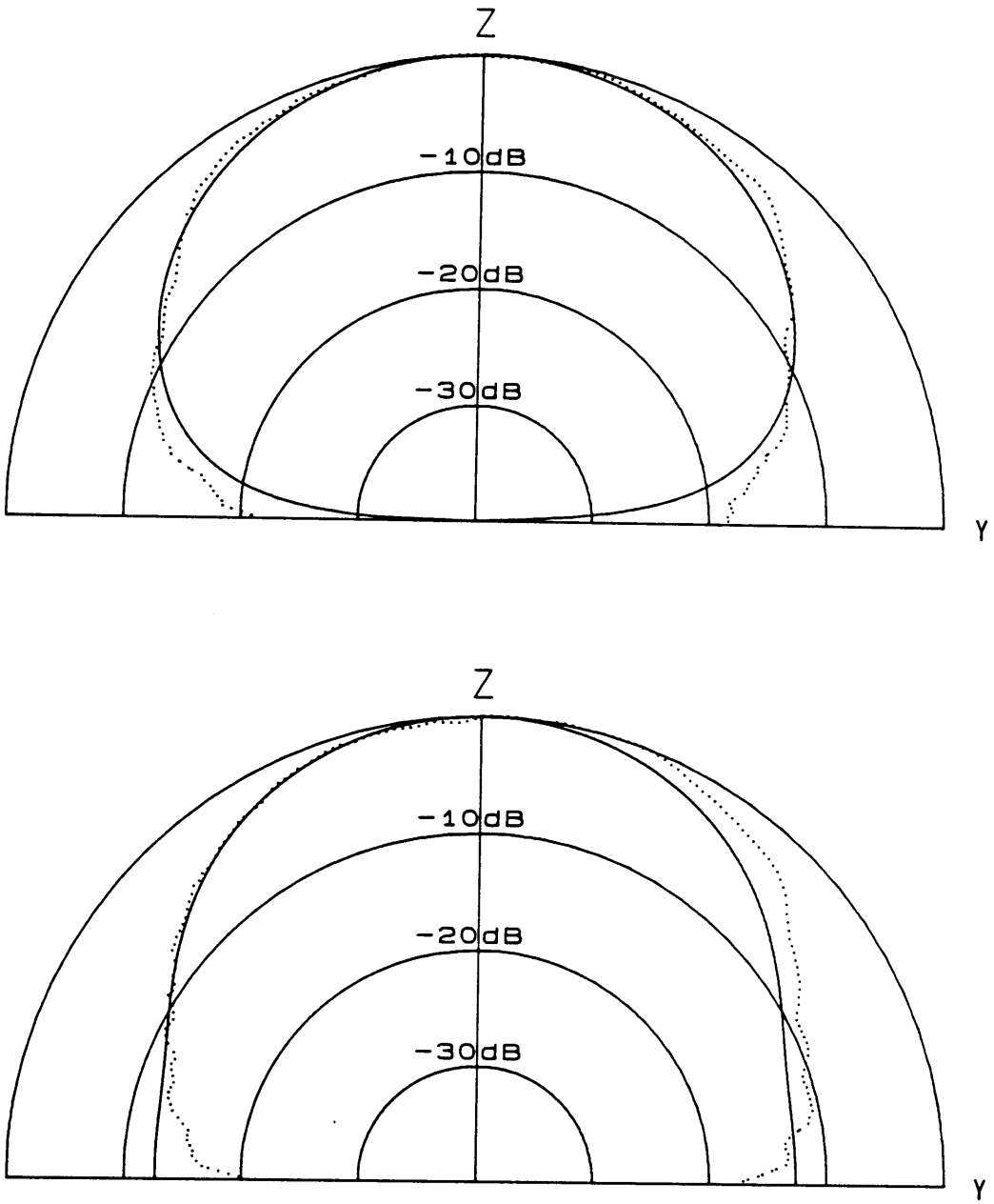

Figure 7.2-7 (continued) top, $\phi = 90°$ plane pattern horizontal polarization, bottom, $\phi = 90°$ plane pattern vertical polarization. Measured-dashed; theoretical results obtained from ESP-solid.

VIII. Conclusions and Recommendations

8.1 Conclusions

The primary goal of this research project was to design and construct elements for use in the wideband switched [1]. It was found that Archimedean spiral antennas are appropriate elements. A second goal was to employ modern numerical methods in the design of the spiral antenna. The Electromagnetic Surface Patch Code (ESP) [17] was used to aid in the design and analysis of the antenna. Specific conclusions follow.

1. *Spiral Design*

The design of an Archimedean spiral antenna capable of operation over the two octave bandwidth between 2.5 GHz and 10 GHz was presented in Chapter 4. The structure of the Archimedean spiral is shown in Fig. 4.1-1. The spiral was chosen to be self-complimentary; therefore, the space between the arms of the spiral, s, is equal to the widths of the arms,w. We chose the dimensions

$$s = w = 0.03 inch. \tag{8.1-1}$$

In section 4.1 it was shown that for these values of s and w the spiral requires $N = 8$ turns to achieve operation over the two octave bandwidth. In order to simplify attachment of the feed network, the design of Section 4.1 includes two feed attachment plates at the center of the spiral. Each feed attachment plate has a radius of $R_f = 0.045$ inch.

The method by which the Archimedean spiral of Section 4.1 was constructed is discussed in Chapter 5.

2. *Prediction of Spiral Performance With ESP*

Originaly we had intended to model the Archimedean spiral of Section 4.1 with infinitely thin infinitely conducting plates. However, as will be discussed in Section 8.2, this was not possible and we were forced to model the spiral using electrically thin wires.

For numerical evaluation an approximation to the Archimedean spiral consisting of 722 straight wire segments was used. The approximate spiral is shown in Fig. 4.4-1. All of the wires used in the approximation have a radius of $a = 0.015$ inch and are spaced 0.03 inch apart providing a self-complimentary structure. It is noted in Section 4.3 that ESP uses a thin wire approximation which may lead to inaccurate results for wire radii exceeding $a = .01\lambda$ [17]. For the wires with radii $a = 0.015$ inch, the electrical radii change from $a = 0.0032\lambda$ to $a = 0.0127\lambda$ over the two octaves between 2.5 GHz and 10 GHz. At 7.87 GHz $a = 0.01\lambda$; therefore, we have cause to view results obtained from ESP at frequencies greater then 7.87 GHz with suspicion.

Numerical results obtained from ESP over the two octave region between 2.5 GHz and 10 GHz are shown in Table 4.4-1. A plot of input impedance magnitude versus frequency is shown in Fig. 4.4-2. It is noted that at 4 GHz the input impedance begins

to increase sharply. This is most likely due to the thin wire approximations made by ESP. As we know that results obtained by ESP at frequencies above 7.87 GHz are likely to be erroneous due to the thin wire approximations made by ESP, we cautiously ignored impedance results obtained for frequencies greater than 7.0 GHz Field pattern predictions made by ESP are presented in Figs. 7.2-3 through 7.2-7. The thin wire approximations do not seem to affect the pattern calculations.

3. *Balun Design*

The choice was made to use 50-ohm coaxial cable in the feed network of the spiral because it is readily available, inexpensive and compatible with the existing equipment at our antenna range. This choice presented us with two problems. The first problem was the impedance mismatch between the input to the spiral and the 50-ohm coax. The second problem was assuring that the spiral is feed in a balanced manner. Both of these problems are thoroughly discussed in Section 4.0.

The two problems which result from feeding the Archimedean spiral with 50-ohm coax were resolved by using a wideband balun transformer [12]. A diagram of the wideband balun transformer used is shown in Fig. 6.1-1. A discussion of the basic principles behind the balun transformer is presented in Section 6.1. Design equations and the design procedure used for the balun transformer are discussed in Section 6.2. To aid in the design procedure, two computer programs have been written in FORTRAN. The first program, referred to as the Impedance Taper Code (ITC), is presented in Appendix A. The second program, referred to as The Impedance Versus Subtended Angle Code (IVSAC), is presented in Appendix B. In Section 6.2 both codes are discussed and a stepwise design procedure for the wideband balun transformer which uses ITC and IVSAC is presented. An example of how ITC and IVSAC are used in the design of a wideband balun transformer is presented in Section 6.3.

For the purposes of our present discussion, it is sufficient to state that the wideband balun transformer used provides a matching section between coaxial cable of characteristic impedance Z_1 and a balanced two conductor transmission line of characteristic impedance Z_2 so that the reflection coefficient, as measured from the coaxial side, possess a Tchebycheff response with frequency. Typical Tchebycheff responses are shown in Fig. 6.2-2.

In section 6.3 the design of a wideband balun transformer used to match a 50-ohm coaxial cable to a 125-ohm two conductor line is presented. The wideband balun transformer is designed to have a low frequency cutoff, as defined by (6.2-8), of 2.0 GHz and a maximum reflection coefficient in the passband of $\rho = 0.023$. The method by which the balun was constructed is also discussed in Section 6.3.

4. *Wideband Balun Transformer Performance*

The method by which the wideband balun transformer of Section 6.3 was attached to the Archimedean spiral of Section 4.1 is discussed in Section 7.0, and S_{11} reflection coefficient measurements for the spiral antenna fitted with the balun transformer and fed by 50-ohm coax is are presented are presented in Section 7.1. Measurements were made over the frequency range between 500 MHz and 12 GHz using a Hewlett-Packard 8410 network analyzer. The results of the measurements are shown in Figs. 7.1-1 and 7.1-2.

Comparison of Fig. 7.1-1 to Fig. 6.2-2 verifies that the reflection coefficient amplitude, when plotted versus frequency, possessess the desired Tchebycheff response. The balun transformer of Section 6.3 was designed to have a low frequency cutoff of 2.0 GHz. As discussed in Section 7.1, the low frequency cutoff is graphically found from Fig. 7.1-1 to be approximatly 1.8 GHz. Over the two octaves between 2.5 GHz and 10 GHz, the reflection coefficient magnitude peaks remain fairly constant, falling within the range of 0.05 to 0.15 with a gradual increase with frequency being observed. While the

magnitude of the peaks are higher then the design goal of 0.023 they are reasonable small for our purposes. An explanation for the difference is that the balan transformer was designed to match a 50-ohm coaxial cable to a 125-ohm two wire transmission line. This is the case for which the 0.023 peak was calculated. As noted in Section 6.3, a larger impedance transformation was not chosen as it would require an excessivly large slot width at the end of the transition region for the coax that we are using. Predictions of the spiral's input impedance obtained from ESP, ignoring results obtained at frequencies greater then 7.0 GHz, indicate that we can expect the impedance magnitude to be somewhere in the range between 118.8 and 205.9 ohms. For this range of input impedances, a reflection coefficient in the range of 0.025 to 0.24 can be expected to be measured at the junction between the 125-ohm two conductor output of the balun and the input to the spiral. Therefore, the larger measured reflection coefficient peaks are probably due to the impedance mismatch between the output of the balun transformer and the input to the spiral. It should also be noted that while a gradual increase in reflection coefficient magnitude peaks with frequency is observed in Fig. 7.1-1, there is no evidence that the input impedance of the spiral of Section 4.1 increases drastically with frequency at frequencies greater than 4 GHz as predicted by ESP. It is suspected that the thin wire approximations made by ESP caused this erroneous result.

To conclude, in terms of both impedance transformation and low frequency cutoff, the wideband balun transformer performed satisfactorily close to the design objectives outlined in Section 6.3, also, the impedance predictions obtained from ESP where found to be useful in the design of the balun transformer as an idea of the spirals input impedance was required.

5. *Spiral Antenna Results*

Radiation patterns were measured for the Archimedean spiral of Section 4.1 at the Virginia Tech far field antenna range [27]. Because we are only interested in the forward directed radiation, and want to prevent scattering from the balun and feed network while making the measurements, the spiral was backed by a piece of absorber. The absorber measures 8 inches on each side and is 5 inches deep. The geometries used in making the measurements is shown in Figs. 7.2-1 and 7.2-2. Pattern recorded at the frequencies 2.5, 4.0, 6.0, 8.0 and 10.0 GHz are shown in Figs. 7.2-3 through 7.2-7.

In every case ESP has predicted the fields accurately out to about $\theta = 45°$. In the region about $\theta = 90°$ the predictions made by ESP are the least accurate. The difference in the patterns in this region are most likly caused by the absorber backing.

In order to assess the performance of the spiral of Section 4.1 with respect to a commercial spiral, patterns were recorded for a wideband spiral antenna produced by the American Electronics Laboratories Inc. (AEL). The AEL antenna, model AST-1492A, is a broadband, absorber loaded cavity backed, planar Archimedean spiral antenna, which is designed to operate over the frequency range between 2.0 GHz and 20 GHz [19].

In Appendix D, radiation patterns recorded for the spiral of Section 4.1 are shown along with patterns recorded for the AEL spiral at the frequencies 2.5, 6.0 and 10.0 GHz. The patterns recorded for the two spiral are very similar at all frequencies. The patterns are the most dissimilar at 2.5 GHz. This is explain by the fact that the AEL spiral is backed by an absorber loaded metalic cavity while the spiral of Section 4.1 is only backed by absorber. At the lower frequencies the absorber is less efficient and more radiation is able to reflect off of the back of the AEL spiral cavity and affect the pattern. This phenomena does not affect the spiral of Section 4.1 because there is no metallic cavity backing for this spiral.

To conclude, ESP has done an adequate job of predicting the field pattern of the spiral of Section 4.1 throughout the two octaves between 2.5 and 10.0 GHz. It is also noted that the spiral of Section 4.1 compares favorably to the commercial AEL spiral in terms of radiation pattern.

8.2 Recommendations for Future Work

1. *Improvements to ESP*

Our original intention was to model the spiral of Section 4.1 using infinitly thin infinitly conducting plates. However, as discussed in Section 4.3, ESP only allows structures to be feed by delta gap generators which may only be placed between segments of electrically thin wires or at junctions between the wires and plates. In any case, to insure continuity of current at the wire to plate junctions, attachment modes must be specified. attachment modes require that a disk of radius between 0.01λ and 0.25λ be specified on the surface of the plate to which the wire is to be attached, no closer then 0.1λ from any edge of the plate. Because the feed attachment plates have radii of $R_f = 0.045$ inch which is only 0.021λ at the highest frequency of 10 GHz (where they appear the largest electrically throughout the two octaves) the excessive size requirements of the feed attachment plates prevented us from modeling the spiral with plates. Because there is no size limitations on the plates themselves, possibilities for future work include an investigation into the possibility of either shrinking the size requirements on the wire to plate attachment modes or feeding the plates directly thus eliminating the need for attachment modes altogether.

Another possible improvement to ESP would be to modify it so that the dielectric on which the spiral is printed and the absorber loaded cavity backing the spiral could be included in the theoretical model.

2. *Smaller Antennas*

In Section 3.2, the Archimedean spiral was found to be an appropriate element for use in the two octave wideband switched array of Section 3.1, element size was not a problem. However, if spiral elements could be made electrically smaller without sacrificing bandwidth, a switched array architecture could be made possible which uses closer element spacings to achieve a greater bandwidth for the same given area.

Methods of increasing the bandwidth of spiral antennas were discussed in Section 2.4. These methods can also be used to reduce the size requirement of a spiral of a given bandwidth. The simplest method of reducing size is using a square spiral as shown in Fig. 2.4-1. More size reduction can be obtained by using a slow-wave spiral whose arms have been modulated, such as the spiral shown in Fig. 2.0-1. Two future areas of study can be identified. First, spiral geometries which offer size reduction can be examined in terms of the trade off between size reduction and performance (ESP could be helpful in this examination if it could be modified as stated earlier). Second, a study of wideband switched array geometries which make use of the smaller spirals could be pursued.

3. *Impedance Matching*

As stated in Section 2.2, for a planar spiral with a self-complimentary structure a high input impedance can be expected (in the range of 188.5 ohms as predicted by Babinet's principle). This often causes impedance matching problems as the spiral is usally fed from a 50 ohm coaxial line. It has been noted that the impedance matching problem might be greatly simplified if the impedance of the spiral were reduced by

making the ratio of conductor width to conductor spacing in the spiral greater then unity [16]. This is an area which deserves investigation.

Appendix A: ITC Fortran Listing

The following program uses (6.2-9) and (6.2-12) to calculate the impedance taper needed to match an impedance Z_1 to an impedance Z_2 for specified values of $|\rho_{max}|$ and ρ_o. An example of the use of ITC is presented in Section 6.3.

```
CCCCCCCCCCCCCCCCCCCCCCCCCCCCCCCCCCCCCCCCCCCCCCCCCCCCCCCCCCCCCCCCCCCCCCCCCC
C                                                                           C
C                          ITC FORTRAN                                      C
C                                                                           C
C                   WRITTEN BY PAUL C. WERNTZ                               C
C                                                                           C
CCCCCCCCCCCCCCCCCCCCCCCCCCCCCCCCCCCCCCCCCCCCCCCCCCCCCCCCCCCCCCCCCCCCCCCCCC

CCCCCCCCCCCCCCCCCCCCCCCCCCCCCCCCCCCCCCCCCCCCCCCCCCCCCCCCCCCCCCCCCCCCCCCCCC
C                                                                           C
C   THIS PROGRAM IS USED TO CALCULATE THE REQUIRED IMPEDANCE TAPER          C
C                                                                           C
C   NEEDED TO MATCH TWO TRANSMISSION LINES WITH DIFFERENT                   C
C                                                                           C
C   CHARACTERISTIC IMPEDANCES SO THAT THE REFLECTION COEFFICIENT            C
C                                                                           C
C   POSSESSES A TCHEBYCHEFF FREQUENCY RESPONSE.   THE PROGRAM MAKES         C
C                                                                           C
C   USE OF THE IMSL ROUTINE 'DCADRE' WHICH EVALUATES THE INTEGRAL OF        C
C                                                                           C
C   F(X) FROM X=A TO X=B                                                    C
C                                                                           C
CCCCCCCCCCCCCCCCCCCCCCCCCCCCCCCCCCCCCCCCCCCCCCCCCCCCCCCCCCCCCCCCCCCCCCCCCC
      EXTERNAL F
      DOUBLE PRECISION LZO,A,XOL,B,C,RERR,AERR,ZO,PO,Z1,Z2,AY,T,Y,P
      RERR=0.DO
      AERR=1.0D-5
      A=0.DO
C
C   BELOW, ENTER THE CHARACTERISTIC IMPEDANCES OF THE TWO TRANSMISSION
C
C   LINES TO BE MATCHED, Z1 AND Z2.
C
      Z1=
      Z2=
C
C   ENTER BELOW:
C
C        1. PO - THE REFLECTION COEFFICIENT WITHOUT THE MATCHING
C           SECTION.
C
C        2. P - THE DESIRED REFLECTION COEFFICIENT WITH THE MATCHING
C           SECTION.
C
      PO=
      P=
C
      P=PO/P
      AY=DLOG(P + DSQRT(P * * 2 -1))
      XOL=-.51DO
 10   XOL=XOL+.01DO
      B=2.DO*XOL
      C=DCADRE(F,A,B,AERR,RERR,ERROR,IER)
      LZO=0.5DO*DLOG(Z1*Z2)+(PO/COSH(AY))*((AY**2)*C + 1)
      ZO=DEXP(LZO)
      WRITE(08,*)ZO
      IF(XOL.LE.0.5DO)GO TO 10
      STOP
```

```
      END

      REAL FUNCTION F(X)
      DOUBLE PRECISION P,PO,AY,Y,T
C
C     BELOW, INPUT THE VALUES OF P AND PO.
C
      P=
      PO=
C
      P=PO/P
      AY=DLOG(P + DSQRT(P * P-1))
      Y=AY*DSQRT(1.D0-X*X)
      T=DABS(Y/3.75D0)
      F=(0.5D0
     /+0.87890594D0*T**2
     /+0.51498869D0*T**4
     /+0.15084934D0*T**6
     /+0.02658733D0*T**8
     /+0.00301532D0*T*10
     /+0.00032411D0*T**12)
      RETURN
      END
```

Appendix B: IVSAC Fortran Listing

The following program uses equations (6.2-14) through (6.2-18) to calculate the upper bound, lower bound and average value of the impedance of a sloted coaxial line versus the subtended angle 2α. An example of the use of IVSAC is presented in Section 4.3.

```
CCCCCCCCCCCCCCCCCCCCCCCCCCCCCCCCCCCCCCCCCCCCCCCCCCCCCCCCCCCCCCCCCCCCCCCCCCC
C                                                                             C
C                        IVSAC FORTRAN                                        C
C                                                                             C
C                    WRITTEN BY PAUL C. WERNTZ                                C
C                                                                             C
CCCCCCCCCCCCCCCCCCCCCCCCCCCCCCCCCCCCCCCCCCCCCCCCCCCCCCCCCCCCCCCCCCCCCCCCCCCC

CCCCCCCCCCCCCCCCCCCCCCCCCCCCCCCCCCCCCCCCCCCCCCCCCCCCCCCCCCCCCCCCCCCCCCCCCCC
C                                                                             C
C     THIS PROGRAM CALCULATES THE UPPER AND LOWER BOUND OF THE                C
C                                                                             C
C     CHARACTERISTIC IMPEDANCE OF A SLOTED COAXIAL TRANSMISSION LINE          C
C                                                                             C
C     AS THE ANGLE SUBTENDED BY THE SLOT IS VARIED FROM 1.0 TO 355            C
C                                                                             C
C     DEGREES IN 1 DEGREE INCREMENTS.   THE USER IS PROMPTED TO INPUT:        C
C                                                                             C
C            1. ER - THE RELATIVE DIELECTRIC CONSTANT OF THE MATERIAL         C
C                                                                             C
C               BETWEEN THE CONDUCTORS.                                       C
C                                                                             C
C            2. ZO - THE CHARACTERISTIC IMPEDANCE OF THE COAX WITH NO         C
C                                                                             C
C               SLOT.                                                         C
C                                                                             C
CCCCCCCCCCCCCCCCCCCCCCCCCCCCCCCCCCCCCCCCCCCCCCCCCCCCCCCCCCCCCCCCCCCCCCCCCCCC
      REAL MU,N,K,LBA,ZO
      WRITE(*,05)
 05   FORMAT(/,'ENTER ER,ZO')
      READ(*,*)ER,ZO
      PI=ACOS(-1.0)
      MU=4*PI*1.0E-7
      EP=ER*8.854E-12
      LBA=ZO*2*PI*SQRT(EP)/SQRT(MU)
      DO 40 J=1,355
         DEG=J
         DEG=DEG*PI/360
C
C  THIS SECTION EVALUATES THE LOWER BOUND.
C
         FTOT=0.0
 12      FORMAT(/,'ZO=',F8.5)
         DO 10 I=1,100
            N=I*1.0
            FAC=COSH(N*LBA)/SINH(N*LBA)
            F1=(1.0+FAC)/(N*DEG)
            AN=(N*DEG)**3-(N*DEG)*6.0
            BN=((N*DEG)**2)*3.0-6.0
            F2=(AN*COS(N*DEG)-BN*SIN(N*DEG))/((N*DEG)**4)
            F2=F2**2
            FTOT=FTOT+(F1*F2)
 10      CONTINUE
         CINV=(4.0*DEG)/(5.0*PI)+LBA*(40.0/PI)*FTOT
         C1=1/CINV
         TOP=(1.0/(2*PI))*SQRT(MU/EP)*LBA
         BOT=1-(4.0/5.0)*(DEG/PI)*C1
```

```
         FANS=TOP/BOT
C
C     THIS SECTION EVALUATES THE UPPER BOUND.
C
         K=PI/(PI-DEG)
         TOP=0.0
         BOT=0.0
         DO 20 I=1,100
            N=I*1.0
            VAL=(N**2-K**2)
            VALL=(COSH(N*LBA))/(SINH(N*LBA))
            TOP=TOP+(SIN(N*DEG)**2)/(N*VAL*(1+VALL))
            BOT=BOT+(N*(SIN(N*DEG))**2)/((VAL**2)*(1+VALL))
20       CONTINUE
         C1=TOP/BOT
         TOT=0.0
         C1=-C1
         DO 30 I=1,100
            N=1.0*I
            VALL=(COSH(N*LBA))/(SINH(N*LBA))
            TOP=(SIN(N*DEG)**2)*(1.0+(C1*N**2)/(N**2-K**2))**2
            BOT=(N**3)*(1+VALL)
            TOT=TOT+TOP/BOT
30       CONTINUE
         X=SQRT(MU/EP)
         HANS=(X/(2*PI))*LBA+(X/(PI*(PI-DEG)**2))*TOT
         WRITE(08,*)J,FANS
         WRITE(09,*)J,HANS
         WRITE(10,*)J,(FANS+HANS)/2.0
40    CONTINUE
      STOP
      END
```

Appendix C: Comparison of VT Patterns and Nominal AEL Patterns

In this appendix radiation patterns recorded at the Virginia Tech far field antenna range [27] for an AEL model AST-1492A absorber loaded cavity backed Archimedean spiral antenna, are presented along with nominal pattern data measured by AEL [29] for a similar antenna. The geometries used in making the patterns are shown in Figs. 7.2-1 to 7.2-2. The patterns are shown in Figs. C-1 to C-3. A discussion of the patterns is presented in Section 7.2.

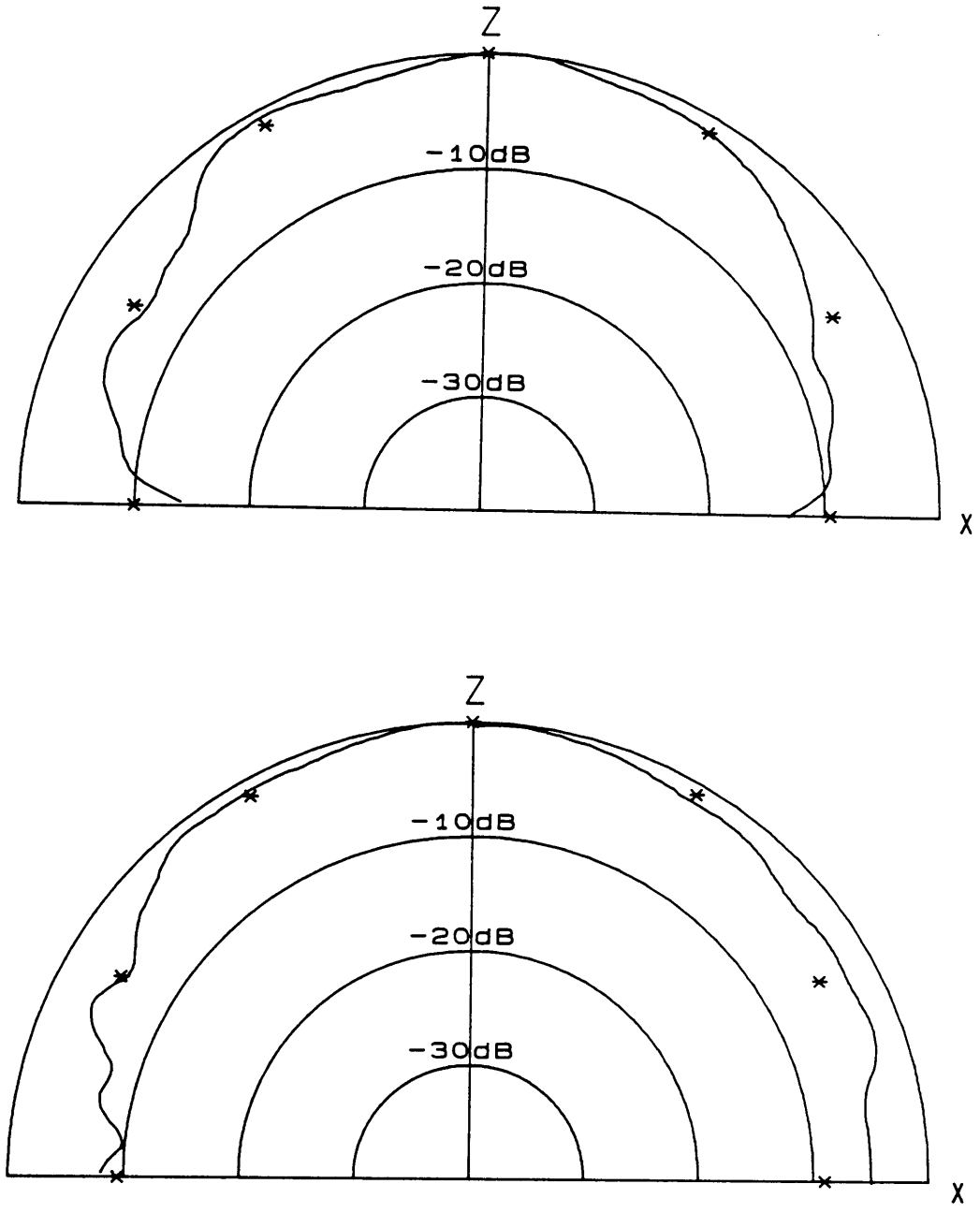

Figure C-1. Measured radiation patterns of AEL spiral model AST-1492A at 3.0 GHz: top $\phi = 0°$ plane pattern horizontal polarization, bottom, $\phi = 0°$ plane pattern vertical polarization. Asterisks represent nominal AEL results [29]; V.T. results-solid.

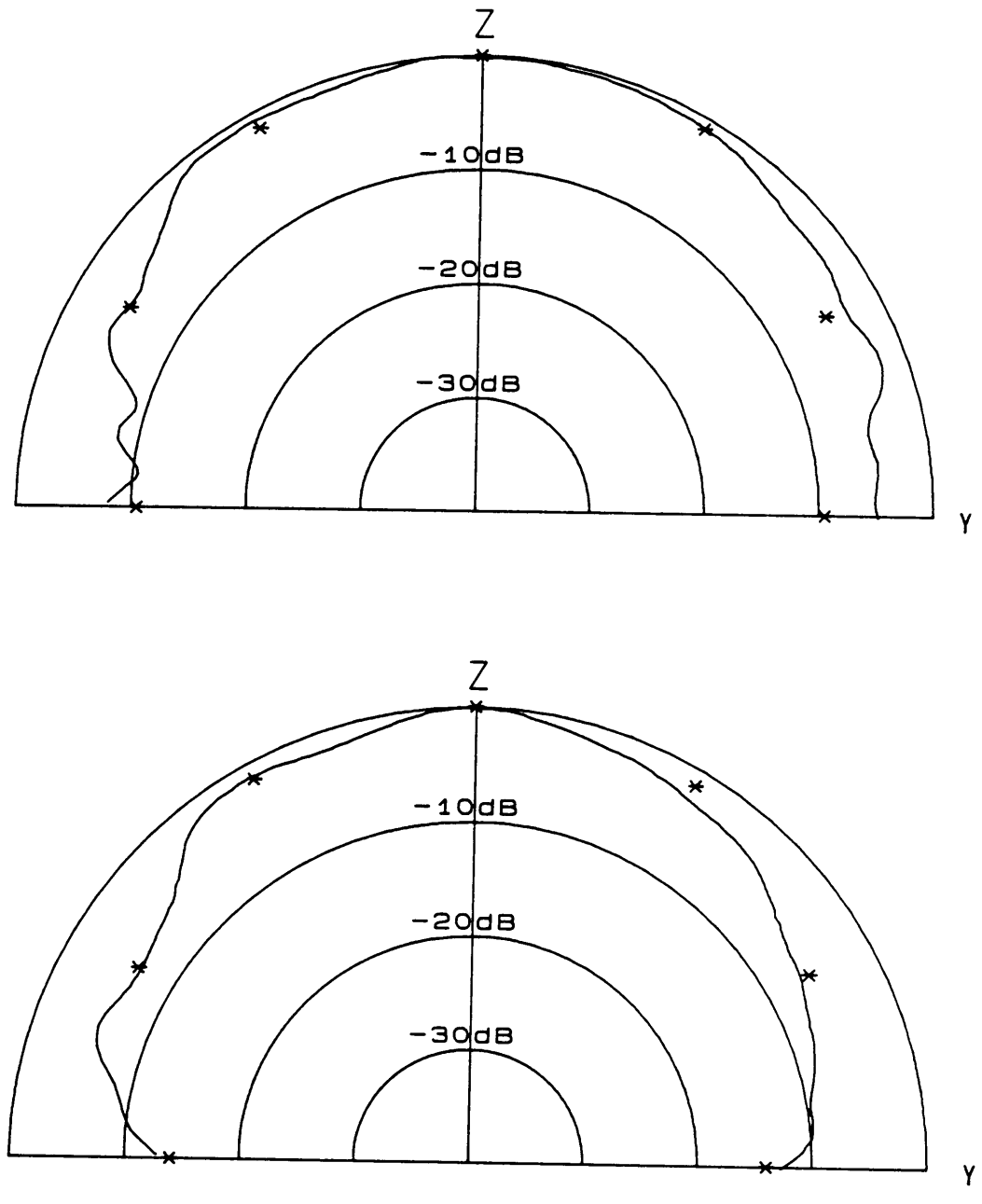

Figure C-1 (continued), top $\phi = 90°$ plane pattern horizontal polarization, bottom, $\phi = 90°$ plane pattern vertical polarization. Asterisks represent nominal AEL results [29]; V.T. results-solid.

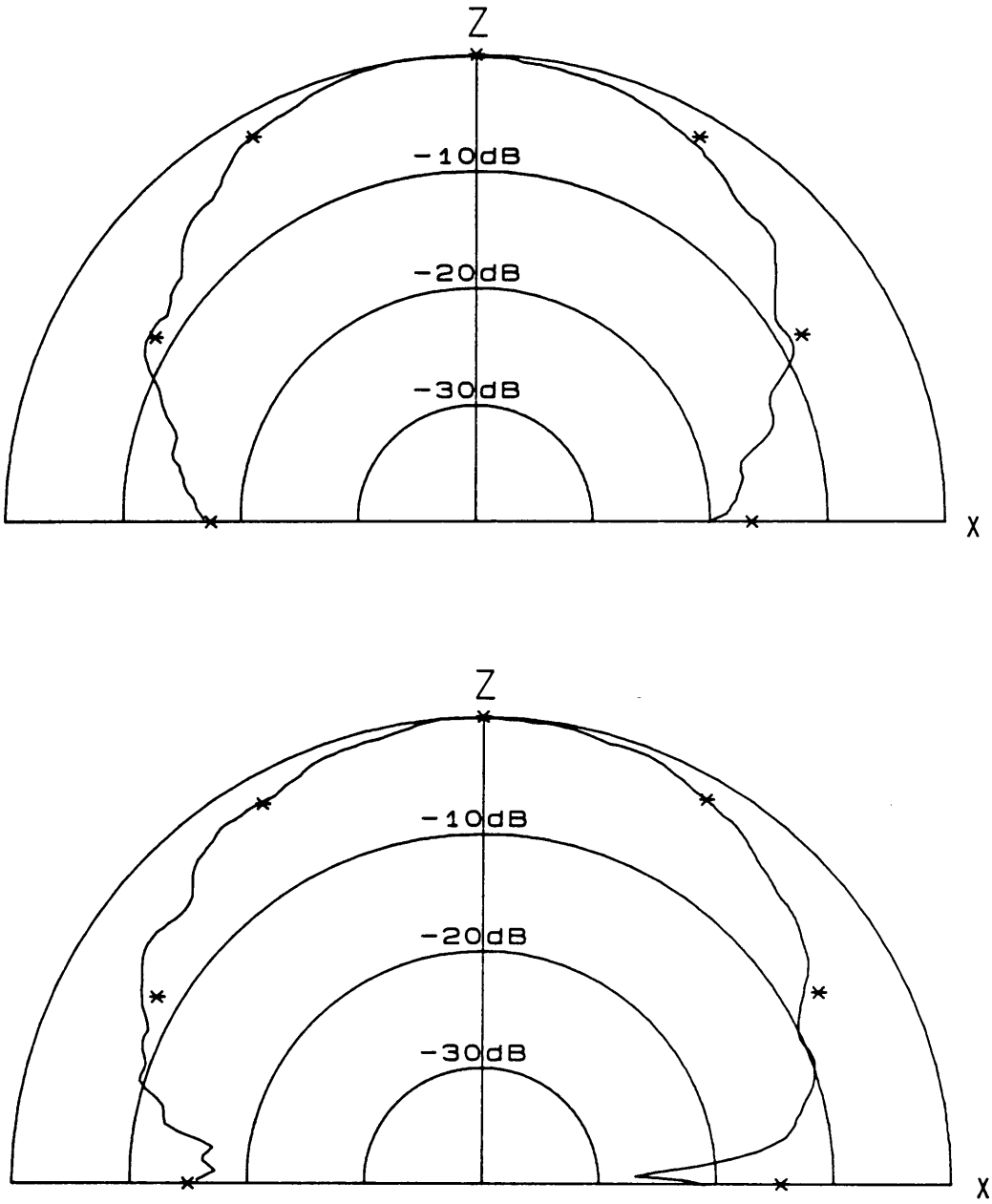

Figure C-2. Measured radiation patterns of AEL spiral model AST-1492A at 6.0 GHz: top $\phi = 0°$ plane pattern horizontal polarization, bottom, $\phi = 0°$ plane pattern vertical polarization. Asterisks represent nominal AEL results [29]; V.T. results-solid.

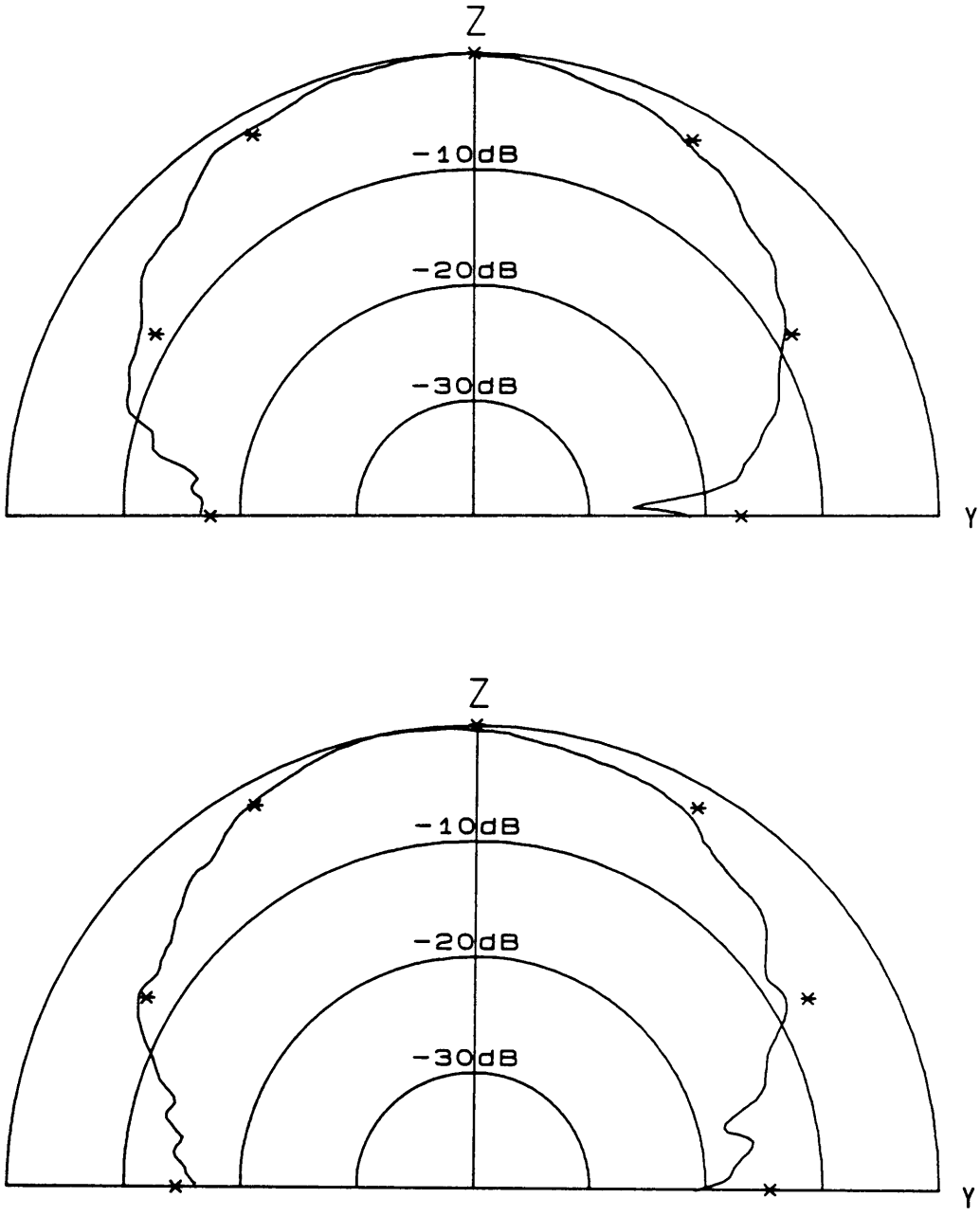

Figure C-2 (continued), top $\phi = 90°$ plane pattern horizontal polarization, bottom, $\phi = 90°$ plane pattern vertical polarization. Asterisks represent nominal AEL results [29]; V.T. results-solid.

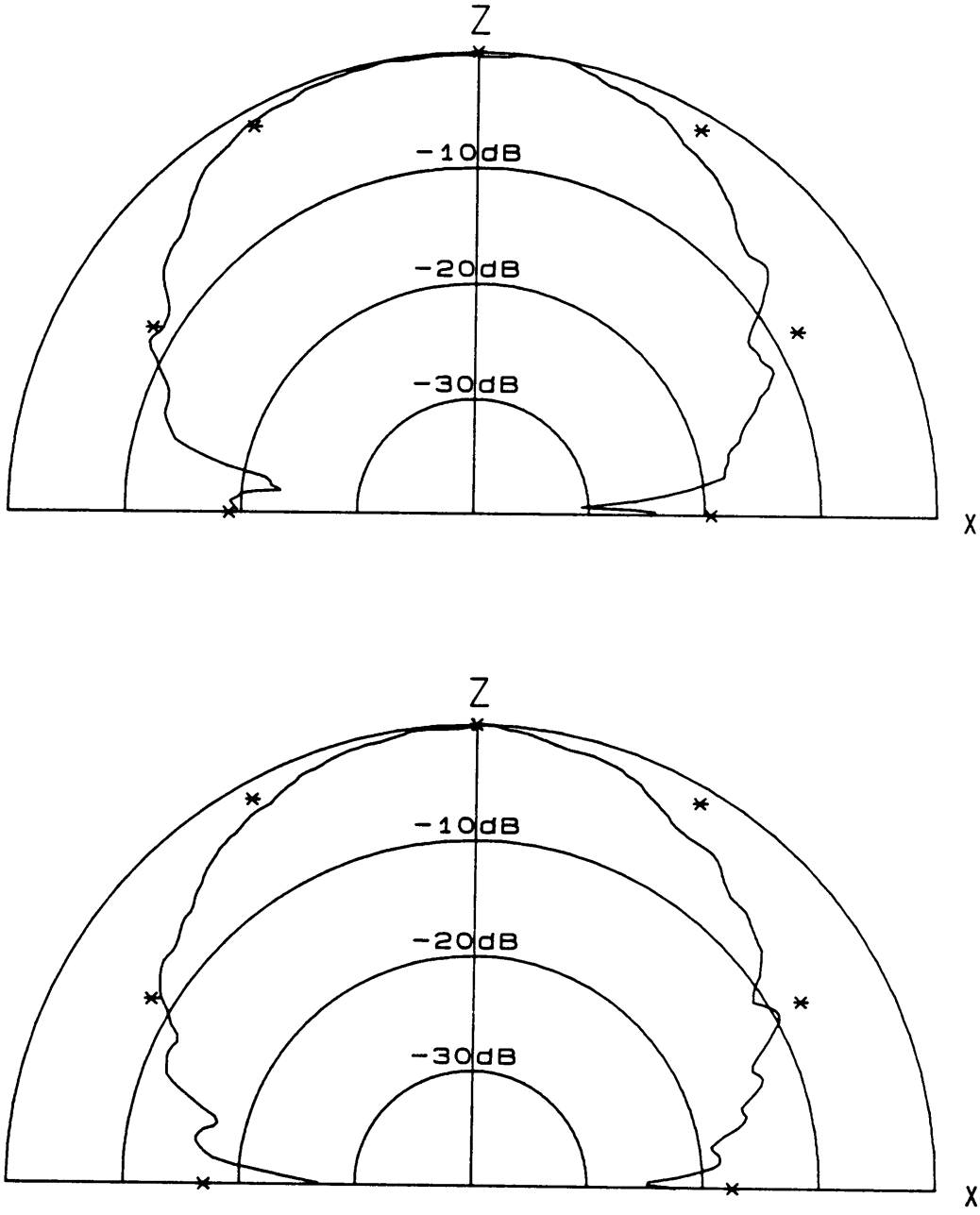

Figure C-3. Measured radiation patterns of AEL spiral model AST-1492A at 10.0 GHz: top $\phi = 0°$ plane pattern horizontal polarization, bottom, $\phi = 0°$ plane pattern vertical polarization. Asterisks represent nominal AEL results [29]; V.T. results-solid.

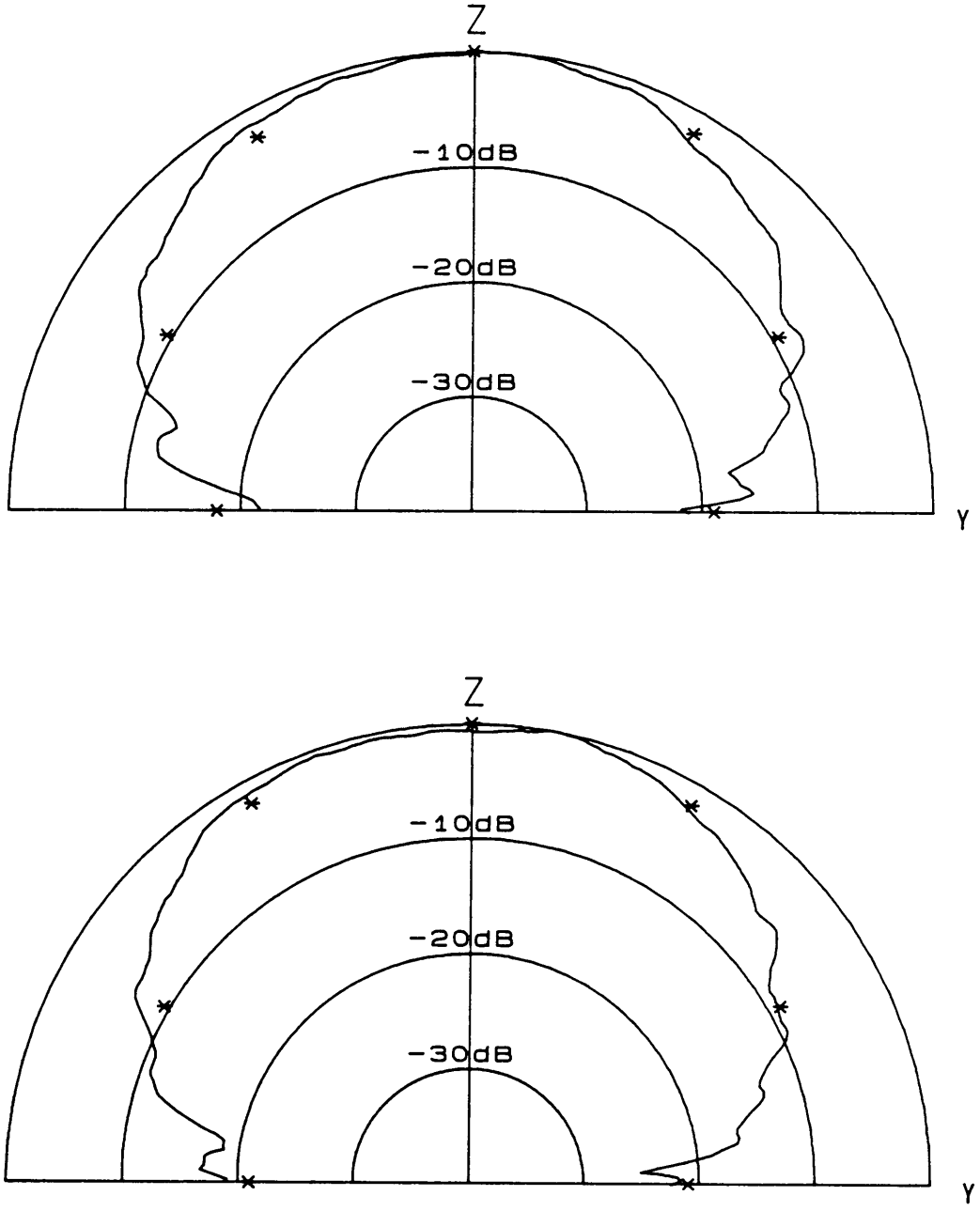

Figure C-3 (continued), top $\phi = 90°$ plane pattern horizontal polarization, bottom, $\phi = 90°$ plane pattern vertical polarization. Asterisks represent nominal AEL results [29]; V.T. results-solid.

Appendix D: Comparison of AEL and Constructed Spiral Patterns

In this appendix radiation patterns of the Archimedean spiral designed in Section 4.2 are presented along with radiation patterns recorded for the AEL AST-1492A cavity backed Archimedean spiral. All of the radiation patterns were recorded at the Virginia Tech far field antenna range [27]. The geometries used in making the patterns are shown in Figs. 7.2-1 and 7.2-2. The patterns, which were recorded at 2.5, 6.0, and 10.0 GHz, are presented in Figs. D-1 to D-3. A discussion of the patterns is presented in Section 7.2.

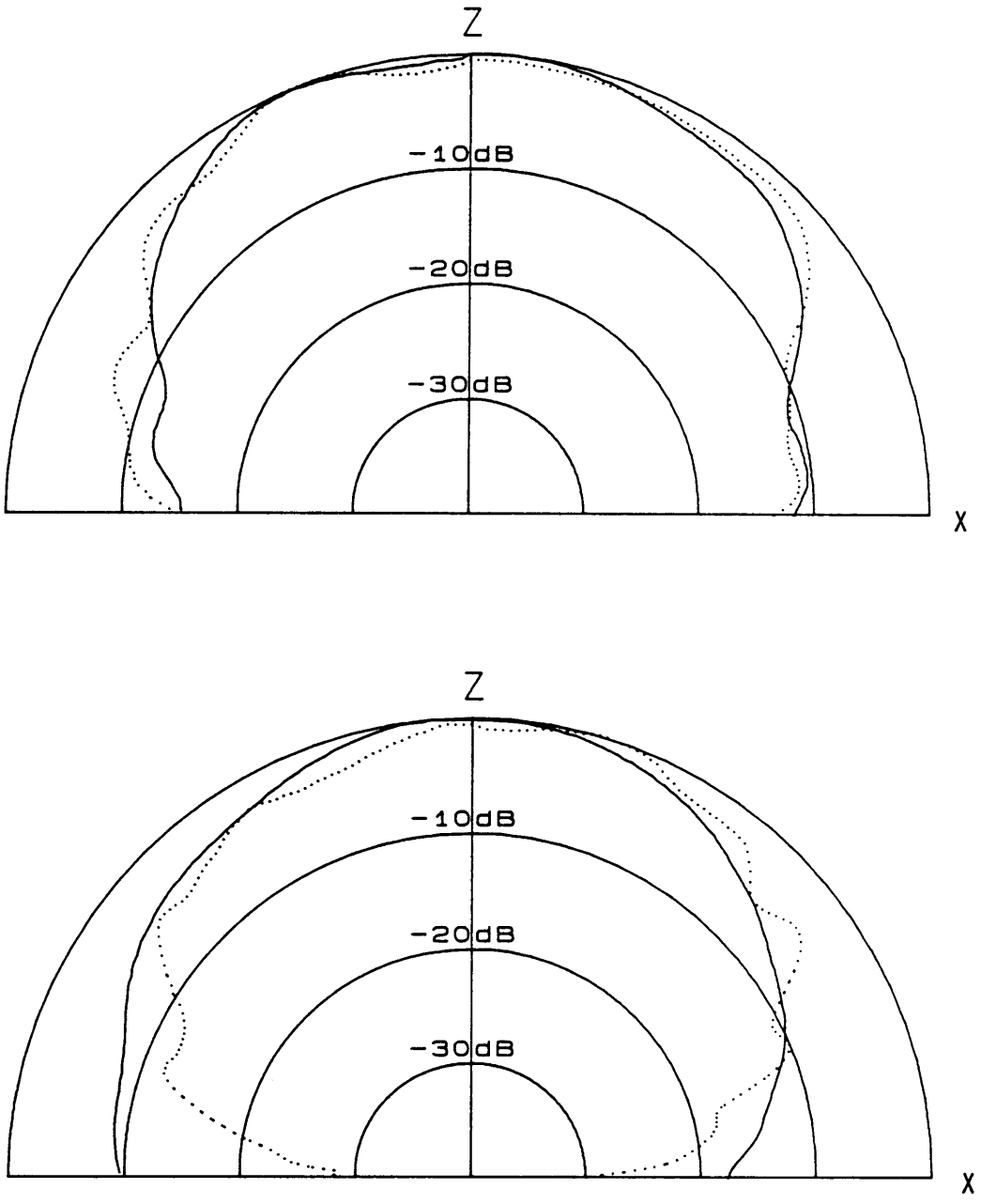

Figure D-1. Radiation patterns at 2.5 GHz: top $\phi = 0°$ plane pattern horizontal polarization, bottom, $\phi = 0°$ plane pattern vertical polarization. Spiral from Section 4.1-solid; AEL model AST-1492A spiral-dashed.

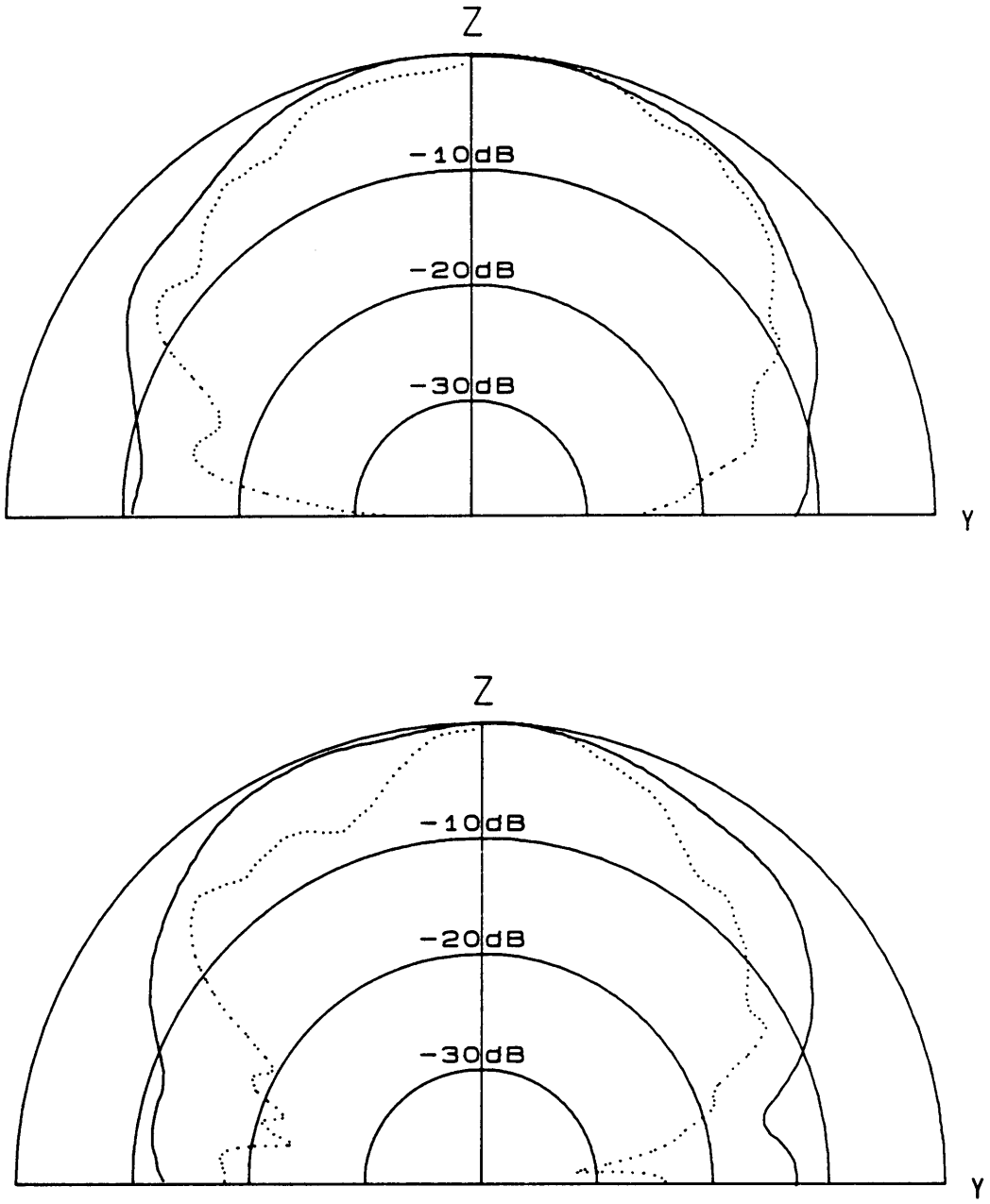

Figure D-1. (continued): top $\phi = 90°$ plane pattern horizontal polarization, bottom, $\phi = 90°$ plane pattern vertical polarization. Spiral from Section 4.1-solid; AEL spiral-dashed.

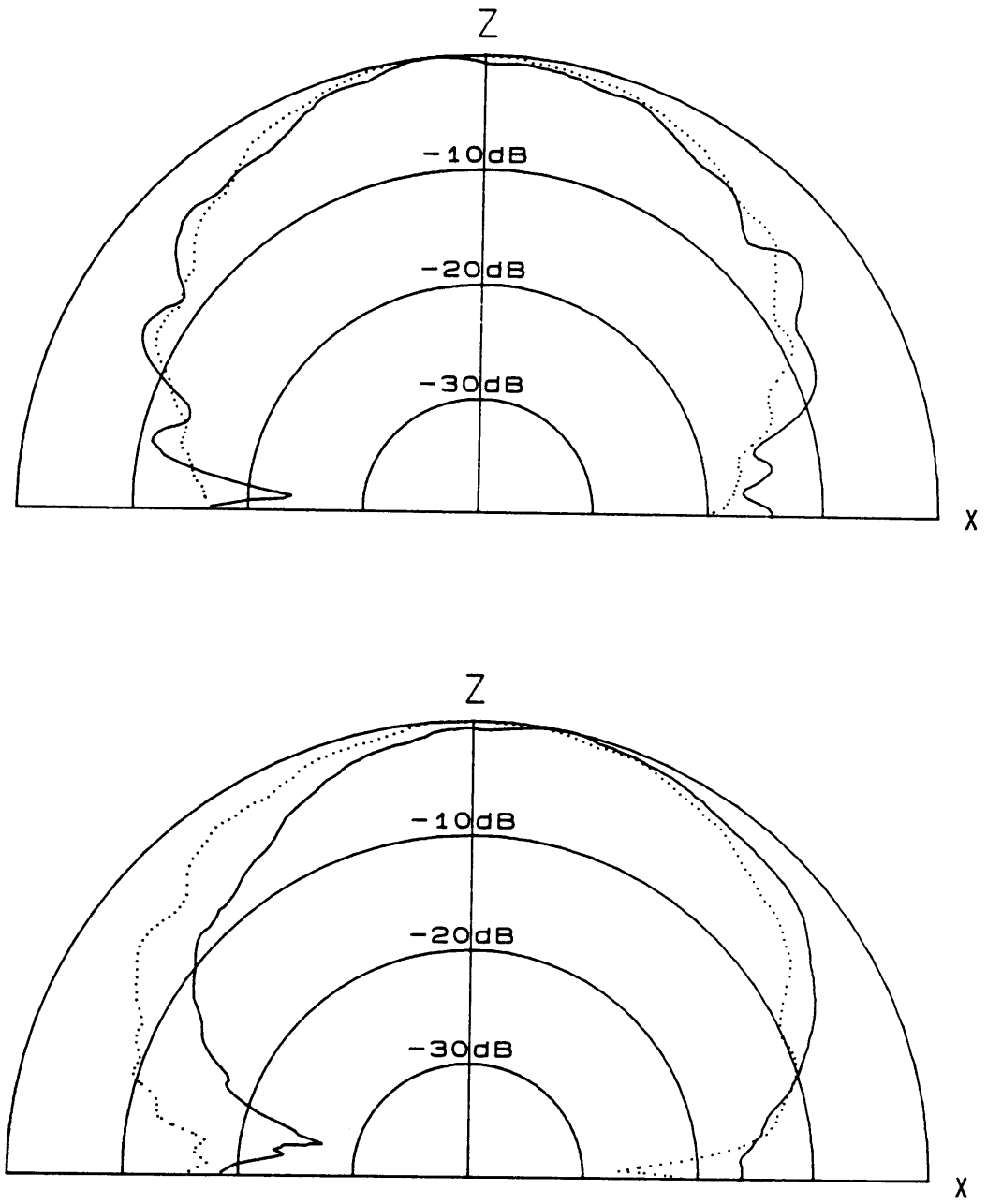

Figure D-2. Radiation patterns at 6.0 GHz: top $\phi = 0°$ plane pattern horizontal polarization, bottom, $\phi = 0°$ plane pattern vertical polarization. Spiral from Section 4.1-solid; AEL model AST-1492A spiral-dashed.

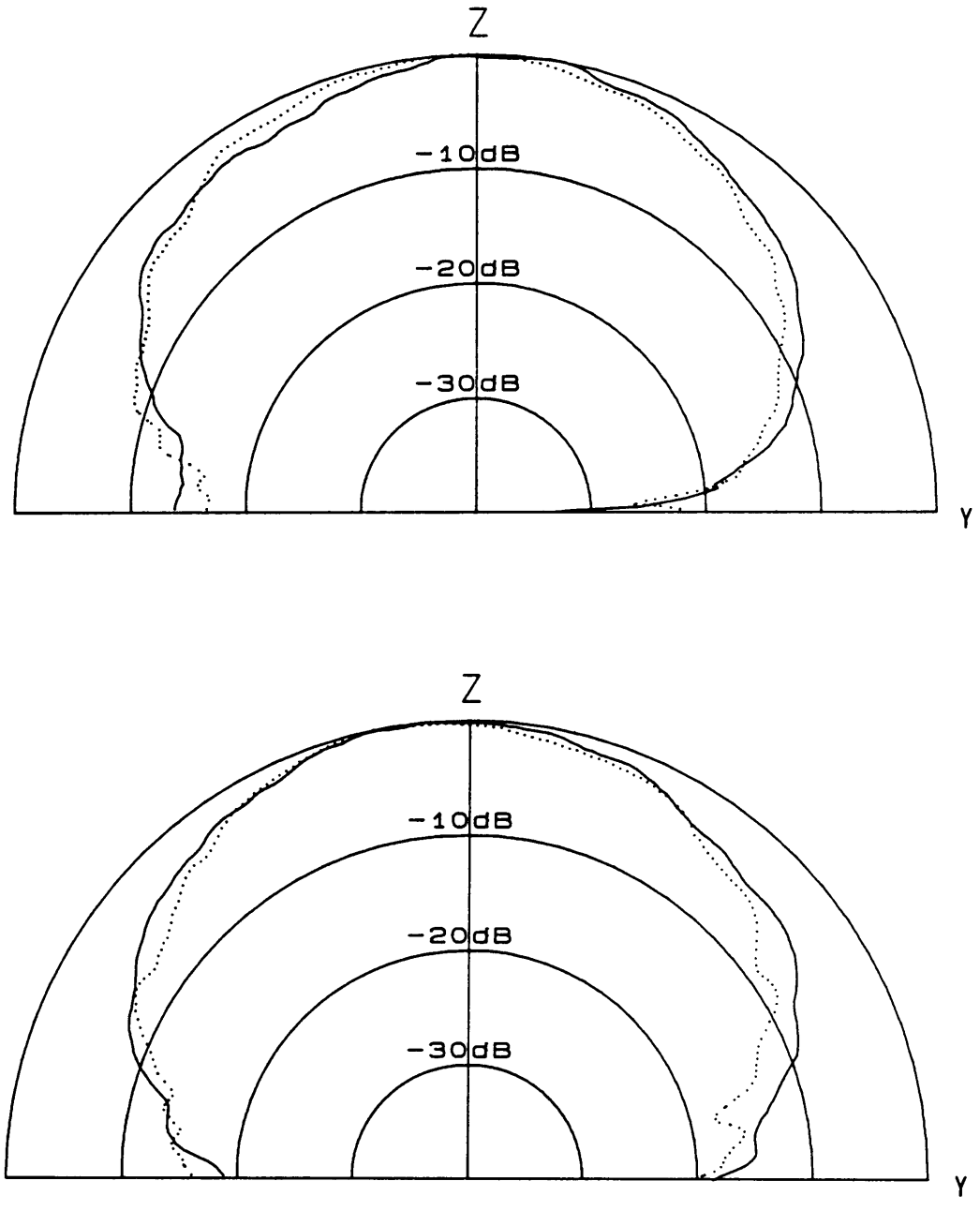

Figure D-2. (continued): top $\phi = 90°$ plane pattern horizontal polarization, bottom, $\phi = 90°$ plane pattern vertical polarization. Spiral from Section 4.1-solid; AEL spiral-dashed.

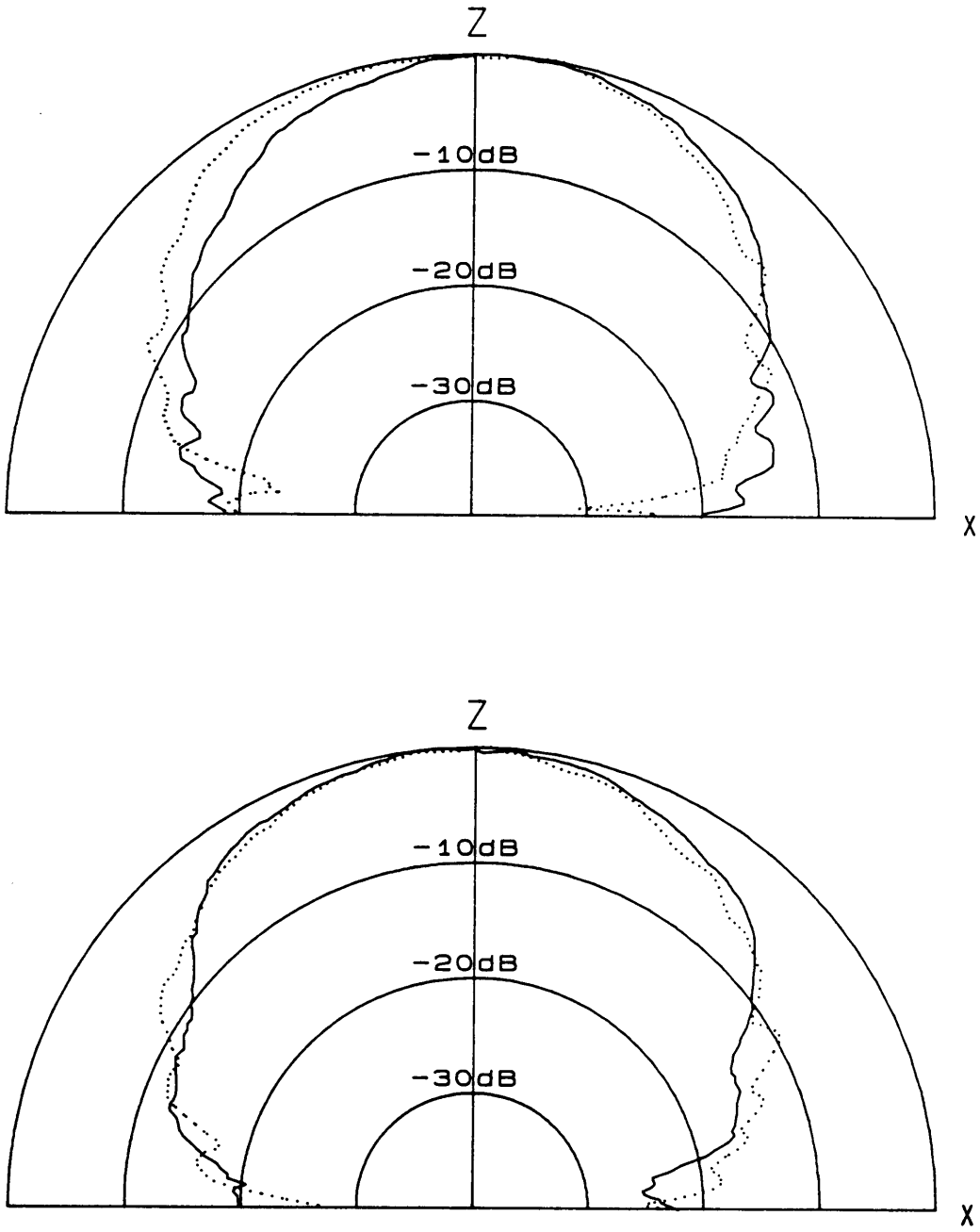

Figure D-3. Radiation patterns at 10.0 GHz: top $\phi = 0°$ plane pattern horizontal polarization, bottom, $\phi = 0°$ plane pattern vertical polarization. Spiral from Section 4.1-solid; AEL model AST-1492A spiral-dashed.

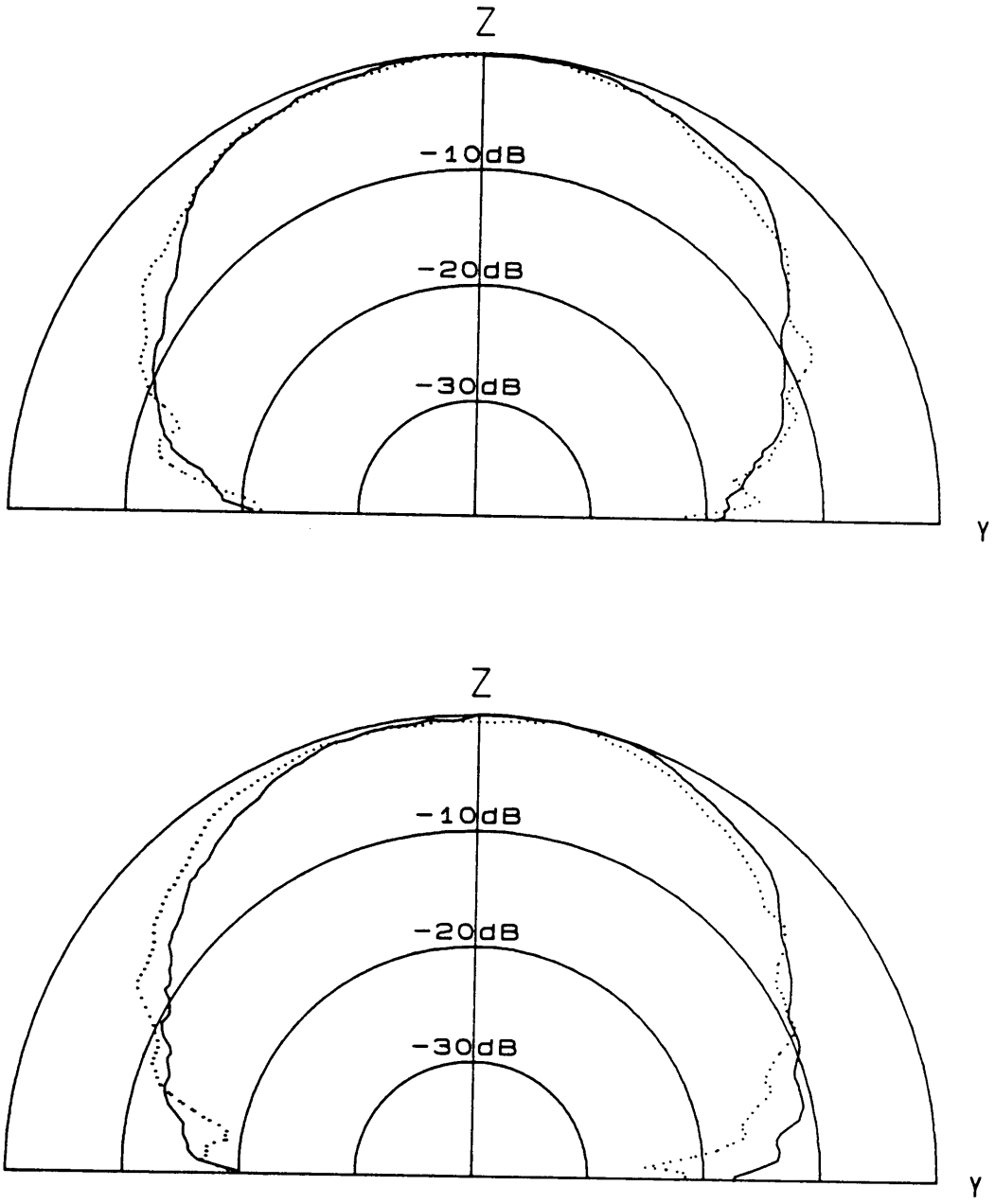

Figure D-3. (continued): top $\phi = 90°$ plane pattern horizontal polarization, bottom, $\phi = 90°$ plane pattern vertical polarization. Spiral from Section 4.1-solid; AEL spiral-dashed.

Appendix E: Patterns Produced by a Traveling Wave Current Loop

In Section 2.1 the statement was made that many of the radiating characteristics of spiral antennas can be explained by a "band" description of radiation. This statement was followed by a discussion of the case of a two arm spiral whose arms are excited with equal amplitudes and opposite phases (the $M = 1$ mode of excitation). Using the principles of band theory (that the source of radiation from this spiral is an annular band with a circumference of one wavelength in which the currents on the two arms of the spiral are approximatly inphase) the radiation of this spiral should be similar to that produced by a one wavelength loop of traveling wave current. In this appendix, the fields radiated by a hypothetical source consisting of a one wavelength loop of traveling wave current are calculated.

The loop of current is located in the xy-plane as shown in Fig. E-1. The current density on the loop is given by

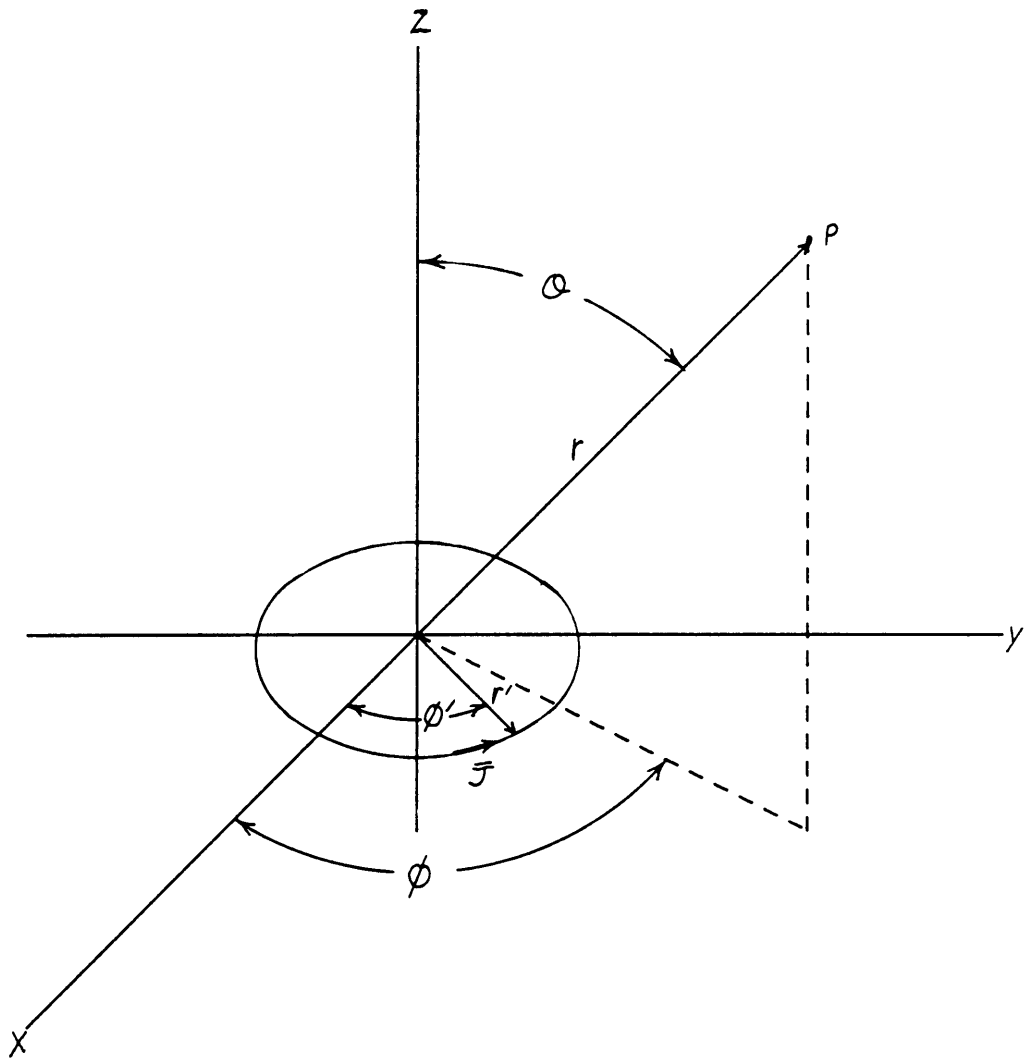

Figure E-1. One wavelength traveling wave current loop located in the xy-plane.

$$\bar{J} = I_o e^{-j\phi'} \delta(r' - \lambda/2\pi)\delta(\theta' - \pi/2)\hat{\phi}'. \tag{E-1}$$

Using a parallel ray approximation, the far field can be calculated using [2].

$$\bar{E} = -j\omega\mu\bar{A} - (-j\omega\mu\bar{A} \cdot \hat{r})\hat{r}, \tag{E-2}$$

where $\bar{A}$ is given by

$$\bar{A} = \frac{e^{-j\beta r}}{4\pi r} \int\int\int_{v'} \bar{J} e^{j\beta \hat{r} \cdot r'} \, dv'.$$

For the geometry of Fig. E-1,

$$\hat{r} \cdot r' = r' \sin\theta \cos(\phi - \phi') \tag{E-3}$$

and

$$\hat{\phi}' = \hat{r} \sin\theta \sin(\phi - \phi') + \hat{\theta} \cos\theta \sin(\phi - \phi') + \hat{\phi} \cos(\phi - \phi'). \tag{E-4}$$

Substitution of (E-1), (E-3) and (E-4) into (E-2) leads to the following electric fields:

$$\bar{E}_\phi = -jK \cos\theta \int_0^{2\pi} \sin(\theta - \theta') e^{j[\sin\theta \cos(\phi - \phi') - \phi']} \, d\phi'. \tag{E-5}$$

and

$$\overline{E}_{\phi} = -jK\int_0^{2\pi} \cos(\theta - \theta')e^{j[\sin\theta\cos(\phi-\phi')-\phi']}\,d\phi'. \qquad (E\text{-}6)$$

where

$$K = \frac{I_o\omega\mu e^{-j\beta r}}{4\pi r}$$

Numerical integration was used to calculate the normalized fields given by (E-5) and (E-6) in the two principle plane defined by $\phi = 0.0°$ (the xz-plane) and $\phi = 90.0°$ (the yz-plane). The patterns are shown Fig E-2, where vertical polarization is defined as being parallel to the x-axis and horizontal polarization is defined as being parallel to the y-axis.

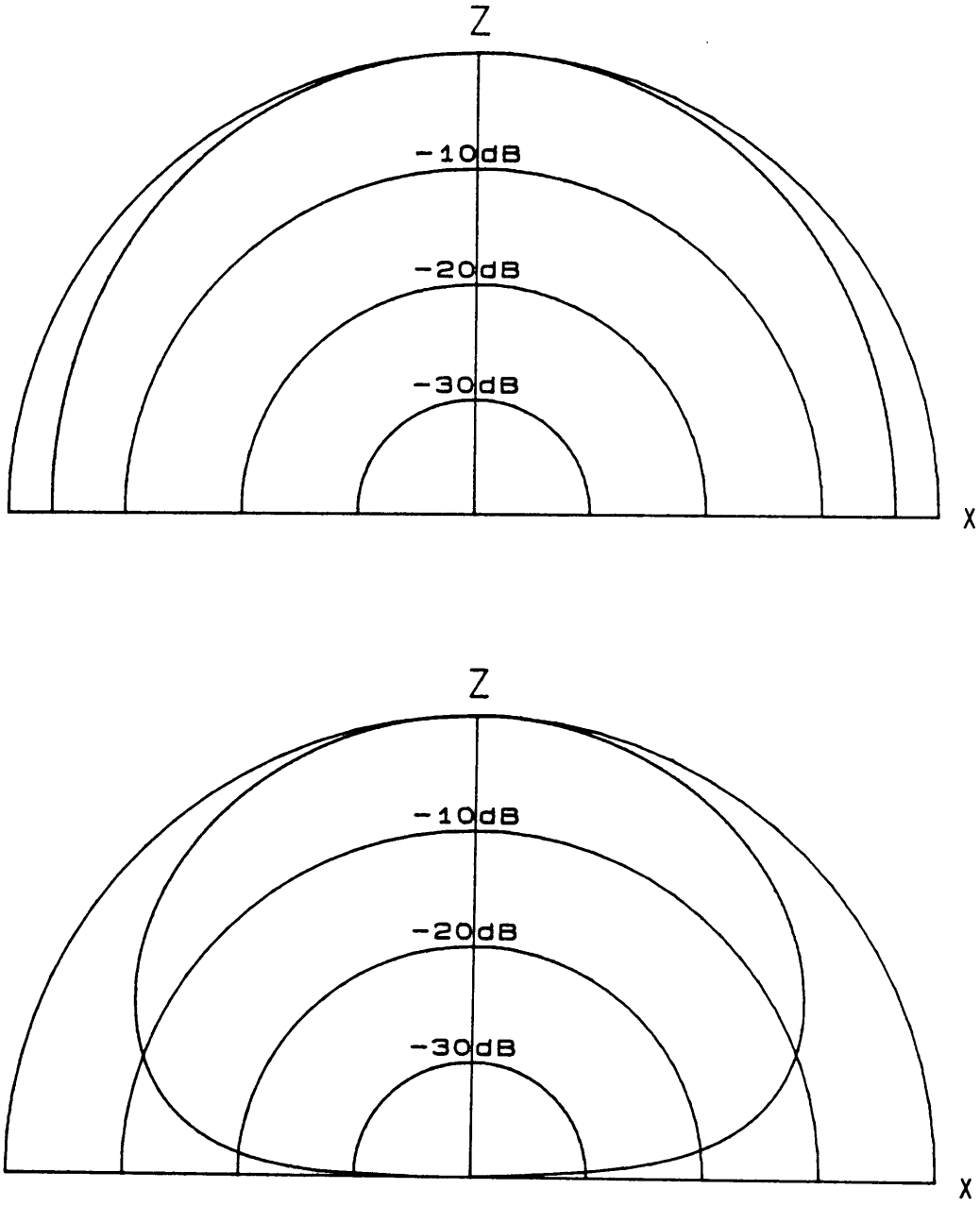

Figure E-2 Radiation patterns produced by a one wavelength loop of traveling wave current: top $\phi = 0.0°$ plane pattern horizontal polarization, bottom, $\phi = 0.0°$ plane pattern vertical polarization.

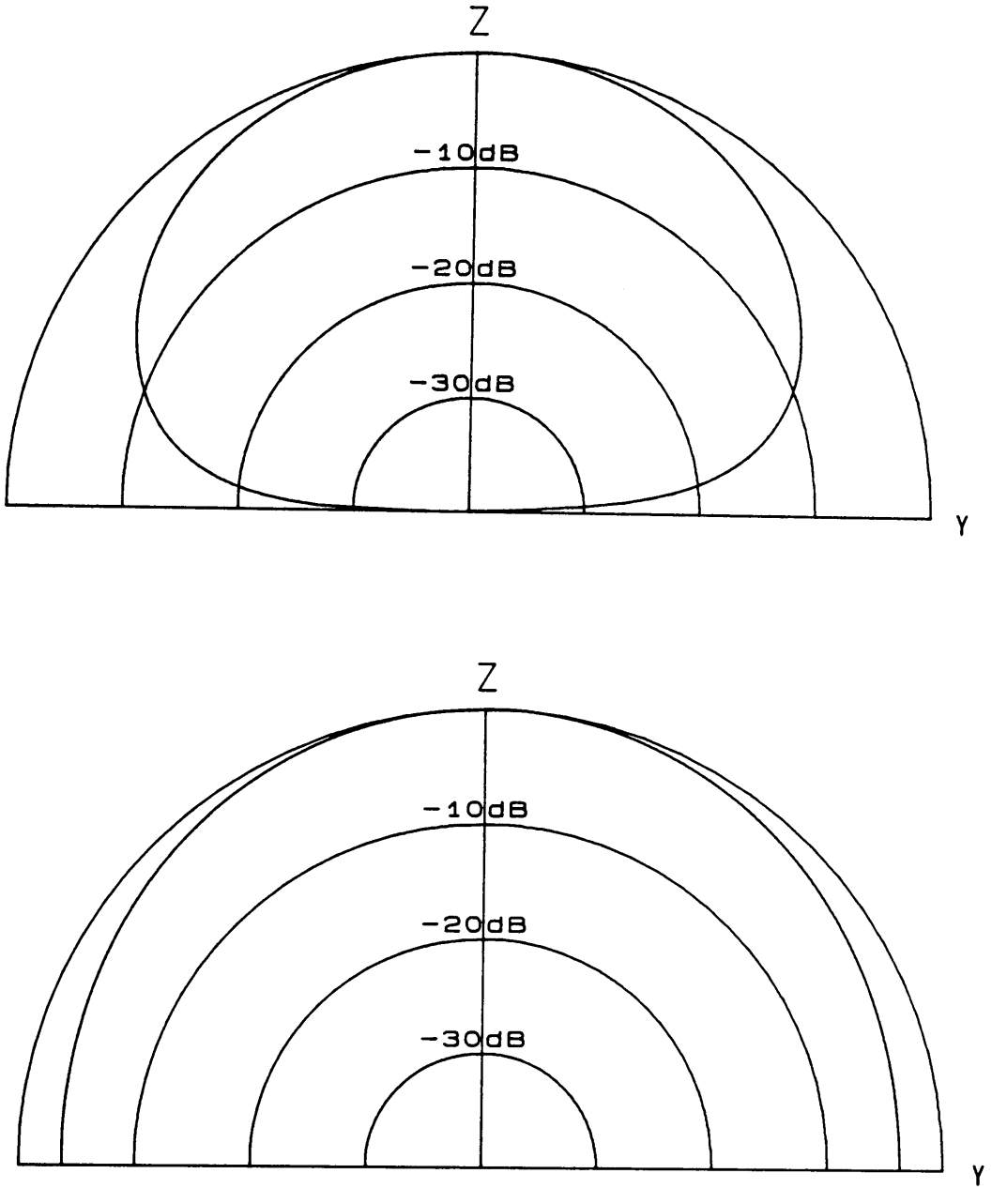

Figure E-2 (continued): top $\phi = 90.0°$ plane pattern horizontal polarization, bottom, $\phi = 90.0°$ plane pattern vertical polarization.

References

1. D.G. Shively, *Wideband Planer Array Antennas: Theory and Measurements*, Thesis, The Bradley Department of Electrical Engineering, Virginia Tech., Blacksburg Va., April 1988.

2. W.L. Stutzman and W.L.Thiele, *Antenna Theory and Design*, John Wiley & Sons: New York, 1981.

3. R.C. Johnson and H. Jasik, *Antenna Engineering Handbook, Second Edition*, McGraw-Hill: New York, 1984.

4. B.R.S. Cheo, V.H. Rumsey and W.J. Welch, "A Solution to the Frequency-Independent Antenna Problem," *IRE Trans. on Ant. and Prop.*, vol. AP-9, pp. 527-534, Nov. 1961.

5. V. Rumsey, *Frequency Independent Antennas*, Academic Press: New York, 1966.

6. E.A. Wolff, *Antenna Analysis*, Wiley: New York, 1967.

7. P.E. Mayes and J.D. Dyson, "A Note on the Difference Between Equiangular and Archimedes Spiral Antennas," *IEEE Trans. on Micro. Theory and Tech.*, vol. Mitt-9, pp. 203-205, March 1961.

8. S.E. Lipsky, *Microwave Passive Direction Finding*, John Wiley & Sons: New York, 1987.

9. W.L. Stutzman, "Near Field Feasibility Study, Part 1: Probe Antenna Element Investigation," New Mexico State University Physical Science Laboratory Report Number PN01049, Nov. 1983.

10. E.T. Roland and W.F. Patterson, "A Slow-Wave Flat Spiral Antenna," 17th USAF Antenna Applications Symposium, U. of Illinois Allerton Park, Nov. 1967.

11. J.A. Kaiser, "The Archimedean Two-Wire Spiral Antenna," *IRE Trans. on Ant. and Prop.*, vol.AP-8, pp.312-323, May 1960.

12. J.W. Duncan and V.P. Minerva, "100 - 1 Bandwidth Balun Transformer," *Proc. IRE*, vol.48, pp. 156-164: Feb. 1960.

13. R.W. Klopfenstein, "A Transmission Line Taper of Improved Design," *Proc. IRE*, vol.44, pp.31-35, Jan. 1956.

14. R.E. Collin, "Theory and Design of Wide-Band Multisection Quarter-Wave Transformers," *Proc IRE.*, vol.43, pp.179-185, Feb.1955.

15. T.T. Taylor, "Dolph Arrays of Many Elements," Tech. Memo. no.320, Hughes Aircraft co., Culver City, Calif., August 18, 1953.

16. R. Bawer and J.J. Wolfe, "The Spiral Antenna," *IRE. Int. Conv. Rec.*, pp.84-87, 1960.

17. E.H. Newman and R.L. Dilsavor, *A Users Manual for the Electromagnetic Surface Patch Code: ESP Version III*, Technical Report No.716148-19, Grant NSG 1613, May 1987.

18. C. Balanis, *Antenna Theory Analysis and Design*, Harper & Row: New York, 1982.

19. S.A. Schelkonoff, "On the Diffraction and Radiation of Electromagnetic Waves," *Physics Review*, vol.56, August 15, 1939.

20. R.F. Harrington, *Time Harmonic Electromagnitic Fields*, McGraw Hill: New York, 1961.

21. E.H. Newman and D.M. Pozar, "Electromagnetic Modeling of Composite Wire and Surface Geometries," *IEEE Trans. Antennas and Propagation*, Vol.AP-26, pp.784-789, Nov. 1978.

22. E.H. Newman and M.R. Schrote, "On the Current Distribution for Open Surfaces," *IEEE Trans. on Antennas and Propagation*, Vol.AP-31, pp.515-518, May 1983.

23. E.H. Newman, P. Alexandroupoulos, "Polygonal Plate Modeling of Realistic Structures," *IEEE Trans. on Antennas and Propagation*, Vol. AP-32, pp 742-747, July 1984.

24. J.H. Richmond, E.D. Pozar and E.H. Newman, "Rigorous Near-Zone Field Expressions for Rectangular Sinusoidal Surface Monopoles," *IEEE Trans. on Antenna and Propagation*, Vol. AP-26, pp.509-510, Jan.1976.

25. E.H. Newman and D.M. Pozer, "Considerations for Efficient Wire/Surface Modeling," *IEEE Trans. on Antennas and Propagation*, Vol. AP-28, pp. 121-125, Jan. 1980.

26. E.H. Newman and P. Tulyathan, "A Surface Patch Model for Polygonal Plates," *IEEE Trans. on Antennas and Propagation*, Vol. AP-30, pp.588-593, July 1982.

27. D.G. Shively and W.L. Stutzman, *The Virginia Tech Antenna Laboratory: Documentation and Performance*, The Bradley Department of Electrical Engineering, Virginia Tech, Blacksburg, Va., April 1988.

28. H. Nakano, *Helical and Spiral Antennas, A Numerical Approach*, John Wiley & Sons: New York, 1987.

29. "Cavity Backed Spiral Antenna AEL Model AST-1492A Data Package" American Electronics Laboratories, Inc., P.O. Box 552, Lansdale, Pa. 19466.

The vita has been removed from the scanned document